AIP | Review of Scientific Instruments

Invited Review Article: Combining scanning probe microscopy with optical spectroscopy for applications in biology and materials science

Marcel Lucas and Elisa Riedo

Citation: Rev. Sci. Instrum. **83**, 061101 (2012); doi: 10.1063/1.4720102
View online: http://dx.doi.org/10.1063/1.4720102
View Table of Contents: http://rsi.aip.org/resource/1/RSINAK/v83/i6
Published by the American Institute of Physics.

Invited Review Article: Combining scanning probe microscopy with optical spectroscopy for applications in biology and materials science

Marcel Lucas[a] and Elisa Riedo
School of Physics, Georgia Institute of Technology, Atlanta, Georgia 30332-0430, USA

(Received 10 February 2011; accepted 22 January 2012; published online 7 June 2012)

This is a comprehensive review of the combination of scanning probe microscopy (SPM) with various optical spectroscopies, with a particular focus on Raman spectroscopy. Efforts to combine SPM with optical spectroscopy will be described, and the technical difficulties encountered will be examined. These efforts have so far focused mainly on the development of tip-enhanced Raman spectroscopy, a powerful technique to detect and image chemical signatures with single molecule sensitivity, which will be reviewed. Beyond tip-enhanced Raman spectroscopy and/or topography measurements, combinations of SPM with optical spectroscopy have a great potential in the characterization of structure and quantitative measurements of physical properties, such as mechanical, optical, or electrical properties, in delicate biological samples and nanomaterials. The different approaches to improve the spatial resolution, the chemical sensitivity, and the accuracy of physical properties measurements will be discussed. Applications of such combinations for the characterization of structure, defects, and physical properties in biology and materials science will be reviewed. Due to the versatility of SPM probes for the manipulation and characterization of small and/or delicate samples, this review will mainly focus on the apertureless techniques based on SPM probes. © *2012 American Institute of Physics*. [http://dx.doi.org/10.1063/1.4720102]

I. INTRODUCTION

A. Motivation

Nanostructures have been extensively researched for their potential integration in electronic components, sensors, energy harvesters, and biological systems. In order to predict their behavior in devices, a thorough characterization of their physical properties is required. Due to their small sizes and technical challenges related to their synthesis and manipulation, new tools with high resolution and sensitivity are needed for the characterization of nanostructures. Electron microscopy has been widely used to characterize the morphology and crystalline structure of nanomaterials, but these techniques are mainly limited to conductive or thin samples. Transmission electron microscopy (TEM) is inapplicable to nanostructures that are integrated into devices on a solid substrate. The sample can be damaged during imaging, meaning it cannot be recovered for the next fabrication step. Imaging point defects with a TEM still represents a technical challenge. Also, due to the uncertainty in sample thickness and the small gap between the pole-pieces, the *in situ* TEM characterization of optical, mechanical, tribological, and/or electron transport properties of nanostructures is very challenging or impossible.[1,2]

Fluorescence microscopy has provided a wealth of chemical information, giving insight into a variety of chemical reactions and biological processes. However, the spatial resolution of conventional optical microscopy is limited by the diffraction limit, which is about half the wavelength of the light. Considerable efforts have been made to increase the spatial resolution beyond the diffraction limit. Development of photoswitchable fluorophores and their sequential illumination led to the development of stimulated emission depletion, stochastic optical reconstruction, and photoactivatable localization microscopies, which improved the spatial resolution to a few tens of nm.[3] However, fluorescence microscopy requires labeling, since not every molecule is fluorescent. This complicates the sample preparation and introduces labels that may interfere with the physical properties of the sample or the behavior of biological samples. In addition, fluorescence microscopy provides no chemical signature from the sample for its identification.

Advances in scanning probe microscopy (SPM) addressed these issues and provided an abundant wealth of information on the topography and physical properties of nanomaterials, in some cases at atomic resolution. SPM is extremely versatile and can operate in vacuum, air, or liquids; on insulating or metallic samples. In parallel, optical spectroscopy, such as Raman spectroscopy, is an indispensable tool for the collection of chemical signatures, characterization of the crystalline structure and orientation, point defects, mechanical deformation and thermal properties. In this review, the technical difficulties associated with the combination of SPM with various optical spectroscopies, including Raman spectroscopy, will be examined. Reports of such combinations in the literature will be reviewed and discussed. Efforts to combine SPM with optical spectroscopy have so far been mostly directed toward the development of tip-enhanced Raman spectroscopy, which will be reviewed. But in the following sections, the great potential of SPM-optical spectroscopy combinations beyond tip-enhanced Raman spectroscopy will also be emphasized and of particular interest are combinations that enable the characterization of structure and quantitative measurements of

[a]Present address: Institute for Shock Physics and Department of Physics, Washington State University, Pullman, Washington 99164-2816, USA. Electronic mail: marcel.lucas@wsu.edu.

physical properties, such as mechanical, optical, or electrical properties. The different approaches to improve the spatial resolution, the chemical sensitivity and the accuracy of physical properties measurements will be discussed. Applications of such combinations for the characterization of structure, defects, and physical properties in biology and materials science will be reviewed. Although near-field optical microscopies with aperture will be mentioned, this review will mainly focus on apertureless near-field optical spectroscopy/microscopies.

B. Outline

In Sec. II, the various feedback mechanisms used in scanning probe microscopy to maintain the tip-sample distance constant and measure the sample physical properties are briefly reviewed. In Sec. III, Raman spectroscopy, coherent anti-stokes Raman spectroscopy, and surface-enhanced Raman spectroscopy will be presented. In Sec. IV, some of the technical issues related to combinations of scanning probe microscopy with optical spectroscopy, including excitation wavelength, sample illumination configuration, and spatial resolution, will be discussed. Efforts to break the diffraction limit in Raman spectroscopy by aperture scanning near-field microscopy will be discussed. Tip-enhanced Raman spectroscopy, an apertureless scanning near-field technique, will be introduced and reviewed in Sec. V. In Sec. VI, demonstrations of combinations of scanning probe microscopy with other optical spectroscopies, such as fluorescence and infrared spectroscopy, will be described. Finally, the potential applications in biology and materials science will be reviewed in Sec. VII.

II. SCANNING PROBE MICROSCOPY

A. Principle

Scanning probe microscopy has been extensively used for surface analysis of the physical properties at the nanoscale. Typically, a sharp probe is kept in the vicinity of the sample by using various feedback mechanisms. The sharpness of the tip apex, reduced to a single atom in some cases, can provide information on the topography and the physical properties of the sample at atomic resolution in optimal conditions. The invention of the scanning tunneling microscope (STM) was soon followed by the development of various scanning probe microscopies based on different interactions between the probe and the sample.[4,5] The flexibility of the detection systems and advances in probe fabrication have expanded the versatility of scanning probe microscopy to the investigation of mechanical, electrical, tribological, thermal, chemical, magnetic interactions. In Sec. II B, the various feedback mechanisms to keep the tip-sample distance constant and to collect data about the sample physical properties are briefly reviewed.

B. Feedback mechanisms

The invention of STM enabled the imaging of topography and charge density variations at an atomic resolution.[4] In STM, a bias voltage is applied between a metallic sample and a sharp metallic tip with a single atom at the apex, typically made of tungsten. When the tip is at a distance of a few angstroms above the sample, a tunneling current can pass through the tip-sample gap. The tunneling current is a function of the tip-sample distance, bias voltage and the local electronic density of states of the sample. In order to keep the tip-sample distance constant, a feedback mechanism monitors variations of the tunneling current for a set voltage and adjusts the tip-sample distance with a piezoelectric scanner supporting the sample or the tip to maintain the current constant.[6–9] A topography image, or more precisely an image of the charge density, is collected by scanning the tip across the sample surface. Alternatively, an image of the tunneling current, which is related to the charge density, can be obtained by scanning the tip at constant voltage and tip-sample distance.[4] The latter method is preferred because of the higher acquisition rate.

A few years later, the atomic force microscope (AFM) was developed to analyze conductive and non-conductive samples. In most AFMs, a tip is located at the end of a cantilever and the cantilever deflection is monitored by a laser beam reflected off the back of the cantilever and analyzed by a four-quadrant photodetector. One feedback mechanism to collect a topography image is based on maintaining the deflection of the cantilever constant by adjusting the tip or sample height as the tip scans the sample in a constant contact mode.[5,10–12] Generally, STM offers a better lateral resolution than AFM due to the sharpness of the tip and a better control over the smaller tip-sample distance.

To increase sensitivity, particularly in liquids, the four-quadrant photodiode can be replaced by an interferometer. A low noise detection system based on a Fabry-Pérot interferometer with differential amplification was demonstrated in vacuum, air, and liquid.[13] An interferometry approach was implemented in an optical fiber-based system. The light from a laser diode is directed by an optical fiber to the interference cavity formed between the fiber end and the back of a reflective cantilever. The intensity of the reflected light is a function of the fiber-cantilever distance and is collected by the same optical fiber before its collection by a photodiode.[14] Another detection scheme, commonly used in aperture scanning near-field optical microscopy (SNOM), is based on a tuning fork with high quality factor.[15,16] The fiber tip is attached to one prong of a piezoelectric tuning fork which is vibrated at a set amplitude and frequency. When in resonance, the oscillation of the prongs is maximum and generates an oscillating piezoelectric potential that is used for feedback.[15]

Feedback mechanisms based on the oscillation frequency or amplitude of the probe led to the development of imaging modes where the tip never contacts the sample (non-contact mode) or only intermittently (tapping mode), which reduces damage to the sample and tip. One of the first applications led to the shear force feedback mechanism in aperture SNOM. The probe is excited at a set amplitude close to its resonance frequency. In the vicinity of the sample (below 20 nm), the tip vibration amplitude is damped by shear forces and its variation is used in a feedback loop to keep the tip-sample distance constant.[17] In AFM non-contact and tapping modes, the cantilever is driven in the normal direction at a set amplitude close to its resonance frequency. Variations of the oscillation

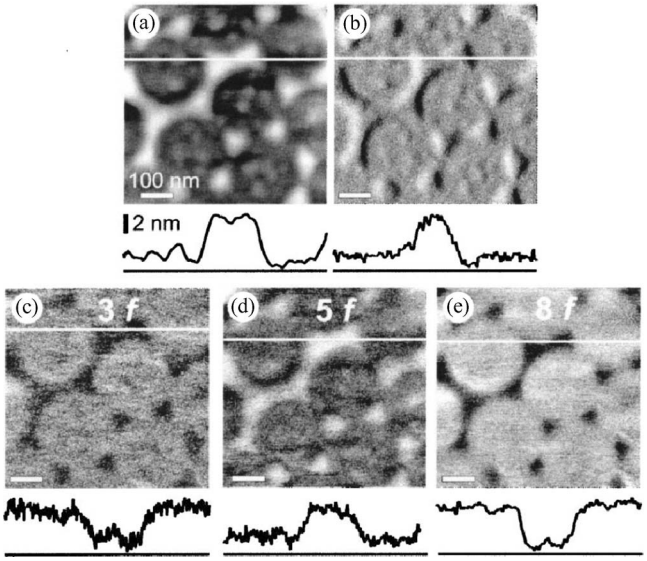

FIG. 1. Imaging with higher harmonics in tapping-mode atomic-force microscopy. (a) Topography, (b) control error, and (c)-(e) 3rd, 5th, and 8th harmonic images of a Pt–C film deposited on a glass substrate. The fundamental frequency f is 52.2 kHz. Reprinted with permission from Stark and Heckl, Rev. Sci. Instrum. **74**, 5111 (2003). Copyright © 2003 American Institute of Physics.

amplitude or frequency trigger the adjustment of the tip or sample height.[5,18,19] The use of higher harmonics of the driving frequency for feedback increased the signal-to-noise ratio of the detection system, improving the performance in liquids and the lateral resolution of the instrument (Fig. 1).[20–22]

Using the feedback mechanisms mentioned above to measure the sample topography, a wide variety of probes can access the different tip-sample interactions. The normal and lateral deflections of the AFM cantilever have been widely used as a way to measure liquids and materials mechanical[23] and friction properties (Fig. 2).[24] The use of modulated techniques in tapping mode provided an improved contrast mechanism for materials with different stiffness, damping, adhesion;[25–27] and even enabled the identification of individual atoms based on distinct chemical forces with the tip (Fig. 3).[28,29] Magnetic force microscopy probes the magnetic forces between a magnetic tip (coated with CoCr for example) and the sample magnetic domains in a non-contact mode.[30,31] The application of a frequency-modulated magnetic field led to the development of magnetic resonance force microscopy, which detects magnetic forces between a magnetic tip and the electron or nuclear spins at the sample surface.[32,33] In scanning thermal microscopy, the thermal properties of a heated sample can be probed by a platinum wire bent to form a tip or a Au/Pd coated silicon tip. The local heat flow from the heated sample to the tip is measured by the variation in electrical resistivity in the probe. The probe can also be used to heat the sample: the heat flow from the probe to the sample is then measured by resistivity variations or by the thermal expansion of the sample.[34,35]

The development of electrically conductive tips led to the development of numerous electrical feedback mechanisms[36] for electrochemistry microscopy,[37] electrostatic force microscopy,[38,39] Kelvin probe microscopy,[40] dielectric microscopy,[41] or Eddy current microscopy.[42] For

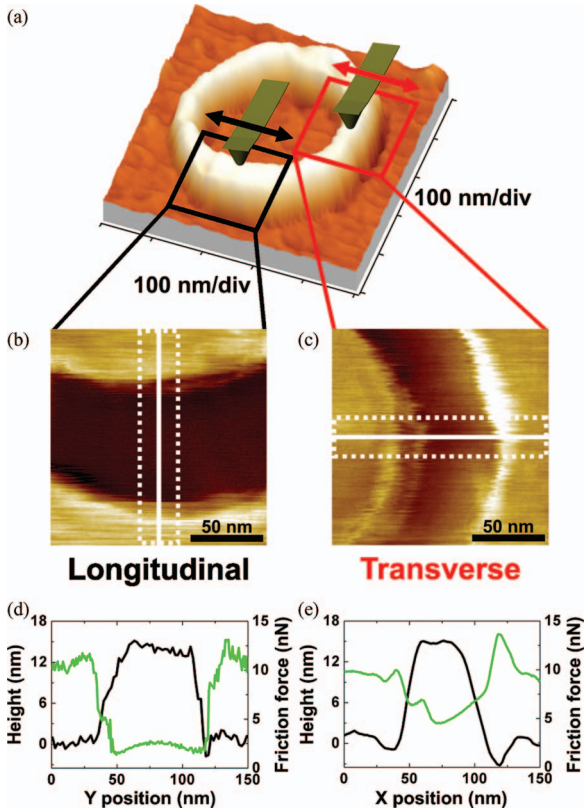

FIG. 2. Friction force microscopy on carbon nanotubes. (a) Topography AFM image. (b), (c) Friction images of the highlighted longitudinal (b) and transverse (c) sections of the nanotube. The fast scanning direction of the AFM tip is indicated by an arrow. In (d), (e), the black solid line is the topography profile along the white solid lines in (b), (c); the green solid line is the average friction force profile inside the area delimited by the dotted line in (b), (c). Reprinted by permission from Lucas *et al.*, Nat. Mater. **8**, 876 (2009). Copyright © 2009 Macmillan Publishers Ltd.

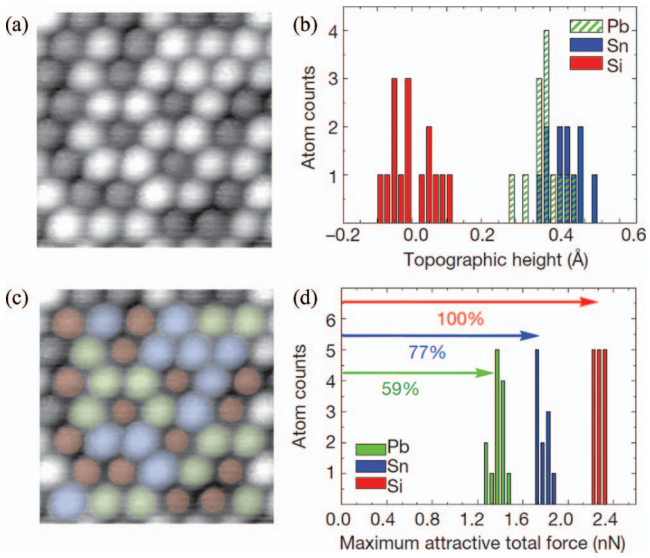

FIG. 3. Chemical imaging with atomic resolution. (a) Topography image of an assembly of Si, Sn, and Pb atoms on a Si(111) substrate. (b) Height distribution of the atoms in (a). (c) Local chemical composition of the image in (a). The Pb, Sn, and Si atoms are highlighted in green, blue, and red, respectively. (d) Distribution of maximum attractive total forces measured over the atoms in (a). Image dimensions are 4.3 × 4.3 nm^2. Reprinted by permission from Sugimoto *et al.*, Nature (London) **446**, 64 (2007). Copyright © 2007 Macmillan Publishers Ltd.

example, in Kelvin probe microscopy, a conductive tip first scans the sample to determine its topography. In a second scan, the tip is kept at a constant distance above the sample and a dc potential is applied to the tip to compensate for the electrostatic forces and potential difference between the sample and tip. To measure the small electrostatic forces, an amplitude- or frequency-modulated approach is used where an additional ac electrical excitation is applied to the tip close to the cantilever resonance frequency.[36,40] Scanning electrochemical microscopy has provided valuable insight in charge transfer mechanism at surfaces and electrochemical reactions.[37,43,44] For a more exhaustive list of feedback mechanisms recently developed to study individual atoms and molecules, the readers are encouraged to consult Ref. 45.

C. Spatial resolution

Imaging the topography of atomically smooth surfaces at atomic resolution was demonstrated with STM.[46,47] Scanning tunneling hydrogen microscopy was recently developed by placing a hydrogen or deuterium molecule in the tunneling junction at low temperature. In contrast to conventional STM which probes the local electronic density of states, scanning tunneling hydrogen microscopy resulted in images of the atomic structure of single molecules[45,48] and even their intermolecular interactions (Fig. 4)[49] at atomic resolution.

In addition to the topography, considerable efforts were made to improve the spatial resolution of images characterizing the chemical and physical properties of the sample. For example, in magnetic force microscopy, the spatial resolution is mainly limited by the area of the magnetized section of the tip and the tip-sample distance. To address these issues, two fabrications processes were developed to fabricate sharper tips with a smaller magnetized section. In the first process, a commercial silicon tip is coated with a 50–100 nm layer of CoCr. A carbon cap is then placed on the tip apex by electron beam deposition. The carbon cap acts as a mask when the magnetic layer is etched by ion beam milling, leaving a small magnetic particle at the apex protected by a thin carbon layer. The second process involves the growth of a carbon needle at the apex of a silicon tip. A thin magnetic film and a carbon mask are then deposited on one side of the carbon needle. The magnetic film on the silicon tip is then etched by ion beam milling. The prepared tips resulted in a lateral resolution below 10 nm.[31] Another way to improve the resolution is to shield the tip from long-range interactions, such as electrostatic and capillary forces. In piezoresponse force microscopy, this can be achieved by immersing the sample and the tip in water. The ions in the solution effectively screen the tip from long-range electrostatic interactions. Using this technique, the domain walls in polycrystalline lead zirconate-titanate ceramics were imaged with a resolution of 3 nm.[50]

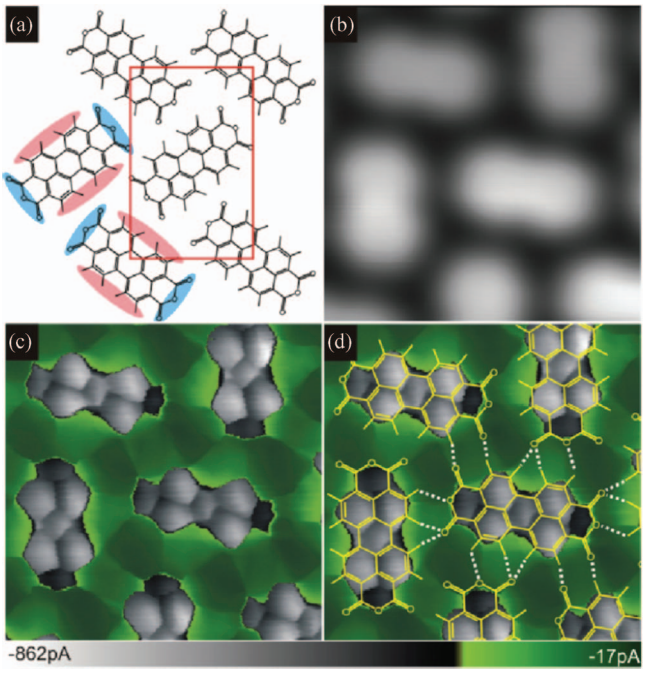

FIG. 4. Scanning tunneling hydrogen microscopy (STHM) images of 3,4,9,10-perylene-tetracarboxylic-dianhydride (PTCDA) on Au(111). (a) Structure model, molecular orientation, molecular quadrupole moment, and the unit cell of PTCDA. (b) Conventional STM image in constant height mode. (c) STHM image. (d) Superposition of (c) with the structure in (a). White lines mark possible hydrogen bonds. Image dimensions are 25 × 25 Å^2. Reprinted with permission from Weiss *et al.*, J. Am. Chem. Soc. **132**, 11864 (2010). Copyright © 2010 American Chemical Society.

Further improvements in the resolution and signal-to-noise ratio were made possible by modulating the tip movement with an excitation of set amplitude and frequency.[21] The contact area between the tip and the sample can be controlled accurately in modulated techniques. Such an approach applied to modulated nanoindentation enabled the study of elastic deformation in carbon nanotubes by keeping the indent depth below 1 nm.[23] Magnetic resonance force microscopy was used to image the proton spin density in an individual tobacco mosaic virus with a resolution better than 10 nm.[33] Doping levels in a doped field-effect transistor were measured by scanning capacitance microscopy with a sub-10 nm resolution.[51]

The collection of multiple force-distance curves at a high frequency in ultrahigh vacuum enables the characterization of the sample chemical composition at atomic resolution, by probing the site-specific chemical forces between the sample and the tip.[28,29] This approach was applied to identify individual Si, Pb, and Sn atoms in an alloy surface. The atoms cannot be distinguished by topography. To identify individual atoms, characteristic force-distance curves were first collected on Si/Pb and Si/Sn alloy surfaces before the analysis of a more complex Si/Sn/Pb alloy surface.[28] The chemical forces between different atoms were also distinguished by curves of the tip frequency shift as a function of the tip-sample distance. Operating at a low temperature of 6 K, non-contact AFM was used to image the chemical forces in graphite with sub-nm resolution.[29]

III. RAMAN SPECTROSCOPY

A. Principle

Raman spectroscopy is a laser spectroscopy technique that probes the vibrational states of gases, liquids, and solids. When the sample is illuminated by a monochromatic light of

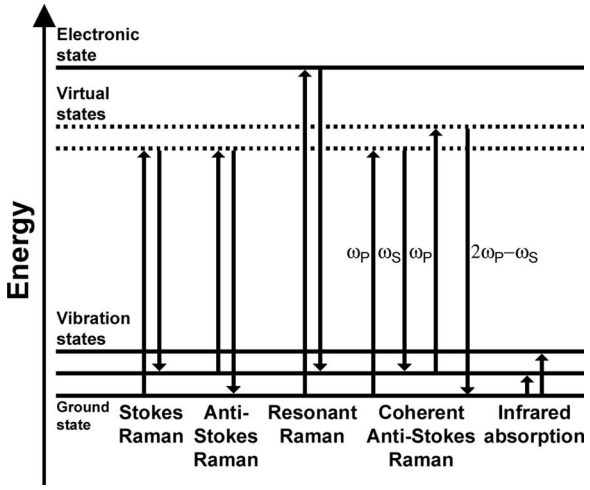

FIG. 5. Energy diagram of electronic transitions involved in different types of vibrational spectroscopy. For coherent anti-Stokes Raman spectroscopy, ω_P indicates the pump laser frequency, and ω_S the Stokes laser frequency.

frequency v_0, most of the light is scattered elastically at the same frequency v_0 (Rayleigh scattering). Some of the light is scattered inelastically at a different frequency. The inelastic scattering process is the Raman effect (Fig. 5).[52,53] In contrast to infrared spectroscopy which is sensitive to molecular dipole moment variations, a molecule is Raman active only if polarizability variations are involved. For example, the polarizability of the C=C bond changes dramatically with stretching, so the Raman scattering is strong, while the infrared absorption is weak.[53]

In infrared spectroscopy, the electrons absorb the incident photons with an energy equal to the difference of energy between the ground state and the excited vibrational state. In Raman spectroscopy, the electrons are first excited to a virtual electronic state, the result of the distortion of the electronic cloud around atoms due to the electric field of the incident light. The excited electrons then relax with the emission of photons with an energy different from the incident wavelength (inelastic scattering). In a Stokes Raman scattering process, the emitted photon has a lower energy than the incident photon, and the electron in the molecule gains an energy quantum hv_i (with the creation of a phonon). In an anti-Stokes Raman scattering process, the emitted photon has a higher energy than the incident one, and the electron in the molecule loses an energy quantum hv_i (with the annihilation of a phonon). This is possible if the initial state is an excited vibrational state, and the final state is the ground state or a lower excited vibrational state.[53]

The anti-Stokes Raman intensity depends on the population of the first excited vibrational state, thus its intensity is usually much weaker than the Stokes intensity. In non-resonant conditions, the anti-Stokes/Stokes intensity ratio depends on the temperature and is proportional to the Boltzmann factor:[53]

$$\frac{I_{anti-Stokes}}{I_{Stokes}} = \frac{(v_0 + v_i)^4}{(v_0 - v_i)^4} \exp\left(\frac{-hv_i}{kT}\right),$$

where $I_{\text{anti-Stokes}}$ and I_{Stokes} are the anti-Stokes and Stokes Raman intensity functions respectively. T is the temperature, h and k are Planck's and Boltzmann's constants respectively. The anti-Stokes/Stokes ratio is used in non-resonant conditions to measure the sample temperature.[54]

When the laser excitation energy matches an absorption band of the sample, the Raman signal becomes resonant and is significantly enhanced due to the increase in the electronic density of states. This enhancement is large enough for single-molecule detection in the case of individual single-wall carbon nanotubes.[55] These resonant effects are particularly evident in carbon nanotubes: only the radial breathing modes of carbon nanotubes with an absorption band matching the excitation wavelength appear on the Raman spectra.[56] The resonance conditions and therefore the Raman intensities of the radial breathing modes change when the excitation wavelength changes[56] or when the nanotube electronic bands are shifted by mechanical stress.[55–57] Resonant Raman spectroscopy provides a way to reduce the fluorescence background, while increasing the signal-to-noise ratio for enhanced chemical sensitivity.[58]

Unlike fluorescence spectroscopy, Raman spectroscopy is a non-destructive technique that does not require any sample preparation or deposition of labels. Raman spectroscopy can be applied to solutions and biological samples in aqueous environments, since the signal loss from water absorption is reduced compared to infrared spectroscopy. It complements the surface SPM analyses with subsurface analyses made possible with confocal Raman spectroscopy[59] and spatially offset Raman spectroscopy.[60] In addition to applications in pharmaceuticals, it found applications in archeology for the authentication of artifacts.[61] The technique is now robust and portable enough to be used in space for biomolecular analyses.[62]

B. Coherent anti-stokes Raman spectroscopy (CARS)

The sample is illuminated by two coherent and synchronous monochromatic beams, a pump laser of frequency v_1 and a Stokes laser of frequency v_2, with $v_1 > v_2$. When v_1-v_2 matches the frequency of an excited vibrational band, the intensity of the scattered light of frequency $2v_1$-v_2 (anti-Stokes frequency) is significantly enhanced compared to spontaneous anti-Stokes Raman scattering. CARS is usually implemented with two colinear lasers, since this geometry results in higher resolution and image quality.[63] Since CARS is a four-wave mixing process, high peak power femtosecond laser pulses are usually focused on the sample with a high NA objective.[64–68] In contrast to the spontaneous Raman effect, the CARS signal is proportional to the Stokes beam intensity, to the square of the pump beam intensity and to the square of the number of molecules. The tight focus means that the CARS signal comes from a much smaller volume, leading to the reduction of the background signal[69] and enabling 3D sectioning of the sample.[65] The CARS signal is at a lower wavelength than the excitation and thus can be separated from the fluorescence background.[63] The technique was applied in biology for the label-free chemical imaging of DNA,[68] cells,[64,65,69] live tissues,[70] and for the spectral analysis of flames.[66]

The use of ultrafast lasers also led to the development of femtosecond CARS, where a pump and a Stokes laser excite the sample to a higher vibrational state, and a probe laser, which is identical to the pump laser, generates the anti-Stokes scattered light. The Stokes beam is not colinear with the pump and probe beams to eliminate the CARS signal that is generated when the pump and Stokes beams are synchronous. CARS spectra were collected for different delay times (temporal resolution of a few tens of femtoseconds) between the probe/Stokes beams and the pump beam. The femtosecond CARS data exhibit a transient response that is characteristic to the analyte.[67]

The presence of a non-resonant background has limited the widespread application of CARS. This non-resonant background is the result of electronic resonances excited by third-harmonic generation. It offers no contrast for the sample and can distort CARS spectra.[65,69,71] It becomes stronger as the pump and Stokes laser pulses become shorter.[71] This non-resonant background can be reduced by controlling the laser polarization,[69] a pulse-sequenced detection scheme[63] and by the excitation of the sample with near-infrared lasers or picosecond laser pulses (Fig. 6).[65,72] An interferometric approach was also proposed to eliminate the non-resonant background. A single laser pulse of 120 nm bandwidth with controlled phase and polarization excited the sample to produce two spectral interference CARS signals along two distinct linear polarizations. The difference between the two spectra is similar to the spontaneous Raman spectrum where the non-resonant background is removed.[71]

Another technique, frequency modulation CARS, requires two pump lasers of different wavelengths that are switched at high frequencies of the order of 1 MHz by a Pockels cell[73] and/or an optical parametric oscillator.[74] For example, one of the pump lasers can be tuned to a vibrational mode of interest, while the other would be tuned to a spectrally flat region. A half-wave plate makes the two pump lasers polarized perpendicularly. Switching between the two pump lasers results in the amplitude modulation of the CARS signal, which can be demodulated with a lock-in amplifier. The non-resonant background which is independent of the pump laser wavelength is thus eliminated.

Advances in spectral focusing have improved the CARS spectral resolution.[72] Indeed, the spectral resolution depends on the bandwidth of the pump and Stokes lasers and it decreases with the use of shorter femtosecond pulses. The use of chirped broadband laser pulses improved the spectral resolution and the vibrational excitation frequency can be simply tuned by the time delay between the pump and Stokes lasers. Recently, spectral focusing was combined with frequency-modulation of the pump laser to achieve background-free CARS with high spectral resolution. Broadband pulses from a Ti:sapphire laser was split into a pump and a Stokes laser. A Pockels cell modulates the polarization of the pump beam at a frequency of 100 kHz. A polarizing beam splitter then directs the pump beam along one of two different paths depending on the polarization of the incident beam toward two mirrors at slightly different distances. The Stokes beam goes through a glass rod to match the group velocity dispersion of the pump laser and is reflected off a mirror located on a translation stage

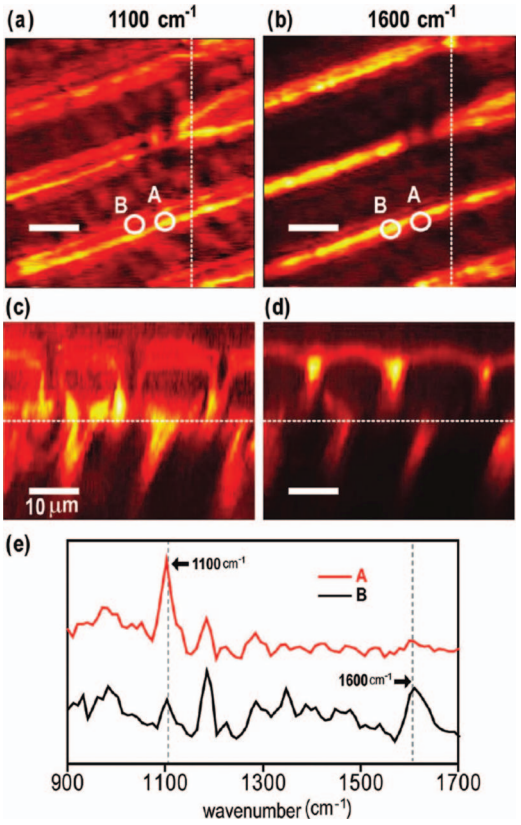

FIG. 6. Frequency modulation coherent anti-Stokes Raman scattering (FM-CARS) images of (a) cellulose (1100 cm^{-1}) and (b) lignin (1600 cm^{-1}) in a corn leaf. (c), (d) Depth profiles of (c) cellulose and (d) lignin are along the dotted lines in (a) and (b). The scale bar is 10 μm. (e) FMCARS spectra at the positions labeled A and B in (a) and (b). Reprinted with permission from Chen *et al.*, J. Phys. Chem. B **114**, 16871 (2010). Copyright © 2010 American Chemical Society.

to select the vibrational excitation frequency. The reflected pump beam is recombined with the Stokes beam, and the scattered CARS signal from the sample is demodulated by a lock-in amplifier at the frequency of the Pockels cell. By sweeping the time delay of the Stokes beam, background-free CARS spectra that look like spontaneous Raman spectra were obtained from oils, membranes, skin and plant cells over a 800-1700 cm^{-1} window with a spectral resolution of 20 cm^{-1}.[72]

C. Surface-enhanced Raman spectroscopy

Anomalously high Raman intensities were observed for pyridine deposited on silver electrodes[75–78] and on gold/silver particles.[79] The adsorption of the analytes on the surface of a noble metal can enhance significantly the Raman signal, by a factor as large as 10^{14}, leading to the development of surface-enhanced Raman spectroscopy (SERS).[80] Later, SERS was also applicable on iron[81] and copper[82] surfaces. The large enhancement of the Raman signal is generally attributed to two mechanisms. The first is an electromagnetic effect and the second is from a chemical effect which involves a charge transfer from the metal to the first layer of adsorbates.[83]

The electromagnetic effect comes from the surface plasmon resonance of metal nanoparticles, when they are excited by a laser with the appropriate wavelength.[84,85] The surface

plasmons are coherent collective excitations of surface conduction electrons. When the surface is irregular and exhibits edges and nanoscale roughness, the induced electric field of the plasmon becomes localized. The intensity of the electric field enhancement depends on the surface material and the topography of the substrate.[86] The enhancement of the Raman signal then scales with the fourth power of the electric field enhancement.[87] The enhancement factor was measured for silver nanostructures with different sizes and localized surface plasmon resonance wavelength. The maximal enhancement was observed when the resonance peak is located in a 120-nm-wide spectral window that includes the excitation wavelength and the Raman-scattered wavelength.[88]

The chemical effect involves a charge transfer between the metal nanoparticle and the adsorbate that modifies the polarizability of the adsorbate.[82,89,90] Another proposed enhancement mechanism is the modulation of the metallic surface polarizability by the adsorbate vibration.[87] Band shifts in DNA nucleobases and in C_{60} were attributed to these chemical effects that depends on the distance between the metal nanoparticle and the adsorbate.[91–93] The observation of a chemical enhancement depends on the analyte adsorbed on the gold/silver nanostructures.[87] Surface-enhanced resonant Raman data of Rhodamine 6G adsorbed on silver colloid nanostructures and aggregates compared well with finite-difference time-domain simulations that only accounts for the electromagnetic enhancement and neglected the chemical enhancement.[94]

The "hot spots" where the Raman signal is significantly enhanced are usually found at the gaps between nanoparticles in aggregates,[95–98] but rough single particles can also produce hot spots.[84,85,99–101] Signatures of single-molecule detection were likely to be found in the gap between two or more nanoparticles.[102] Aggregation also leads to the shift and broadening of the plasmon resonance.[103]

To understand the origin of SERS, researchers have characterized thoroughly the structure of the nanoparticles and tried to relate it to the enhancement factor as a function of size, shape, aspect ratio, orientation, gap between particles, chemical composition, coating thickness, and optical properties. Another approach was to design particles and substrates with various lithographic techniques and chemical processes to optimize the enhancement of the Raman signal and ensure the reproducibility of the SERS signals: nanoporous structures,[104] hole arrays,[105] nanorod arrays,[106,107] gratings,[108] dimers, and single particles.[109–111]

The electromagnetic enhancement in SERS was studied with colloidal systems, where the size of the nanoparticles and their aggregation can be controlled chemically. By varying the reagents concentration, gold nanoparticles of diameters ranging from 10 to 100 nm were synthesized. UV/Vis spectroscopy showed that the surface plasmon resonance redshifts as the diameter increases and the experimental results were simulated successfully using Mie theory.[112] The Raman enhancement factor is maximum when the surface plasmon resonance matches the excitation wavelength. This was confirmed by electron energy-loss spectroscopy for a monolayer of pyromellitic anhydride deposited on atomically smooth copper and silver surfaces.[82]

Experimental studies of pairs of nanoparticles showed that the surface plasmon resonance and therefore the enhancement factor are extremely sensitive to any changes in the gap distance.[113] Nanoporous gold substrates or silver hole arrays were manufactured by lithographic or chemical processes to understand how the gap between nanostructures affects the enhancement. For example, the enhancement factor of Rhodamine 6G increased as the characteristic length in nanoporous gold decreased.[104] SERS measurements of 6-mercaptopurine on silver hole arrays revealed a dependence on the hole diameter.[105] Arrays of gold dipole antennas composed of nanorod pairs of various lengths at different gap widths were prepared by electron lithography. An increasing blueshift of the plasmon resonance was observed as the gap width increases.[107]

The shape of the nanostructures also affects the plasmon resonance maximum. By varying the reaction conditions during the reduction of $AgNO_3$ in ethylene glycol, nanoparticles in the shape of a cube, sphere, bar, and rice grain can be deposited. The SERS intensity was found to be lower in spheres and higher in cubes and rice grains due to high-curvature surfaces.[110] The plasmon resonance was characterized for silver nanoparticles of various shapes, nucleated around gold seeds. It was found that the particles with a circular cross section have a plasmon resonance peak in the blue (400–500 nm), whereas those with a pentagonal or triangular cross section exhibit a maximum in the green and red (500–700 nm). An increase in particle size results in a redshift of the resonance peak.[109] A heat treatment at 200°C resulted in the rounding of the corners for the triangular particles and a blueshift of the resonance peak.[109] The nanoparticles larger than 100 nm in diameter can take multiple shapes and their absorption and scattering spectra can exhibit strong variations in intensity and linewidth. In contrast, the optical properties of smaller nanoparticles are less subject to shape variations.[111] The aspect ratio of gold nanorods also influences the plasmon resonance position. Absorption spectra of gold nanorods with aspect ratios ranging from 1.5 to 3.5 exhibited a transverse plasmon resonance peak around 520 nm and a longitudinal resonance peak that redshifted from 570 nm to 700 nm as the aspect ratio increased.[114] Plasmon spectroscopy on dimers found that the plasmon resonances are also influenced by differences in diameter between the two particles and their core-shell structures.[115]

The particles with non-spherical shapes give rise to anisotropic polarization effects. In the cases of cubes and rice grains, the SERS intensity is highest when the incident polarization is along a line connecting sharp features such as the cube corners or the grain ends.[100,110] Tomographic plasmon spectroscopy on a single non-spherical gold nanoparticle revealed variations in the plasmon resonance peak positions and linewidths in three dimensions. A polarization study in three dimensions showed the dependence of the resonance peak intensity on the incident polarization.[116] For pairs of nanostructures, the enhancement factor depends also on the relative orientation of the two nanostructures. For two nanorods at a fixed distance between centers of mass, the frequency shift exhibited a $\cos^2\theta$ dependence with the rotation angle θ of one

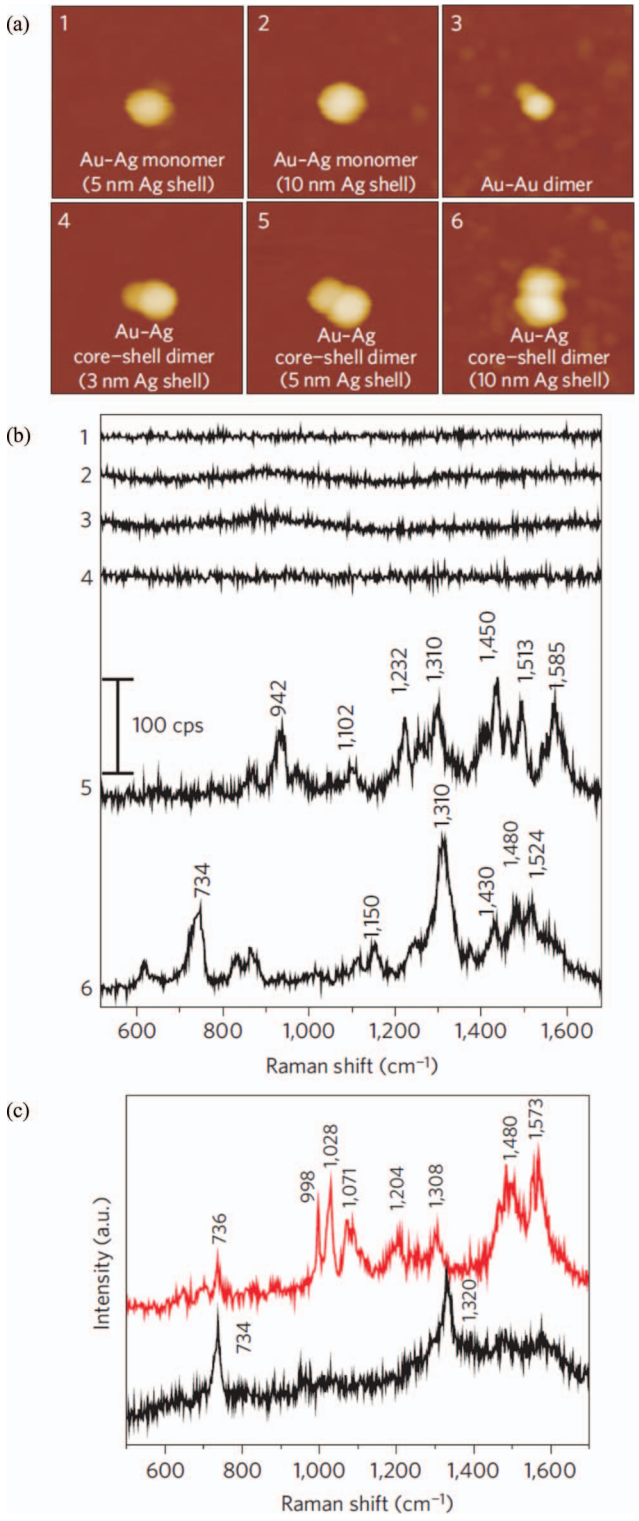

FIG. 7. SERS activity of Au/Ag core-shell nanoparticles and heterodimers. (a) AFM topography images of the synthesis products. Image dimensions are $1 \times 1\ \mu m^2$. (b) SERS spectra collected from the corresponding nanostructures. (c) Raman spectra of Cy3-modified oligonucleotides (red/upper line) and Cy3-free oligonucleotides (black/lower line) in NaCl-aggregated silver colloids. Reprinted by permission from Lim *et al.*, Nat. Mater. **9**, 60 (2010). Copyright © 2010 Macmillan Publishers Ltd.

of the nanorod. The blueshift of the plasmon resonance was maximum for $\theta = 90°$.[107] These orientation and polarization effects were also observed on nanostructures in the shapes of spheres, cubes and triangles (Fig. 7).[110,117]

IV. COMBINATION OF SPM WITH RAMAN SPECTROSCOPY

A. Motivation

AFM has been used extensively for the characterization of topography, mechanical,[118] tribological,[24] and transport properties[36] at the nanoscale. In parallel, Raman spectroscopy is a powerful tool for the characterization of chemical composition, crystal structure and orientation,[119–121] mechanical deformation,[57] thermal properties,[122] and defects.[119,123] The combination of SPM and Raman enables the characterization of the structure-properties relationship with excellent spatial resolution. Confocal Raman spectroscopy can also provide depth information. The ability to control the position of the tip and the sample with piezoelectric elements enables the rastering of the sample during imaging, while the tip can be used as a probe for mechanical, electrical, or optical measurements.

Such a combination has been used to identify proteins at the surface of individual cells.[124] The overlay of AFM and Raman images made possible the imaging of mechanical stresses in carbon nanotubes,[125] the doping level in individual poly(3-methylthiophene) nanotubes,[126] and the chemical composition of thin films of polymer blends.[127] The complex interplay between morphology, defects, growth direction, and mechanical properties was elucidated in individual ZnO nanobelts.[119,123]

B. Side vs. axial illumination

The combination of a SPM and optical microscope requires a robust, often customized, stage to reduce mechanical noise. The stage must accommodate for objective changes, support the AFM and stay open for additional equipment, such as hot stages, electrical contacts, liquid cells, etc. The different optical configurations for AFM-Raman microscopy combinations are discussed. The various methods to orient the incident laser polarization with respect to the AFM tip axis are also discussed. The polarization orientation will be particularly important for the application of tip-enhanced Raman spectroscopy, discussed in Sec. V.

1. Excitation wavelength

The deflection of the SPM probe is typically measured by a red or infrared laser beam bouncing off the back of the cantilever. This laser is much weaker that the excitation laser used for the Raman, but is much stronger than the Raman signal. Depending on the Raman excitation wavelength, a band pass or long pass filter must be placed before the photodetector of the SPM to block the scattered light. A short pass filter in front of the Raman spectrometer would also block the laser from the SPM.[128]

Illumination of the cantilever by a Raman laser in the infrared, 785 nm for example, can lead to the perturbation of the AFM scan. When silicon nitride cantilevers were used, the bending of the cantilever due to laser heating interferes with the approach of the tip and the operation of the AFM.[129] Silicon cantilevers did not suffer from the same problem

and could operate with the Raman laser beam. However, the strong laser focus also causes a torque of the cantilever that can be measured by the lateral deflection of the cantilever.[129] It is preferable to use two lasers spectrally isolated for the AFM and Raman measurements. For Raman measurements with infrared excitation, a few AFM manufacturers now offer lasers at 980 and 1064 nm.

2. Bottom illumination

In this configuration, an AFM is placed on top of an inverted optical microscope. The excitation laser illuminates the tip in transmission from below through a high NA objective and the signal is collected through the same objective. For tip-enhanced spectroscopy (Raman, infrared, fluorescence or second-harmonic generation), the tip is raster scanned across the laser spot to find the tip position yielding the highest intensity. The tip position is then fixed. A second nanopositioner for the sample is then used to scan the sample. The feedback of the AFM is used to maintain a constant distance between the sample and the tip.

This geometry allows for the tight focusing of the laser beam around the tip apex and can enhance the near-field signal with respect to the far-field signal. However, in this configuration, the samples have to be thin or transparent. The laser can penetrate a micrometer deep into the sample, adding to the far-field contribution. The use of condensers is possible above the inverted microscope with a large aperture above the tip. However, the mechanical stability of the AFM is then compromised.

For tip-enhanced Raman spectroscopy, the position of the hot spot on the metal-coated tip with respect to the laser focus and the incident polarization play an important role in the enhancement factor. When the incident laser polarization is linear, the enhanced electromagnetic field around a SERS nanostructure or a metal-coated tip presents two lobes on the sides of the nanostructure or tip.[128,130] This spatial shift can be compensated by moving the tip/nanostructure, or by using higher laser modes.[131,132] As for the polarization, the tip-enhanced Raman spectroscopy is generally maximal when the incident laser polarization is aligned along the tip axis. Such a polarization configuration is difficult to achieve in a bottom illumination configuration. One way is to convert the linearly polarized incident laser into a radially polarized laser using two half-wave plates and use a high numerical aperture objective to focus the light onto the tip apex. Another method is to use parabolic mirror objectives to convert a radially polarized light to a light polarized along the tip. The mirror focuses light with polarization along the tip onto a tight spot. The technique has a collection angle of 180°. Those mirror objectives have no chromatic aberrations, and can be used in liquids or in vacuum at all temperatures (Fig. 8).[133–138]

3. Side illumination

In such a configuration, the Raman signal is collected in a reflection mode.[7,139–145] Opaque samples, such as crystals and metals can be analyzed. However, an objective with a long working distance is necessary, which means low NA, typically between 0.28 and 0.5.[141] Most of the scattered light is reflected off the sample away from the objective, meaning the signal collection is generally poor. Also, the laser beam spot is wider than at normal incidence and covers an area much wider than the near-field around the tip apex. The shadowing effect and retardation effects from side illumination can become an issue.[146] The far-field contribution is much larger when the tip is retracted than when the tip is in the close vicinity of the sample.[147]

The angle between the incident polarization and the substrate normal can be easily adjusted in this configuration (Fig. 9).[129,142,143] It is particularly easier to have an incident polarization parallel to the tip axis. An AFM-Raman microscope combination has the Raman excitation laser at grazing incidence, about 3° off the sample plane.[129] Numerical simulations have shown that the optimal enhancement of a metallic

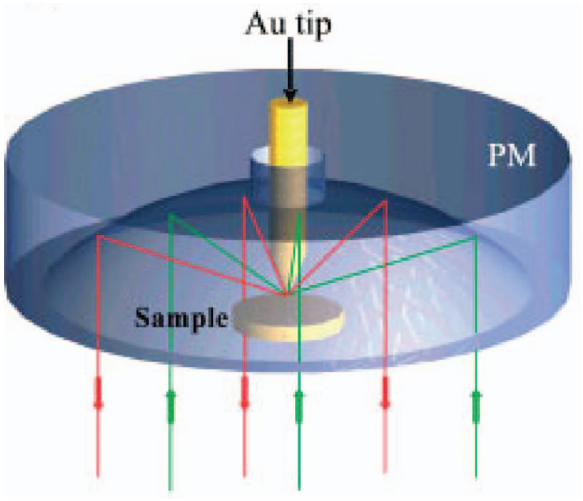

FIG. 8. Schematic of a parabolic mirror focusing a radially polarized laser beam onto the apex of a gold tip. Reprinted with permission from Zhang *et al.*, J. Raman Spectrosc. **40**, 1371 (2009). Copyright © 2009 John Wiley.

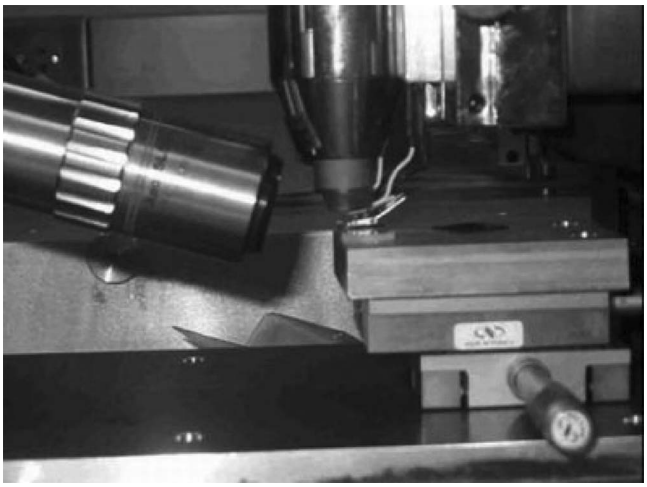

FIG. 9. Side-illumination of an AFM tip. The Raman signal is collected through the same objective, which is at an angle of 65° with respect to the tip axis. Reprinted with permission from Mehtani *et al.*, J. Raman Spectrosc. **36**, 1068 (2005). Copyright © 2005 John Wiley.

tip used for SERS is obtained when the tip is illuminated at an angle of between 40 and 70°.[128,144,148] The optimum incident angle varies with the tip geometry.[128]

A direct comparison between side- and bottom-illumination was performed using the same collection system. With the side illumination, the approach of a metallic tip yielded an apparent enhancement of the Raman signal and the fluorescence background by a factor 3. With the bottom illumination, the tip approach resulted mainly in an increase of the fluorescence background, with only a 20% increase in the Raman signal.[145]

Side illumination of a vertical tip not only reduces the signal collection efficiency, but its application is also complicated by the precise alignment of two separate light illumination and collection systems. An experiment design that involves top illumination with a tilted tip/probe increases the collection efficiency and improves the ease of use.[128,147]

4. Top illumination

The introduction of the tip between the sample and the objective requires a long-working distance objective with low NA. A drawback to this set-up is the shadowing effect from the tip. This is particularly true in AFM, since the tip is not generally at the end of the cantilever, but about 10 μm from the edge.[149] The tip partially blocks the light scattered from the sample and movements of the tip affects the far-field contribution to the signal. However, the variations of the far-field signal are reduced in this configuration compared to the side illumination configuration, since the cantilever moves along the laser beam.[147] Variations of the far-field signal were negligible for cantilever movements smaller that 500 nm.

Shadowing effects can be reduced with the use of a transparent cantilevered glass fiber.[128,147] The tip can be bent so that the tip axis forms an angle of 60° with the sample surface.[128] The off-axis alignment of the tip also allows for the orientation of the laser linear polarization to be almost along the tip axis.[128] A similar approach combines a higher numerical aperture (0.7) and an STM feedback mechanism with a silver tip of radius 75 nm oriented at a 30–50° angle with respect to the sample surface. The use of a high NA objective improved the collection efficiency and the spatial resolution of Raman images for opaque samples (Fig. 10).[150]

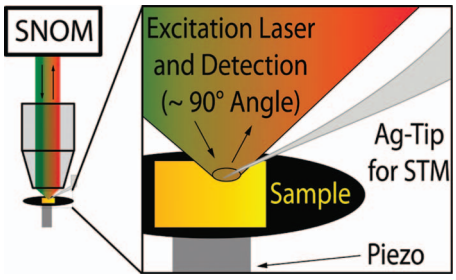

FIG. 10. Top-illumination of an angled tip on the sample surface. Reprinted with permission from Stadler *et al.*, Nano Lett. **10**, 4514 (2010). Copyright © 2010 American Chemical Society.

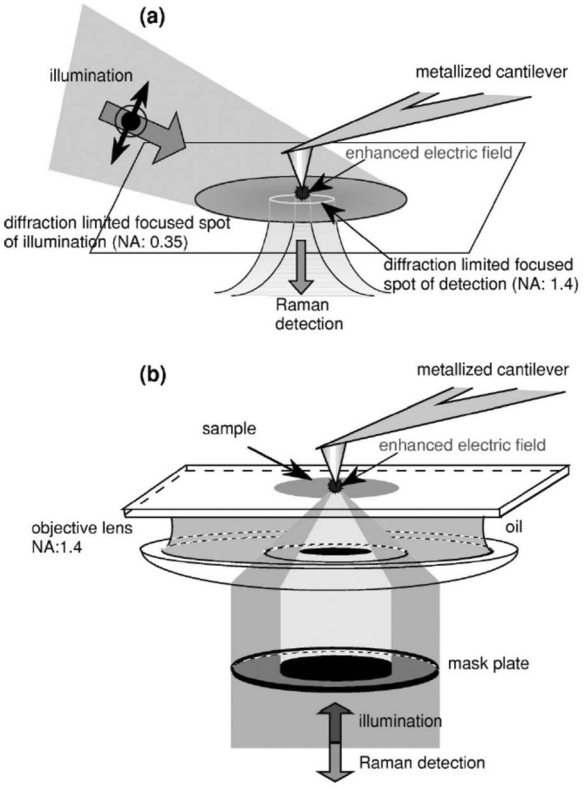

FIG. 11. Schematics of tip-enhanced Raman spectroscopy systems with (a) side-illumination and (b) focused evanescent field illumination. Reprinted with permission from Hayazawa *et al.*, J. Appl. Phys. **92**, 6983 (2002). Copyright © 2002 American Institute of Physics.

5. Multiple excitation or collection systems

In a first example, the sample can be illuminated from below (objective NA 1.4) or from the side at an incidence angle of 80° with the substrate normal (objective NA 0.35). The signal is collected in both configurations with the same system by the objective below (Fig. 11).[145]

In the second example, an AFM tip was illuminated by the excitation laser at a 45° incidence angle. The signal can be collected in a backscattering geometry using the same objective as for the excitation, or with the inverted microscope and its objective placed below the sample. The signal from each objective is detected by its own spectrometer and CCD camera. This configuration can accommodate transparent and opaque samples.[149]

C. Scanning near-field optical microscopy (SNOM) with aperture

The spatial resolution of Raman microscopes is related to the excitation laser beam spot size. And the best focus of the laser beam is defined by Abbe's diffraction limit of $\lambda/(2NA)$ where NA is the numerical aperture of the objective. In order to produce optical and Raman images beyond the diffraction limit, probes with an aperture smaller than the light wavelength were used in close proximity to the sample to direct the excitation light or collect the signal.[151] Two operating modes are used: the illumination and the collection modes. In the illumination mode, the sample is illuminated locally by the

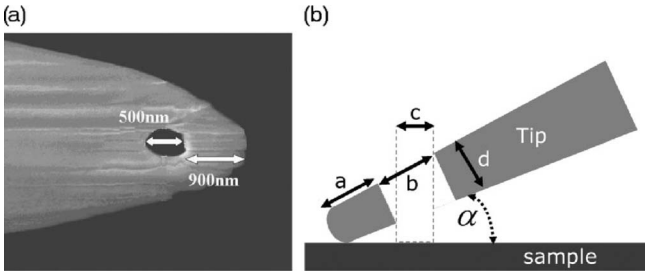

FIG. 12. (a) SEM image and (b) schematic of a tungsten cantilever with an aperture milled by focused ion beam. Reprinted with permission from Mai *et al.*, J. Raman Spectrosc. **39**, 435 (2008). Copyright © 2008 John Wiley.

tapered probe and the signal is collected in the far-field. Due to the small aperture, the laser light that reaches the fiber end is a localized evanescent wave.[152,153] In the collection mode, the sample is illuminated in the far-field and the signal is collected locally by the fiber probe. High surface sensitivity is possible with a total internal reflection illumination.[154] SNOM can also be implemented in a reflection mode where the probe and the objective are located above an opaque sample.[155]

The probe is typically a tapered optical fiber made of glass or quartz. A metallic film, typically aluminum, coats the fiber sidewalls to confine the light inside the fiber.[135,155] Focused ion beam can be used to flatten the fiber end.[151] Indeed, protrusions on the fiber end can produce artifacts due to crosstalk between the near-field optical and the topography images.[156] The fiber end still has an external diameter of a few hundreds of nm, which makes it difficult to keep the tip close to the surface of a rough sample.[155] An alternative to the glass fiber is the AFM tipless cantilever[157] or silicon tip.[158] An aperture can be opened by focused ion beam through a tungsten cantilever (Fig. 12)[157] or silicon tip.[158] The silicon tip coated with chromium and aluminum exhibited an enhanced transmission and resistance to thermal degradation.[158]

SNOM in the visible range was demonstrated in 1984 by two independent groups.[152,153] In one report, an array of apertures was manufactured by electron-beam lithography on a silicon substrate coated with a 50 nm thick Au/Pd film.[153] In the other report, a 30 nm radius tip was etched out of a quartz crystal. The sides of the crystal were coated with layers of Cr/Al or Ag/Au.[152] Transmission of a 488 nm laser light was possible through apertures as small as 30 nm in diameter.[153]

To maintain a constant high resolution, the tip-sample distance is generally controlled with a piezoscanner by a shear-force and tapping mode feedback mechanism. The end of the fiber or pipette is also used to collect topographic images of the surface, using the shear-force feedback mechanism.[159,160] Using an excitation at 488 nm and an aperture of 70 nm, the spatial resolution degraded significantly beyond a tip-sample distance of 5 nm. For a distance above the wavelength, the resolution became comparable to the diffraction limit. A spatial resolution of 12 nm was achieved in transmission with a 514 nm excitation and an aperture of 70 nm.[155] SNOM was applied for Raman microscopy on dyes,[135] thin films,[158,161] and semiconductors such as SiGe.[157] Lines of various widths etched in SiGe by focused ion beam were imaged by SNOM and a lateral resolution of 200 nm was achieved.[157]

SNOM can deliver spatial resolution at the nanoscale, but the technique suffers from the low signal collected, particularly for Raman spectroscopy.[155,162] The light transmission coefficient through an aperture in a conducting plane was predicted to depend on the aperture diameter a and the wavelength λ as $(a/\lambda)^4$.[163] The evanescent wave in the illumination mode also decays exponentially at the tip apex. An optimal probe geometry should have a short tapered section with a high taper angle.[164] One way to increase the sensitivity of SNOM-Raman was to exploit the SERS effect. Thin films of Rhodamine 6G and tris(bipyridine)ruthenium(II) were deposited on silver nanoparticles and detected by SNOM-SERS.[158,161]

The low collection efficiency and long acquisition times has led to the use of metallic tips to enhance the signal with apertureless SNOM.[165,166] Unless specified otherwise, the following sections will focus on apertureless near-field spectroscopy/microscopy. For complete reviews on aperture SNOM, its applications, and the fabrication of probes, the readers are invited to consult Refs. 151 and 167–170.

V. TIP-ENHANCED RAMAN SPECTROSCOPY

The Raman process has a cross section of 10^{-30} cm^2, 10^{10} smaller than for infrared spectroscopy and 10^{14} smaller than for fluorescence.[171] SERS substrates can increase significantly the Raman signal, but the SERS response is inhomogeneous due to the irregular shapes, sizes, and roughness of nanoparticles and clusters. The concept of using a metallic tip to enhance the laser spectroscopic signal was first introduced by Wessel.[99] The metallic nanostructure can enhance and confine the electric field around it. The Raman intensity would then be enhanced by the fourth power of the field enhancement factor, similarly to the SERS effect. A tip-induced enhancement eliminates the need for a reliable SERS substrate.[172,173] The same tip would be used for all positions of the same sample, enabling reproducible chemical imaging.[99] Early Tip-Enhanced Raman Spectroscopy (TERS) studies showed a significant enhancement of the Raman signal from strong scatterers, such as laser dyes,[91,174] carbon nanotubes,[130] fullerenes,[91,175] and diamond particles.[176]

The enhancement factor is mostly controlled by the shape and size of the tip apex. Hot spots, where the electric field is significantly enhanced, are usually generated in regions of high curvature. Reported enhancement factors range from a few hundred to 10^{15} for SERS,[100] potentially making the Raman signal stronger than the fluorescence signal.[177] A small tip radius keeps the enhancement of the electric field local around the tip apex and can improve the spatial resolution down to 10 nm.[91,130,174,175,177]

The gap between the tip and the sample must be controlled accurately with a piezoscanner and feedback mechanism to keep the enhancement factor stable. The ability to move the sample and the tip with independent piezoelectric elements enables the precise positioning of the laser beam with respect to the tip apex and the rastering of the sample for imaging. It allows the laser to be locked on a hot spot

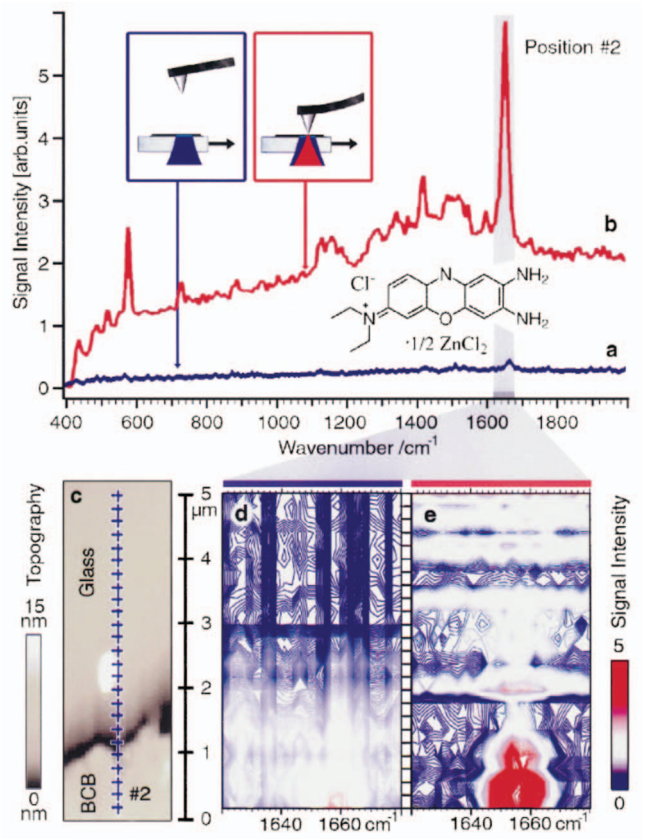

FIG. 13. Tip-enhanced Raman spectra of brilliant cresyl blue with the tip (a) retracted and (b) in contact with the sample. (c)-(e) Series of 25 Raman spectra across a sample boundary indicated in (c), with the tip (d) retracted and (e) in contact with the sample. Reprinted with permission from Stöckle *et al.*, Chem. Phys. Lett. **318**, 131 (2000). Copyright © 2000 Elsevier.

around the tip apex, and the sample can be then scanned independently to obtain an image with optimum enhancement (Fig. 13).[178]

Raman data can also be collected at a specific tip-sample distance with sub-nanometer resolution by time-gated methods (Figs. 14 and 15).[19,179] In one method, the tip oscillated in the normal direction in tapping mode at defined amplitude close to its resonance frequency. The Raman intensity decayed exponentially as the tip-sample distance increased, thus the Raman signal detected by an avalanche photodiode oscillated at the same frequency as the tip driving force. The signal was sent to a dual-gated photon counter that was triggered by the tip driving force at two different time gates that corresponded to the times where the tip was closest to the sample (signal included near- and far-field contributions) and farthest from the sample (only far-field contribution). The near-field signal was obtained by subtraction. Data collection for different time gates resulted in the measurement of the near-field Raman signal as a function of the tip-sample distance.[179] However, this technique can only acquire the Raman signal at a fixed wave number. To collect the whole Raman spectrum at a precise tip-sample distance, a time-gated illumination technique was implemented where the tip was illuminated stroboscopically at the same frequency as the tip driving excitation. The same excitation activated the tip oscillation and an acousto-optic modulator that acted as a shutter

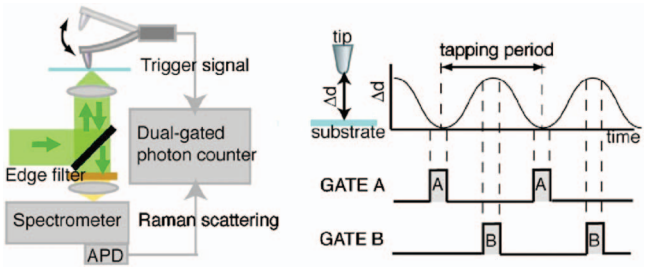

FIG. 14. Schematic of the dual-gating photon counting scheme for a tip-enhanced Raman system using tapping-mode AFM. Reprinted with permission from Yano *et al.*, Appl. Phys. Lett. **91**, 121101 (2007). Copyright © 2007 American Institute of Physics.

for the excitation laser. A time-gate of set delay and duration defined the tip-sample distance range over which the Raman spectrum was collected.[19]

A. Field enhancement

As in SERS, field enhancement in TERS has an electromagnetic and a chemical origin. Two different electromagnetic mechanism can be distinguished: the surface plasmon resonance and the antenna effect. When the laser excitation energy matches the surface plasmon resonance, the electric field is enhanced at the tip apex due to the localization of surface charge densities. In the antenna effect, when the tip is illuminated by a laser polarized along the tip axis, the electric field is significantly enhanced at the apex and confined in its vicinity.[180,181] The chemical enhancement contribution is explained by a charge transfer, that affects the electronic band structure and the Fermi level of the adsorbates, thus creating more intermediates electronic states where resonant Raman

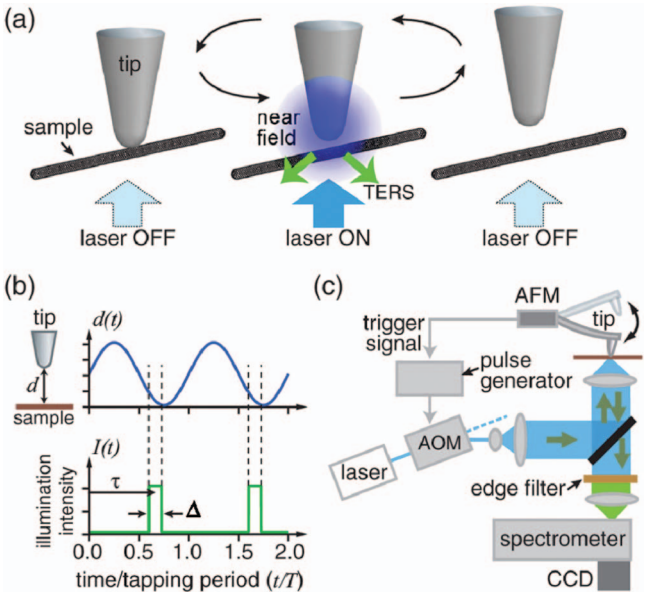

FIG. 15. (a) The tip and sample are illuminated only for a predecided tip-sample distance. (b) Schematic of the sinusoidal oscillation of the tip and the synchronized opening of the time gate. (c) Schematic of the tip-enhanced Raman spectroscopy system using a tapping-mode AFM and acousto-optic modulator for time-gated illumination. Reprinted with permission from Ichimura *et al.*, Phys. Rev. Lett. **102**, 186101 (2009). Copyright © 2009 American Physical Society.

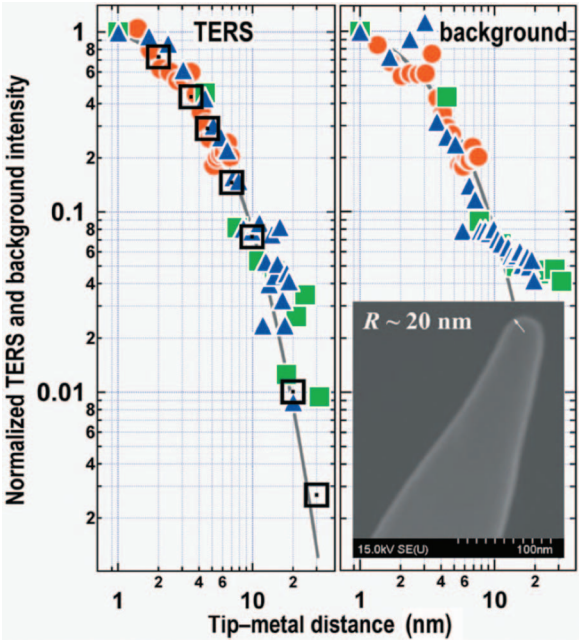

FIG. 16. Normalized TERS intensity of coadsorbed guanine and ClO_4^- and background intensity at different tip-sample distances. The inset is a scanning electron microscope image of the STM tip. The TERS data were collected at different tip retraction velocities: 1.6 nm/s (squares), 0.32 nm/s (triangles), 0.16 nm/s (circles). Reprinted with permission from Pettinger *et al.*, Phys. Rev. B **76**, 113409 (2007). Copyright © 2007 American Physical Society.

processes can be stimulated. This principle was demonstrated in adenine crystals where unique bands have been observed in TERS.

The field enhancement from the laser irradiation of a metallic tip has been calculated by solving Maxwell's and Helmholtz's equations, taking into account the tip shape and size. Such calculations can also predict any shift in the surface plasmon resonance due to the tip size and shape. These simulations only take into account the electromagnetic enhancement and not the chemical enhancement. However, TERS is performed in most cases in non-contact mode, where the distance tip-sample is above 1 nm, so the chemical enhancement is neglected.

In the spontaneous Raman effect, the scattered Raman signal is generated from a change in polarizability induced by the excitation laser. However, in TERS, the electric field enhancement can vary dramatically depending on the distance between the sample and the tip (Fig. 16). A polarizability gradient is then induced by the field enhancement around the tip. Dramatic band shifts and intensity variations can be attributed to the varying distance between the tip and sample, especially when dealing with single molecules.[148,182–185]

The simple approach of the tip near the sample can produce multiple reflections of the excitation laser and confine the light to the tip apex, leading to an enhancement of the Raman signal. To make sure that the enhancement is from near-field effects, an enhanced spatial resolution comparable to the tip radius and a dependence of the enhancement factor on the tip-sample distance must be demonstrated.[186]

The experimental Raman enhancement cannot be deduced only from the increase in intensity. It has to take into account the size of the beam spot and the size of the enhanced volume under the tip. The experimental enhancement factor takes into account the enhancement of the near field signal compared to the far field signal, and also the volume probed by each contribution.[142] Often the enhancement factor E is calculated using

$$E = \frac{I_{near}}{I_{far}} \times \frac{A_{far}}{A_{near}},$$

where I_{near} and I_{far} are the near-field and far-field Raman intensities, A_{near} and A_{far} are the enhanced area under the tip and the spot size, respectively.

The experimental enhancement factor is typically several orders of magnitude higher than the apparent enhancement factor, which is the ratio between the intensity when the tip is in contact and the intensity when the tip is retracted.[187] Shadowing effects can affect the accuracy of this factor, since the far-field contribution varies with the tip-sample distance.[142] Also, the volume probed by the far-field signal is difficult to determine due to the uncertainty on the depth considered: it should be the product of the beam spot area by the sample thickness, laser penetration depth or depth of field of the optical system, whichever is the smallest.[142] Another problem is the uncertainty on the depth to which near-field effects are seen. To determine it, enhancement factors were measured on CdS films of various thicknesses. As the thickness increased, the ratio between the near-field volume and the far-field volume decreased. The enhancement factor was observed to decrease exponentially with the film thickness, with a characteristic depth, which was used to determine the near-field volume. This characteristic depth can vary as a function of the tip radius and the incident angle of the laser.[142] It also includes the contribution of multiple reflections in the enhancement factor.[187] A more consistent method to assess the enhancement factor was proposed, based on TERS intensity line profiles across one-dimensional nanostructures such as carbon nanotubes. Such a line profile exhibits a sharp near-field signal over a broad far-field signal that has the same width as the far-field resolution. The near-field and far-field contributions per unit length of the nanotube can be determined.[187]

Numerical simulations of the field enhancement were performed to assess its dependence on the tip-sample, distance, tip shape, and polarization configuration. To calculate the local field enhancement, the Maxwell equations have to be solved analytically. This is only possible for simple tip geometries, such as a sphere or cylinder. Due to complex tip/sample geometries and dielectric properties, simplification of the equations or numerical simulations were used to find solutions. Different computational methods were developed, such as the finite element method (FEM),[148,188] the finite-difference time-domain method (FDTD),[139,189–194] the scattering theory,[195] Green's function technique,[196,197] multiple multipole method,[198] and the boundary element method.[196,197] Another simplification is the quasistatic approximation.[199] FEM was applied extensively on complex tip/sample geometries. FDTD is well suited in spectroscopy, since the whole spectrum can be computed simultaneously. However, FDTD requires the knowledge of the appropriate law of dispersion and a very small cell size (cell

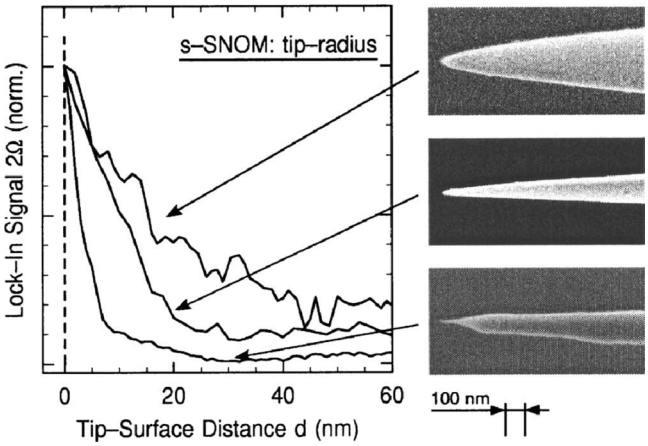

FIG. 17. Tip-sample distance dependence of near-field scattered light for three tips with radii of curvature of about 20 nm (top), 12 nm (middle), and smaller than 5 nm (bottom). Reprinted with permission from Raschke and Lienau, Appl. Phys. Lett. **83**, 5089 (2003). Copyright © 2003 American Institute of Physics.

side 100 times smaller than the tip diameter) to describe the field enhancement around sharp tip features.[200] Using the methods mentioned above, the field enhancement was calculated as a function of the distance to the tip[191–193,195,199] and wavelength[148,190,191,195,199] for various tip geometries. The methods based on solving the Maxwell equations are only able to assess the electromagnetic enhancement of the Raman signal. The chemical effect on the field enhancement is ignored.

The intensity of the light scattered from the tip is highly dependent on the tip-sample distance, exhibiting an exponential decay behavior as the tip-sample distance increases (Fig. 17).[19,130,179,184,201] Using a modulated technique, the Raman *G* band intensity was measured for a single carbon nanotube as a function of the tip-nanotube distance. The Raman signal decreased exponentially with a characteristic length scale of 12 nm that was constant at different locations along the nanotube.[179] The length scale over which the near-field scattered light decayed was measured using three tips with radii of 20, 12, and less than 5 nm. The sharpest tip resulted in a strong localization of the near-field signal (fast decay with tip-sample distance) and an enhancement of the overall signal. The signal amplitude depended on the vertical composition of the sample (metallic coating thickness) over a depth scale comparable with the penetration depth of the incident laser.[201]

More important than the enhancement factor per unit volume is improving the contrast between the far-field and the near-field signal. This is particularly an issue when the sample is placed over a thick substrate. Despite the large enhancement factors reported in the literature, technical advances are still required in apertureless methods to enhance the signal and reduce noise. One way to further increase the enhancement factor is to apply tip-enhanced resonant Raman spectroscopy. This technique was applied to adenine crystals which have an absorption peak around 280 nm. The sample was excited at a close deep-ultraviolet wavelength of 266 nm. The tip was coated with a 20–25 nm thick aluminum film that is SERS active at 266 nm. The enhancement factor observed for the resonant adenine crystals was larger than the one for the nonresonant crystal violet. Deep-ultraviolet excitation also has the advantage of separating spectrally the fluorescence and the Raman signal.[202]

To reduce the far-field background signal, modulated techniques were used where the tip-sample distance oscillated at a high frequency and an amplitude small compared to the tip radius. The resulting optical signal was demodulated at the modulation frequency or higher harmonics. Then, only the signal corresponding to short tip-sample distances were recorded, while the far-field signal was eliminated.[179,201,203] Another way to eliminate the far-field background was to use stroboscopic illumination with a phase-sensitive photon counter. A series of gate pulses synchronized with the tip deflection with adjustable phase and duration enabled the detection of photons only when the tip was in close proximity to the surface.[19,149] However, caution should be exercised that no image artifacts are introduced when these modulated techniques are used. Even after the demodulation at high-order harmonics, a residual background contribution can sometimes subside in the collected signal. A SNOM study showed that imaging the amplitude and phase of the demodulated signal can eliminate near-field image artifacts, assuming that the demodulated signal is a linear combination of the near-field and background signals.[146]

B. Spatial resolution

Numerical simulations predict the spatial resolution would be higher in an apertureless approach. The lateral resolution should be only limited by the tip radius. Finite-difference time domain simulations showed that the resolution from a 25-nm radius gold tip placed at 2 nm above the sample should be better than 10 nm.[193] Finite-element and finite-difference time domain simulations showed that the spatial resolution is also a function of the tip-sample distance.[148,204] As the tip-sample decreases, the enhancement factor increases and the spatial resolution improves. Varying the excitation wavelength from 350 to 650 nm has little effect on the optimal resolution.[204] At short distances below 2 nm, the resolution is expected to be better than the tip radius. At distances longer than 10 nm, the resolution is imposed by the tip radius.[148] Simulations on the spatial resolution in water show a similar trend with the tip-sample distance. However, the improvement at small distances is less dramatic.[148]

Experimentally, the resolution is also affected by the hysteresis and creep of the AFM scanner.[186] The enhancement factor is very sensitive to the position of the tip with respect to the laser focus.[155] If a hot spot exist on the tip, its location under the tip apex or on the tip side must match the center of the laser focus for optimal enhancement and resolution. Therefore, the precise positioning of the tip is essential.[155]

The location and intensity of these hot spots also depend on the polarization configuration of the experiment.[191] A consequence of this position and polarization dependence is the possible dependence of the resolution on the sample roughness. Sharp edges or protrusions on the sample would couple differently with the enhanced electric field around the tip

apex, depending whether the sample feature is under the tip or on the tip side, complicating the estimation of the resolution in Raman images.[147,205]

Some of the best resolutions reported were obtained for carbon nanotubes[130,206] and a laser dye,[207] which have high Raman scattering cross sections. A lateral resolution of about 10 nm was obtained for carbon nanotubes with tips of 10-15 nm radius.[130,206] A resolution of 15 nm was reported for brilliant cresyl blue with a 20-nm radius tip.[207] To further improve the resolution, it was proposed to apply a mechanical stress on the sample, which leads to Raman band shifts for the molecules immediately under the tip. Line scans of the Raman band shifts on a carbon nanotube and an adenine crystal showed a lateral resolution of 4 nm.[208] Advances in tip fabrication would also improve the resolution. The silver waveguide at the center of the photonic crystal cavity can focus the laser-induced surface plasmon at the tip of the waveguide of radius smaller than 5 nm. Raman images of a silicon nanocrystal/SiO_x trench exhibited a spatial resolution better than 7 nm.[209]

C. Temporal resolution

High temporal resolution is desirable to study dynamic events. Piezoelectric scanners suffer from nonlinear effects such as hysteresis, drift, creep, and aging. Shorter acquisition times for the Raman spectra would limit the impact of drift and are necessary for the accurate registry on nanostructures and long biomolecules.[185] High temporal resolution also becomes necessary to account for temporal fluctuations of TERS spectra.[106,210–212] For example, time-lapse series of TERS spectra from malachite green at the same spot showed an exponential decay of the intensity due to bleaching with a time constant of 40 ± 5 s for a laser fluence of 3×10^4 W/cm^2.[210] TERS spectra of clusters of adenine molecules showed significant variations in intensity and band position, which were attributed to molecular orientation changes that affected the polarization conditions for tip enhancement.[212] In SERS, wild variations of the signal were reported for molecules located in a gap smaller than 10 nm between plasmonic nanostructures. This can be explained by the motion of the adsorbates in and out of the enhanced volume under the tip, or the desorption from the tip.[106] Other explanations include variations in the tip-sample distance, contamination with carbonaceous materials, and breakdown of the selection rules.[210,211]

Increasing the laser power would reduce the exposure time, but high laser power would lead to sample damage.[211] Advances in the development of more sensitive detection systems decreased dramatically the exposure time without sacrificing the signal-to-noise ratio.[213] For the strongest scatterers, such as silicon and carbon nanotubes, the typical acquisition time ranges from 100 ms[206] to a few seconds for strain maps.[214] The same acquisition time is used for laser dyes, such as malachite green (Fig. 18).[140] Tip-enhancement reduced the exposure time for small molecules, such as benzenethiol,[215] and self-assembled monolayer of thiophenolate[216] to a range of 10–60 s. In order to reduce the exposure time even further, the TERS signal can be integrated over a wider spectral band. This enabled the Raman imaging of ferroelectric domains in $BaTiO_3$ nanorods of 6 nm height with a collection time of 10 ms per pixel.[217]

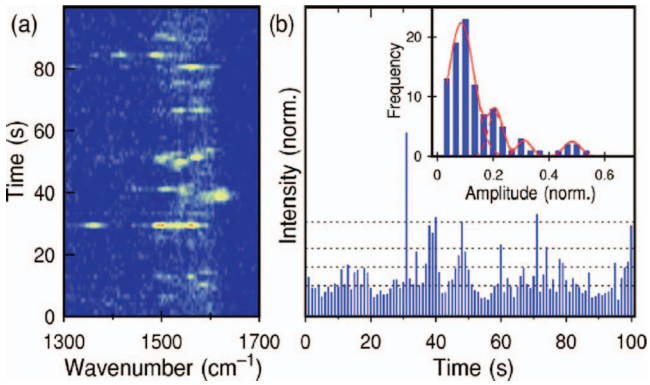

FIG. 18. (a) Time series of tip-enhanced Raman spectra for a submonolayer of malachite green dye. (b) Temporal variation of the intensities of the integrated 1480–1630 cm^{-1} Raman band. The inset is a histogram of the Raman intensity distribution. Reprinted with permission from Neacsu *et al.*, Phys. Rev. B **73**, 193406 (2006). Copyright © 2006 American Physical Society.

Recent advances in ultrafast laser spectroscopy led to the development of Raman spectroscopy with femtosecond resolution. It was applied to biomolecules and for the study of the transient excited states involved during the photoinduced *cis-trans* isomerization of stilbene.[218]

D. Polarization

Experimental data and numerical simulations have shown that the field enhancement depends on the polarization of the incident laser.[9,186,191,219] If the electric field vector of the incident light is perpendicular to the tip axis, the free electrons on the metallic surface will be driven away from the tip apex to the side surfaces of the tip. If the electric field vector of the incident laser is along the tip axis, the free electrons will be confined to the tip apex, leading to a significant field enhancement.[191,219] A direct comparison between *p* (along the tip axis) and *s* (in the sample plane) polarizations was done with the same collection system. With the *p* polarization, an apparent enhancement factor of three was observed on Rhodamine 6G, whereas a slight intensity decrease attributed to shadowing effects was observed with the *s* polarization.[145]

Most Raman spectra are collected in a backscattering geometry where the tip is illuminated from the bottom and the laser propagation direction is along the tip axis. When a low NA objective is used, the polarization remains mostly perpendicular to the tip axis. However, when an objective with a high NA is used, the polarization is not necessarily perpendicular to the tip axis anymore.[167] At the focus plane, some components of the polarization might be along the tip axis. In a backscattering geometry, a radial polarization of the light produces stronger polarization components along the tip axis, leading to an improved enhancement of the Raman signal.[220] A linearly polarized laser beam can be converted to a radially polarized Hermite-Gaussian mode with a mode converter that consists of two half-wave plates.[147,221] The radially polarized light resulted in an enhancement factor at least five

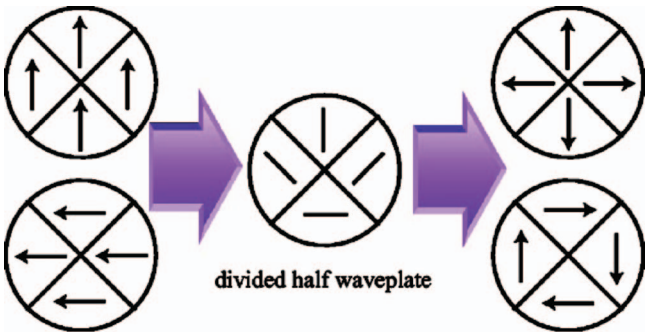

FIG. 19. Conversion of a linearly polarized light into a pseudoradial or azimuthal polarized light with a divided half-wave plate. Reprinted with permission from Hayazawa *et al.*, Appl. Phys. Lett. **85**, 6239 (2004). Copyright © 2004 American Institute of Physics.

times larger than the one obtained with linearly polarized light (Fig. 19).[147,222] The radially polarized light also produced a more uniform enhancement across the laser focus compared to the linearly polarized light.[147] However, the transverse component of the polarization still dominates compared to the polarization component along the tip axis.[131]

The polarization can also be tuned to reduce the far-field background signal. The near-field indeed can allow the emission of the Raman signal in a usually forbidden polarization state.[223] The tip will preferentially enhance the polarization component of the signal parallel to the tip axis. By placing an analyzer that would partially block the far-field signal, the near-field signal can still be collected (Fig. 20).[142,144,219,224–226] By optimizing the orientation of the incident and analyzed laser light with respect to the tip axis, the ratio between the near-field and the far-field contributions was increased from 0.5 to 12 in silicon.[144] However, this technique requires knowledge of the sample material and the crystallographic face being presented to the incident laser. Therefore, it may not apply for other materials such as CdS.[142]

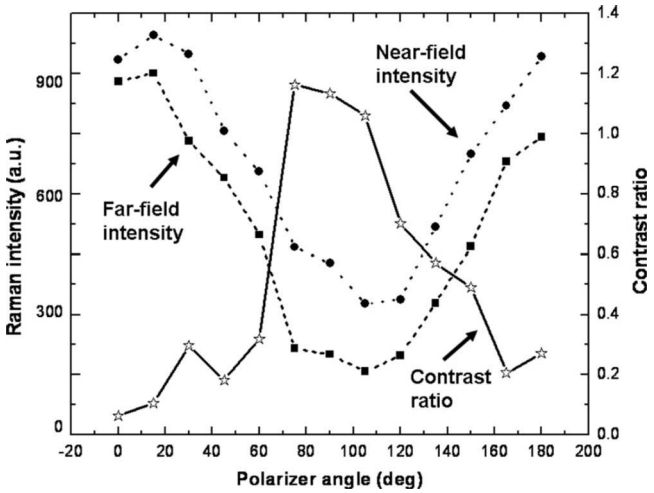

FIG. 20. Far-field intensity (squares), near-field TERS intensity (diamonds) for a silicon substrate (520 cm^{-1} band), and contrast ratio (stars) as functions of the polarizer angle. The analyzer was kept perpendicular to the tip axis. Reprinted with permission from Yi *et al.*, Rev. Sci. Instrum. **79**, 073706 (2008). Copyright © 2008 American Institute of Physics.

E. Tip geometry

Two frequently used techniques for the fabrication of metallic tips are electrochemical etching and metal evaporation on AFM tips. In the electrochemical etching method, a voltage is applied between a metallic gold wire and a ring-shaped metallic electrode, both immersed in concentrated hydrochloric acid solution.[227,228] Using this method, tips of radius 30 nm were produced in a reproducible way.[9] Silver tips were also made using different etching methods.[229,230] In the metal evaporation method, a thin film is deposited by evaporation to produce AFM tip coatings with various roughnesses.[171,230] The deposition of the metallic coating can however affect the performance of the cantilever and bend it to the point where it is unusable. Focused ion and electron beams can be used to further control the morphology of the metallic tip to enhance the antenna effect and possibly tune the surface plasmon resonance.[231]

Another way to produce a metallic coating is the growth of colloidal nanoparticles in solution, where a metal is reduced to produce a suspension of nanoparticles of various shapes and sizes.[129,232–234] For a review of methods for attaching or depositing nanoparticles on an AFM tip, the readers are invited to consult Ref. 235. Glass nanorods can also be used as templates for the deposition of a metallic coating.[236] The metallic coating is usually 20–50 nm thick. Thinner coatings are not as mechanically stable. For gold-coated tips, a thin layer of chromium is first deposited on the silicon cantilever for a better adhesion.[142] There might also be a coating thickness dependence of the enhancement. For an excitation at 514.5 nm, optimum enhancement was observed with a silver layer 40–60 nm thick or a 70–100 nm thick gold layer.[142] Metallic nanorods at the apex of AFM tips can increase resolution, but the low production yield and difficulty to place the nanorod in a reproducible way are major obstacles.[235] Early work on tip preparation produced tips that yielded enhancement only 10%–40% of the times.[129,130,176]

Most AFM tips used in TERS are coated with silver or gold. Even the initial TERS studies involved SNOM fiber tips coated with gold or a gold/palladium film.[152,153] The imaginary part of permittivity in silver is smaller than in gold, yielding higher enhancement factors.[237] However, silver tends to oxidize in air, whereas gold is more chemically stable. A degradation of the enhancement factor is observed for silver tips after a few days, while gold coated tips can yield reproducible enhancement factors for a few months.[142,226] A 2-3 nm thick Al_2O_3 layer can reduce the degradation of silver-coated tips without affecting the enhancement factor.[238] For STM-Raman combinations, silver- or gold-coated tungsten tips or gold tips can be used. Tungsten tips are more resistant to wear and deformation than gold tips (Fig. 21).[149] Tungsten tips are prepared by electrochemical etching, followed by the deposition of a silver coating (about 40 nm thick) by a sputtering process.[226]

The field enhancement factor was calculated as a function of excitation wavelength for tips of different materials, such as gold, silver, aluminum, tungsten, and silicon. The gold tip produced the largest enhancement with the highest chemical stability. Aluminum also yielded a large enhancement,

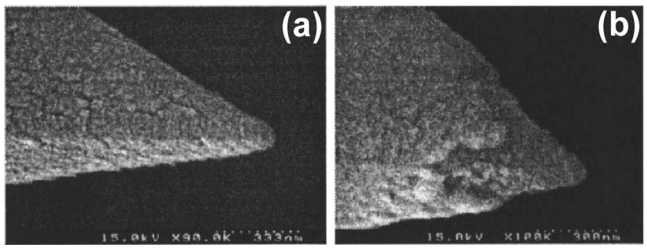

FIG. 21. SEM image of a gold-coated AFM tip (a) before and (b) after approximately 10 h of AFM imaging in tapping mode. Reprinted with permission from Nieman *et al.*, Rev. Sci. Instrum. **72**, 1691 (2001). Copyright © 2001 American Institute of Physics.

but, in air, it is covered with an oxide layer which increases the aluminum-sample distance and inhibits the chemical enhancement in SERS/TERS.[189,197]

The material of the tip on which the metal coating is deposited also plays a significant role in the enhancement factor. The SERS signal from brilliant cresyl blue and malachite green was measured on silver-coated substrates of different compositions. It was found that the SERS signal increases as the refractive index n of the underlying substrate decreases. AlF_3 ($n = 1.4$) was found to produce stronger SERS signals than Si ($n = 4.4$), SiO_x ($n = 1.5-2.05$), and SiO_2 ($n = 1.5$) for a 488 nm excitation.[183] This result was confirmed with TERS spectra collected with silver-coated SiO_2 and silicon nitride ($n = 2.05$) tips. With similar coatings, the SiO_2 tip produced a stronger TERS signal from brilliant cresyl blue.[239]

The apparent enhancement factor is also influenced by the orientation of the incident laser beam with respect to the side faces of silver-coated pyramidal tips. A larger enhancement was observed when the laser reaches the tip normal to one of the side faces, compared to the case where the laser reaches the tip on an edge. However, the larger apparent enhancement was attributed to the fact that the side face acts as a mirror and only enhances the far-field contribution to the signal. In order to increase the ratio between near-field and far-field contributions, the incident laser should not be normal to a side face of the tip.[144]

The effect of tip radius on field enhancement below the apex was studied for various excitation wavelengths. A decreasing tip radius should create a lightning rod effect that leads to an increase in the field enhancement.[193,198,201] However, the surface plasmon resonance also depends on the tip radius size and therefore the effect of tip radius on field enhancement depends on the excitation laser and tip material.[148,190,193] Phase retardation effects must be accounted when the tip becomes larger than a fourth of the excitation wavelength.[189] Also, the electric field below the tip apex decays exponentially as $\exp(-d/R)$, where d is the distance from the tip apex and R the tip radius. The intensity, which is proportional to the fourth power of the electric field, decays faster as d increases when R is smaller.[148]

Theoretical studies and numerical simulations on the optimum geometry of the tip for field enhancement provided an insight on the role of each tip geometric parameter, such as aspect ratio, apical angle, and length. For example, there exists an optimal apical angle that depends on the tip length.[188,192] As for the length, cylindrical tips longer than 500 nm exhibit multiple resonances between 300 nm and 10 μm. The surface plasmon resonance with the lowest energy redshifts as the length increases from 100 nm to 1.5 μm.[194] The tip geometry far above its apex is also important for the optimization of the field enhancement. FDTD simulations on spherical, conical, and pyramidal tips showed a larger enhancement for the trigonal pyramid geometry. This was explained by the collection of charges at the side edges of the pyramid.[190]

The main problems are the mass production and reproducibility of TERS tips. As materials can contaminate the tip, those tips are likely to be replaced more frequently than usual AFM tips. The reproducibility issue comes also from the constantly evolving structure and conformation of the analyte around the tip apex. A change in conformation and distance can dramatically affect the Raman spectra. Repeated contact with the sample, especially in contact mode, can result in the premature wear and the variability of the Raman signal.[211] The tip quality is difficult to assess after production. Poor reproducibility in enhancement factors was observed for tips that seem identical in SEM.[183] SEM images cannot resolve nanoscale roughness on the tip, and additionally it cannot tell which side of the tip will be illuminated by the laser.

New ways to produce TERS tips compatible with the existing AFMs are being developed. Recently, a photonic crystal cavity and silver waveguide was manufactured at the end of a silicon nitride cantilever by ion milling and electron beam deposition. The silver waveguide at the center of the photonic crystal cavity focuses the surface plasmon polaritons generated by the laser excitation at the tip apex of radius smaller than 5 nm (Fig. 22).[209] In another manufacturing process, a

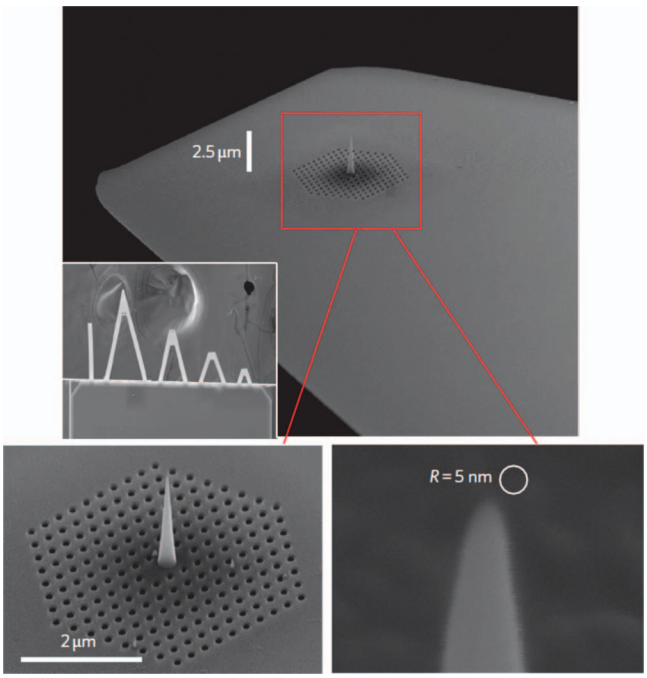

FIG. 22. (Top) SEM image of a tapered waveguide on an AFM cantilever. The inset shows the whole chip with multiple silicon nitride tips. (Bottom) Magnified images of the photonic crystal cavity and waveguide with a radius of curvature of 5 nm. Reprinted by permission from De Angelis *et al.*, Nat. Nanotechnol. **5**, 67 (2010). Copyright © 2010 Macmillan Publishers Ltd.

grating was etched by focused ion beam milling on the shaft of a gold AFM tip several micrometers above the tip apex. The appropriate selection of the grating pitch, tip cone angle and tip material enabled the propagation of surface plasmons over several micrometers and their focusing at the tip apex with a dipole moment aligned along the tip axis. TERS spectra collected from Malachite Green (633 nm excitation) and IR-125 (785 nm excitation) dyes with a side illumination of the grating and 90° sagittal collection of the scattered light from the tip apex exhibited a significantly reduced far-field background due to the smaller size of the emitter.[240]

F. Chemical sensitivity

Numerous experimental studies reported spectroscopic data at very low analyte concentration. However, the fact that rare hot spots exist does not mean that the spectra originated from single molecules. Often, the single-molecule sensitivity is inferred by the low analyte-to-silver colloid ratio or by strong variations in spectral intensity and profile.[8] But significant errors exist when the analyte concentration is smaller than 1 nM due to contamination or wall adsorption. Strong spectral variations can originate from desorption, variation of the molecule configuration or thermal heating.

AFM topography and height profiles were used as evidence of the presence of single molecules for RNA (Ref. 185) and carbon nanotubes.[130] To determine whether the signal is from single molecules or multiple molecules, a bianalyte approach was used where high concentrations of two dye molecules were mixed in a suspension of silver colloids.[241] Due to the high dye concentrations, a spectrum combining the two dye signatures should be expected. The detection of a pure signal coming from one dye would mean that the signal is coming from a small number of molecules. The probability of having multiple molecules of one dye in the same hot spot is very rare and decreases exponentially with the number of molecules. To determine whether the signal is from single molecules, a statistical criterion can be devised based on the variations of the frequency and intensity of hot spots as a function of the analyte concentration.[242] At low concentrations of Rhodamine dye (less than 5 nM), most of the signal was from single molecules, while at concentration higher than 50 nM, the signal was coming from multiple molecules.

Large TERS spectral variations were observed in malachite green isothiocyanate single molecules.[210,211] It was argued that the near-field spectral features of large organic molecules could not be altered significantly from the far-field features, since their electronic band structure would only be slightly affected by adsorption to a metallic particle.[211]

Temporal variations of the TERS spectra of adenine were attributed to variations of the molecule orientation.[212] The molecule orientation combined with the polarization configuration of the experiment would explain different intensity profiles for the TERS spectra (single molecule in a specific orientation) and the far-field spectra (collection of molecules in random orientation).[211]

Contaminants can produce a Raman signal as strong as the analyte. For example, amorphous carbon has a Raman scattering cross section four orders of magnitude higher than benzene.[243] The position of amorphous carbon bands varies wildly.[211,244]

G. Sample heating

Significant spatial and temporal variations in TERS spectra have been reported.[54,210,211,245] These variations have been attributed to variations in the tip-sample distance, adsorbate orientations, bleaching, contamination with carbonaceous materials, breakdown of the selection rules, but also laser heating which can lead to the degradation of the analyte.

TERS spectra can be very different from the far-field Raman spectra with the appearance of new bands, different band positions, and relative intensities. New bands and band shifts can correspond to the contamination from carbonaceous species and degradation of the analyte, respectively. Carbonaceous species have a much higher Raman cross section, so even traces can overwhelm the TERS spectra.[210,211]

Time-lapse series of TERS spectra from malachite green at the same spot for a laser fluence of 3×10^4 W/cm^2 showed a significant gradual intensity loss due to bleaching without the appearance of additional Raman bands that would indicate the formation of carbonaceous species. In contrast, time-lapse series of TERS spectra on photodegraded malachite green exhibit sudden changes in intensity and band positions, as well as the formation of previously unseen bands above 1750 cm^{-1}.[210]

The heating can lead to the chemical and morphological modification of the tip and sample due to thermal annealing. Repeated scans can lead to irreversible topography (roughness) changes, which affect the enhancement factor of a hot spot.[245]

Finite element analysis of the temperature distribution was performed on tips of various materials with a *p*-polarized light at 45° incidence and 1 mW/ μm^2 fluence. The temperature rise at the tip apex can be as high as 350 °C for a gold tip on a gold substrate in air. However, the half-cone angle of the simulated tip was only 10°, so a smaller temperature rise is expected for wider tips.[246] Temperature distributions in gold plasmonic nanostructures simulated with the bound element method showed that the temperature rise upon illumination depends on the structure shape, laser wavelength, and incident angle.[247]

The measurement of temperature variations was attempted by measuring the anti-Stokes/Stokes intensity ratio of Raman bands, which should be proportional to the Boltzmann factor. The temperature was found to rise with increasing laser power. Raman spectra collected with gold-coated tips at different laser powers showed a wavelength dependence that was consistent with the plasmon resonance of the coated tip.[54] However, the anti-Stokes/Stokes intensity ratio was also found constant over a wide range of laser intensities covering several orders of magnitude for crystal violet and colorless analytes. This behavior was explained by a modification of the resonance conditions due to charge transfers between the silver particles and the analyte.[248] The debate is still ongoing as to whether the apparently anomalous

anti-Stokes/Stokes intensity ratio is the result of pumping to excited vibrational states or sample heating.[249–251]

H. Tip-enhanced coherent anti-stokes Raman spectroscopy

Near-field CARS was attempted with an uncoated fiber probe with aperture. Chemical images from human hepatocytes exhibited a lateral resolution of 128 nm.[69] In order to improve the spatial resolution and the signal intensity, an apertureless tip-enhanced approach was adopted.[68,252] CARS spectra are collected by tuning the pump or the Stokes laser wavelength. For optimal apertureless tip enhancement, the pump wavelength should match the surface plasmon resonance of the tip.[253]

Since CARS is a coherent process, phase matching between the pump and the Stokes laser is essential. This is realized through colinear illumination and tight focusing of the laser spot through a high numerical aperture objective.[252] Powerful infrared pulses generated by Ti:sapphire or Nd:YAG lasers are used in tip-enhanced CARS. Picosecond laser pulses lead to reduced sample damage while maintaining a high peak power.[68,252] Infrared excitation reduces the background signals from nonresonant electronic excitations and fluorescence.[69,253] The CARS signal can be modulated to the tip vibration frequency to reduce the far-field and fluorescence background.[254] It is noted that photoluminescence from tips coated with noble metals can also generate a white light continuum background on CARS spectra (Fig. 23).[68]

Polarization effects on the intensity of the CARS signal were observed. For optimal enhancement factor, the pump and Stokes lasers have to be polarized along the tip axis. This can be accomplished with linearly polarized excitations and a high numerical aperture objective. However, in this configuration the maxima for the enhanced electric field are on the sides of the metallic tip apex.[68]

VI. COMBINATION OF SPM WITH OTHER SPECTROSCOPIC TECHNIQUES

Scanning probe microscopy was also combined with other optical microscopy/spectroscopy techniques, such as fluorescence, infrared, Förster resonance energy transfer (FRET), photoluminescence, and second harmonic generation. Indeed, not every sample is Raman active and other more sensitive spectroscopic techniques can be used for live imaging of cells and biomolecules.

A. Fluorescence microscopy

The overlay of AFM and fluorescence images combines the high resolution spatial information from AFM topography with the chemical information from fluorescence microscopy. The combination of these two complimentary techniques has been used in the biological sciences, where laser confocal scanning fluorescence microscopy allows for the live imaging of the cell components with different dye labels in three dimensions (Fig. 24).[255–258]

The excitation of localized surface plasmon resonances at the apex of a gold-coated tip resulted in the enhancement of the fluorescence signal.[255,259–261] For tip-sample distances above 5 nm, the fluorescence signal increases as the tip-sample distance decreases. Below 5 nm, the tip quenched the fluorescence signal and a signal drop was observed.[255,260] This was explained by the fact that the fluorescence rate is influenced by the enhancement of the local electric field and the

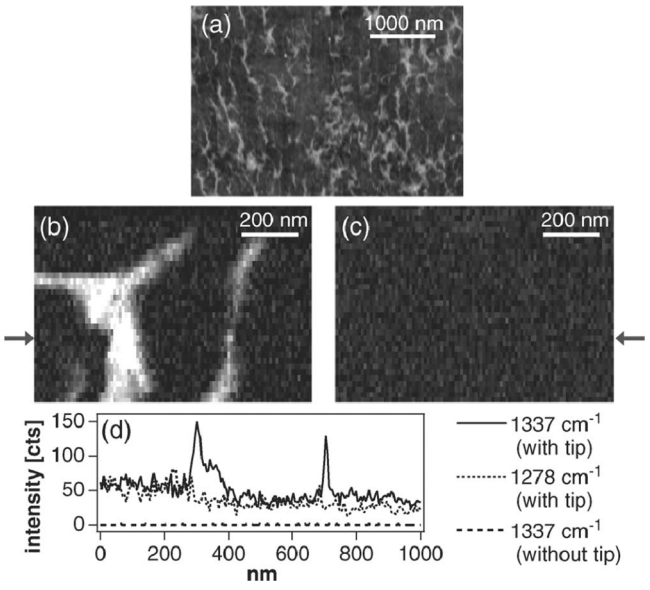

FIG. 23. (a) Topographic image of the DNA network. (b), (c) Tip-enhanced CARS images at the (b) on-resonant frequency (1337 cm^{-1}) and (c) off-resonant frequency (1278 cm^{-1}). (d) Intensity line profile for the horizontal line indicated by arrows. Reprinted with permission from Ichimura *et al.*, Phys. Rev. Lett. **92**, 220801 (2004). Copyright © 2004 American Physical Society.

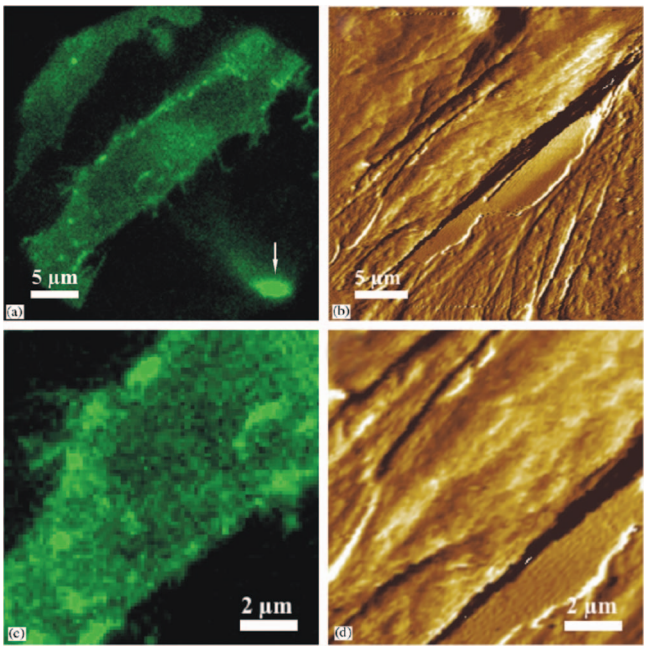

FIG. 24. (a), (b) Simultaneous (a) epi-fluorescence microscopy and (b) AFM imaging of live ldlA7-SRBI-eGFP CHO cells. (c) and (d) are magnified images of (a) and (b). Reprinted with permission from Madl *et al.*, Ultramicroscopy **106**, 645 (2006). Copyright © 2006 Elsevier.

decay rates of radiative and non-radiative processes. At short distances, the increase in excitation rate is overcome by the significant quantum yield decrease due to nonradiative processes, resulting in fluorescence quenching.[255,260]

The enhancement of the fluorescence signal in the area under the tip apex also produces images with a lateral resolution noticeably better than the diffraction limit.[203,255,262] Fluorescence images were collected from the same quantum dot with and without the tip. On the image collected without the tip, the fluorescence intensity profile exhibits a peak with a full width at half maximum (FWHM) of 200 nm. When the tip is approached to a distance of about 5 nm above the quantum dot, the fluorescence peak intensity is enhanced by a factor of four and its FWHM was reduced to 60 nm.[262] The resolution improvement allowed for the imaging of pairs of Cy-3 fluorophores separated by a distance of 13.0 ± 4.1 nm.[203]

To reduce the out-of-focus fluorescence background, total internal reflection fluorescence microscopy was combined with AFM. Total internal reflection occurs at the interface between two environments with different refractive indices *n*. When light travels in the high *n* environment and reaches the interface at an incident angle larger than the critical angle, it is reflected at the interface and an evanescent wave is generated in the low *n* environment. The intensity of the evanescent wave decays exponentially with the distance to the interface. The penetration depth of the evanescent wave is typically under 100 nm, providing high surface sensitivity and low out-of-focus fluorescence background. The surface sensitivity was useful in the study of focal adhesion in vascular smooth muscle cells.[263] The same approach was used to conduct localized surface plasmon resonance spectroscopy on arrays of silver nanostructures.[264]

Due to the small depth penetration of the evanescent wave, precise control of the objective vertical position with piezoscanners is necessary to adjust for thermal drift. The additional closed-loop piezoscanner can interfere with the operation of the AFM. In order to increase the mechanical stability of the AFM-inverted microscope assembly, the objective can be rigidly fixed on the same stage that supports the AFM. Such an assembly was used to collect high resolution force spectroscopy data on dye-labeled DNA strands for hours.[265]

Fluorescence lifetime imaging microscopy (FLIM) has numerous applications in biology, including differentiating cell components, cancer diagnosis, and drug release.[266] Correlated AFM topography and tip-enhanced fluorescence intensity and lifetime images were collected from dye-labeled nanoparticles and stained DNA.[267] Comparison of the fluorescence decay traces for a dye-labeled polystyrene nanoparticle with and without the tip above it revealed that the presence of the tip affects both the fluorescence intensity and lifetime. Without the tip, the decay time constant was measured at 6.4 ± 0.2 ns, while the decay time constant for the same particle with the tip was 2.8 ± 0.2 ns.[267] The interference from the tip complicates the interpretation of the lifetime measurements. The application of FLIM and AFM on stained DNA helped locate the fluorophore along the DNA molecule, with an enhanced spatial resolution that was inaccessible to the AFM or confocal fluorescence microscopy.[267]

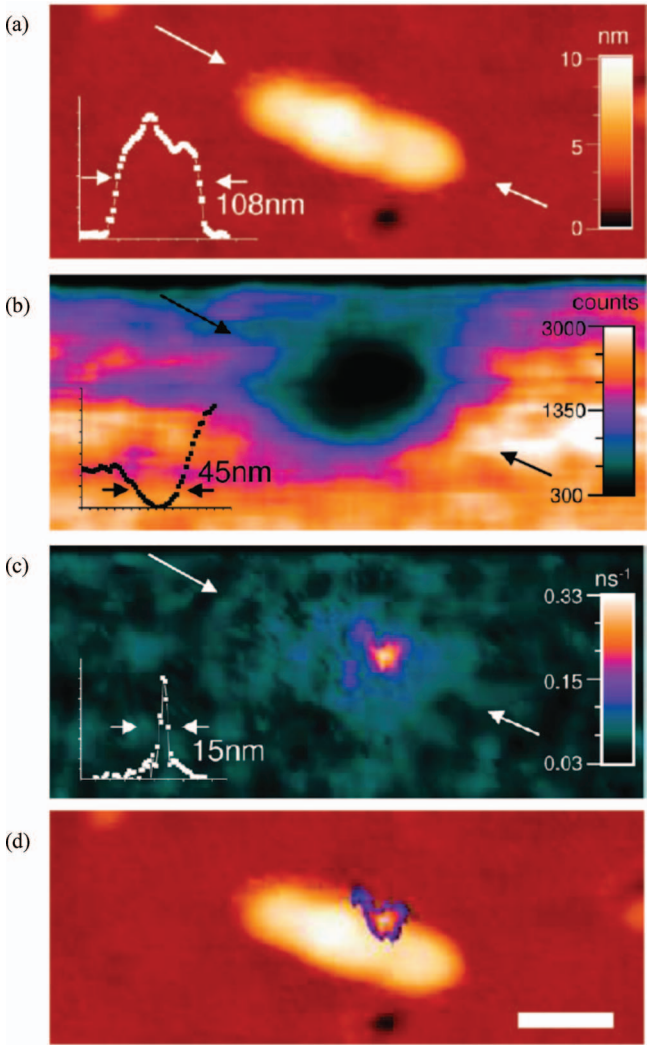

FIG. 25. (a) Topography image of a CdSe/CdS rod, with a 3.9 nm core and length of 108 nm (FWHM). The inset shows the cross section marked with arrows. (b), (c) Height-sectioned near-field fluorescence (b) intensity and (c) lifetime images of the same particle with cross sections of 45 and 15 nm (FWHM), respectively, taken along the topography cross section. (d) Overlay of the lifetime image with the topography image. The peak indicates the seed location along the rod. The scalebar is 50 nm. Reprinted with permission from Yoskovitz *et al.*, Nano Lett. **10**, 3068 (2010). Copyright © 2010 American Chemical Society.

Using a similar approach, the fluorescence intensity and lifetime were also collected for each lateral and vertical position of the tip with a lateral resolution better than 20 nm. The height sectioning was particularly useful in the study of heterostructured semiconductor nanorods, constituted of a CdSe seed embedded inside a CdS nanorod. The fluorescence quenching and longer lifetime at the seed location showed electron localization in the seed (Fig. 25).[268]

One-photon microscopy suffers from the photobleaching and blinking of the fluorophores. To alleviate the blinking problem, quantum dots have been used as fluorophores. The close proximity of the AFM tip within tens of nm of a quantum dot seemed to reduce the fluorescence blinking.[262] The development of tip-enhanced two-photon fluorescence offers less photobleaching, a much better spatial resolution and lower background noise.[181,269]

Control over the polarization of the excitation provides information on the orientation of individual fluorophores. The enhancement factor varies with the orientation of the molecules with respect to the enhanced electric field at the tip apex.[270] Molecules with various orientations produce different tip-enhanced fluorescence patterns that were successfully reproduced by a model that accounts for the dipole-dipole interactions between the tip and fluorophore.[255]

A polarization effect was also seen for two-photon fluorescence spectroscopy on a fluorescent dye. The fluorescence signal was found 2.4 times stronger when the incident polarization was along the tip axis than perpendicular to it.[149] Simultaneous noncontact AFM and fluorescence images showed a resolution of 43.8 nm on both images, much lower than the 800 nm excitation wavelength.[149]

B. Förster resonance energy transfer

FRET describes the energy transfer between two chromophores, such as fluorescent dyes, quantum dots, and other nanostructures. In the FRET mechanism, one of the chromophores, the donor, is first excited by an incident photon, followed by the energy transfer to the other chromophore, the acceptor, in close proximity. The excited acceptor then relaxes back to the ground state by emitting a photon. In order to occur, there must be a significant overlap between the emission spectrum of the donor and the absorption spectrum of the acceptor.[263]

The energy transfer and the fluorescence lifetime of the donor can be expressed as a function of the distance between the two chromophores using the Förster equations. By using these relations, the distance between the chromophores can be determined at the nanoscale by monitoring fluorescence intensity variations of either chromophore.[266]

FRET has been extensively used to study interactions between proteins and other biomolecules. The energy transfer and fluorescence lifetime of the donor are strongly dependent on the relative orientation of the chromophores. Such orientation dependence can potentially enable the study of protein folding and the environment effect on protein interactions.[266]

Scanning FRET microscopy was developed with a SNOM fiber probe[271] and with an apertureless AFM tip.[272] In the fiber probe approach, a small crystal containing the donor or the acceptor was placed at the apex of the fiber probe.[271] In the apertureless approach, the AFM tip was coated with donor or acceptor molecules.[272] When the FRET-activated fiber probe or AFM tip scanned the sample, the complementary donor/acceptor deposited on the sample generated a FRET signal if it was within the Förster radius.[263]

The combination of AFM and inverted microscope for FRET was used to image fibroblast cells expressing CFP-YFP construct. In order to capture simultaneously the images of the donor/acceptor emission and the FRET signal, a double-band dichroic mirror was installed in the inverted microscope. The donor emission was collected with one camera, while the acceptor emission and the FRET signal were collected with another camera.[263]

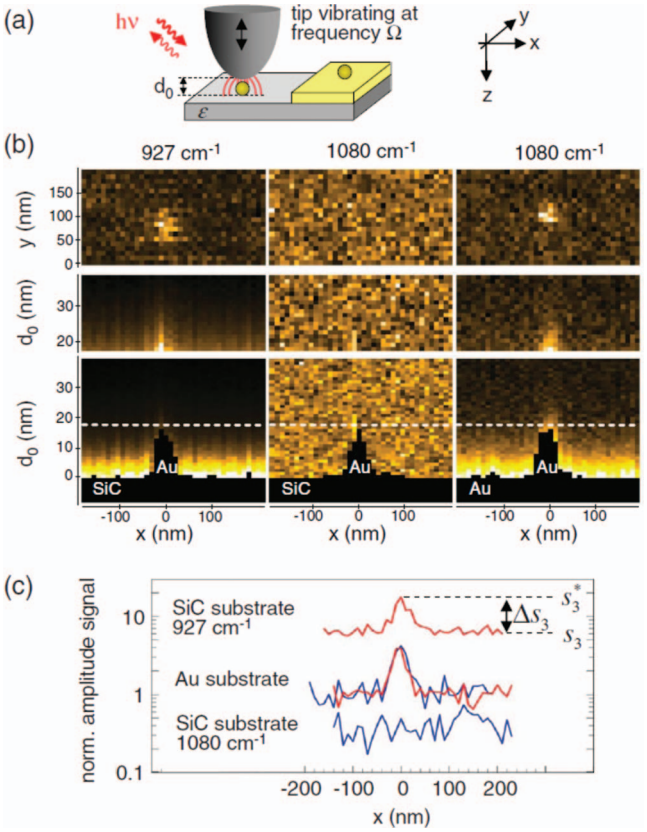

FIG. 26. Near-field infrared imaging of gold nanoparticles deposited on a SiC substrate. (a) Schematics of the experimental setup. (b) 3D optical amplitude images. Bottom row: Vertical slices of the optical signal amplitude as a function of the gap width d_0 and the horizontal particle position. Middle row: Top part of the vertical slices with enhanced contrast. Top row: Horizontal slices 1 nm above the particle (marked by dashed lines). (c) Normalized signal amplitudes of the 1080 cm^{-1} (blue) and 927 cm^{-1} (red) bands along the dashed lines in (b). Reprinted with permission from Cvitkovic *et al.*, Phys. Rev. Lett. **97**, 060801 (2006). Copyright © 2006 American Physical Society.

C. Infrared and optical absorption spectroscopy

Infrared spectroscopy is a vibrational spectroscopy technique that has been helpful in the characterization of chemical composition and monitoring chemical reactions. The excitation wavelength is typically a few micrometers, and therefore imaging with sub-micrometer spatial resolution is challenging due to the diffraction limit. The enhancement of the near-field infrared signal was made possible by the proximity of gold-coated tips, in a way similar to tip-enhanced Raman spectroscopy.[273,274] The lateral resolution of the infrared spectroscopy images was better than 30 nm when this apertureless method was applied to gold nanoparticles on silicon (Fig. 26).[273,274] When applied to a polystyrene/polymethylmethacrylate blend, the contrast between the two polymers was found to depend on the excitation wavelength. When the excitation matches the resonance of one of the polymers, the increased absorption makes the infrared image darker.[273]

Another method, called photothermal infrared microscopy, is based on the thermal expansion of the sample due to infrared absorption. The sample temperature variations are measured by a thermal probe that acts as a thermal couple[275]

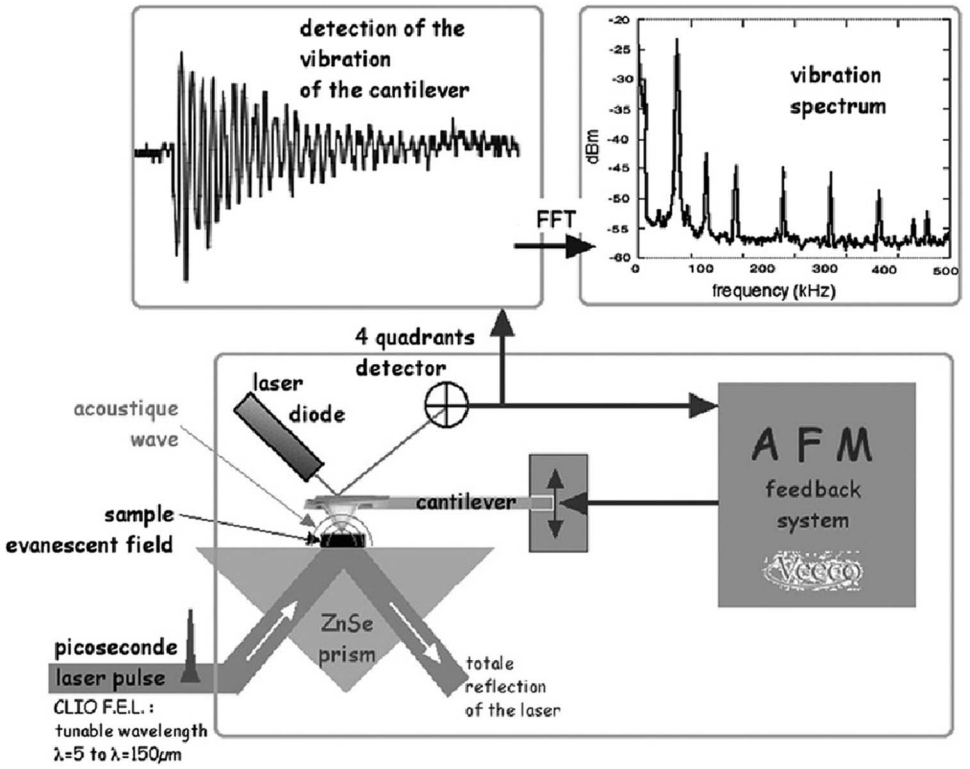

FIG. 27. Schematic of an AFM combined with infrared spectroscopy. The atomic force microscope tip probes the local deformation of the sample induced by a pulsed infrared laser tuned at a sample absorbing wavelength. Reprinted with permission from Dazzi *et al.*, Ultramicroscopy **107**, 1194 (2007). Copyright © 2007 Elsevier.

or by the deflection/deformation of an AFM cantilever (Fig. 27).[276,277] The near-field infrared absorption spectra from a single *E. coli* bacterium matched well with the far-field spectra from a collection of bacteria.[277]

To eliminate the background and increase the signal-to-noise ratio of the near-field signal, modulated techniques were usually used. The AFM tip operated in tapping mode at its resonance frequency.[273,274,276,278] The backscattered light can then be detected by a pseudoheterodyne interferometric method and then demodulated at the second harmonic of the tip oscillation frequency.[279]

In the studies mentioned above, the tip was in most cases illuminated from the side. For example, a Pt-coated AFM tip was illuminated with a CO_2 laser (wavelength 10.6 μm) and a Cassegrain objective (NA = 0.5) placed at an angle of 65° with the substrate normal direction. The scattered light was collected through the same optics.[278] But the sample can also be illuminated from below by total reflection of the incident light in a ZnS or ZnSe prism crystal.[277,280] A combination of AFM with infrared-attenuated total reflection spectroscopy (ATR-FTIR) was demonstrated for the study of surface modification in a liquid cell (Fig. 28).[280] Using the same illumination geometry, a scanning electrochemical microscope (SECM) was combined with ATR-FTIR.[43,44] ATR-FTIR spectroscopy relies on the generation of an evanescent field on the waveguide surface, so it is extremely surface-sensitive and reduces the interferences with strong absorbers and water. The ATR crystal was an integral part of an electrochemical cell. The microelectrode of the SECM, a Pt wire sheathed with an open borosilicate glass capillary, was positioned above the ATR crystal with stepper motors. The combined SECM-ATR-FTIR was used to induce the electropolymerization of 2,5- di-(2-thienyl)-pyrrole by applying a potential to the microelectrode against a reference, and monitor the same reaction *in situ* with a time-lapse series of IR absorption spectra.[44]

As for combinations of optical absorption spectroscopy and SPM, images of the optical absorption of individual carbon nanotubes were obtained with a sub-nanometer

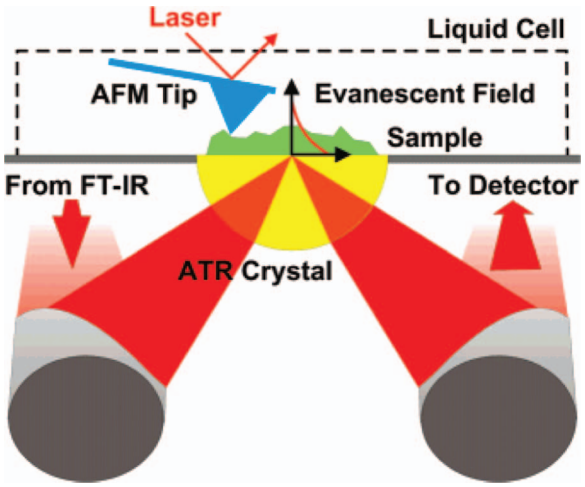

FIG. 28. Schematic of a combination of AFM with infrared attenuated total reflection spectroscopy. Reprinted with permission from Brucherseifer *et al.*, Anal. Chem. **79**, 8803 (2007). Copyright © 2007 American Chemical Society.

resolution using a combination of STM and illumination (total internal reflection) by a frequency- or amplitude-modulated laser. The STM tip measured variations of the tunneling current that were induced when the sample was in resonance. Using a lock-in amplifier, topography and optical absorption images were collected simultaneously. Carbon nanotubes with different chiralities could be differentiated and point defects were imaged.[281]

Molecular resonances in dye molecules were also successfully characterized by image force microscopy, where four laser lines at 475, 543, 594, and 633 nm were coupled to an inverted optical microscope. The incident laser illuminated the sample from the bottom and its intensity was modulated at a frequency of 360 kHz, while the AFM located above the sample operated in tapping mode at a frequency of 65 kHz. The deflection of the AFM cantilever was detected with a lock-in amplifier at the sum frequency of 425 kHz. The image of the signal from the lock-in amplifier showed a wavelength-dependent contrast for the 6-tamra dye that reaches a maximum at 543 nm. The variations of the lock-in intensity matched well with the absorption spectrum of bulk 6-tamra dye collected with a commercial absorption spectrometer. The contrast was explained by the modulation of the force gradient between the excited dipole in the sample and its mirror image in the platinum-coated tip.[282]

D. Second-harmonic generation

Second-harmonic generation (SHG) is a nonlinear scattering process, where the scattered photons have an energy that is twice the energy of the incident photons. The technique is extremely surface-sensitive and probes a smaller volume than in conventional fluorescence microscopy, therefore improving the spatial resolution and reducing the far-field background. According to the selection rules, SHG only occurs in a sample without inversion symmetry. However, most samples exhibit roughness and defects that relax the selection rules. Therefore, SHG is observed on most samples.[283]

Near-field SHG microscopy has attracted considerable interest, since the technique can be applied to a wide variety of samples, such as metallic films[283,284] and ferroelectric films.[285] The first experimental demonstrations were made with rough metallic surfaces.[283,284] A silver-coated[283] or uncoated fiber[284] was maintained at a short distance of the surface by a shear-force feedback mechanism. A silver-coated fiber resulted in a higher enhancement factor of the SHG signal, but introduced large perturbations of the electromagnetic field and the distribution of the SHG signal. The near-field SHG can be detected in two ways: depending of the nonlinear susceptibility of the fiber and sample, either the sample is illuminated from the far-field and the signal is collected locally with a fiber; or the fiber acts as a local light source and the SHG is collected in the far-field.[286,287]

Most studies involved an uncoated glass fiber that can still yield an enhancement due to the sharpness of the fiber apex.[284,288] SHG requires powerful excitations, since the signal is proportional to the fourth power of the local excitation power. It was estimated that in average only one second-harmonic photon count is generated for every 100 excitation pulses.[283] In order to reduce heating and sample damage, ultrafast pulsed lasers are usually used as excitation with side illumination.[283–285] The power density at the sample is typically 1.0 $MW.cm^{-2}$. The SHG signal was found to decrease significantly when the tip-sample distance is larger than 500 nm.[284] The surface sensitivity of this technique limits the fluorescence from the background. The presence of the tip keeps the near-field enhancement localized, and SHG images with a spatial resolution of 80 nm were reported.[285]

The deposition of nanoparticles or a thin metallic layer near the tip of the fiber can also enhance the SHG signal. Enhancement of the SHG signal from a styryl dye was reported after the deposition of a silver or gold nanoparticle at the tip of a glass cantilevered nanopipette.[234] In another study, a 30 nm-thick gold layer coated the silica AFM tip. The gold-coated tip, of diameter 70 nm, was reported to enhance the SHG signal from individual ZnO nanowire by a factor of 2000, after accounting for the far-field background signal.[289]

A strong polarization dependence was observed on the SHG signal.[283–286,289,290] Excitation with *p*-polarization resulted in a stronger near-field SHG signal.[283] With a *s*-polarized excitation, the contrast in the images was mainly due to the sample topography. With a *p*-polarized excitation, the interpretation of the image contrast is complicated by sharp features in a rough surface and the excitation of surface plasmon resonance.[284] Due to the polarization dependence, SHG was found to be sensitive to the crystal orientation in polycrystalline $Pb(Zr_xTi_{1-x})O_3$ films.[285]

VII. APPLICATIONS

A. Single molecule spectroscopy

Spectroscopy on ensembles of molecules only provides average properties of molecules that are isotropically oriented and in different environments. For molecules with a high molecular weight, such as polymers, proteins, and nanowires, the properties along the molecule may change due to different conformations, kinks, defects, crystallographic structure, and orientation. Single-molecule spectroscopy provides a more complete picture of the molecule properties.

Early work was on molecules with high Raman cross sections, such as carbon nanotubes. TERS images of isolated nanotubes were collected with high spatial resolution (Fig. 29).[130] The TERS experimental setup also allowed for the simultaneous collection of photoluminescence images.[291] G' band shifts along an individual nanotube revealed residual stress or defects along the sidewall of the nanotube.[130] TERS was even used for carbon nanotubes beneath an SiO_2 coating.[213] The presence of junctions and defects in carbon nanotubes was also observed.[206,292] Radial breathing modes position shifts along a single nanotube indicated modifications of the nanotube chirality. Topography changes and variations in the *G* band profile with the appearance of the Breit-Wigner-Fano feature in a nanotube section indicated the presence of a metal-semiconductor intramolecular junction.[292] Other nanostructures studied by TERS included multilayered graphene,[293] GaN nanowires,[294] and TiO_2 nanoparticles.[295]

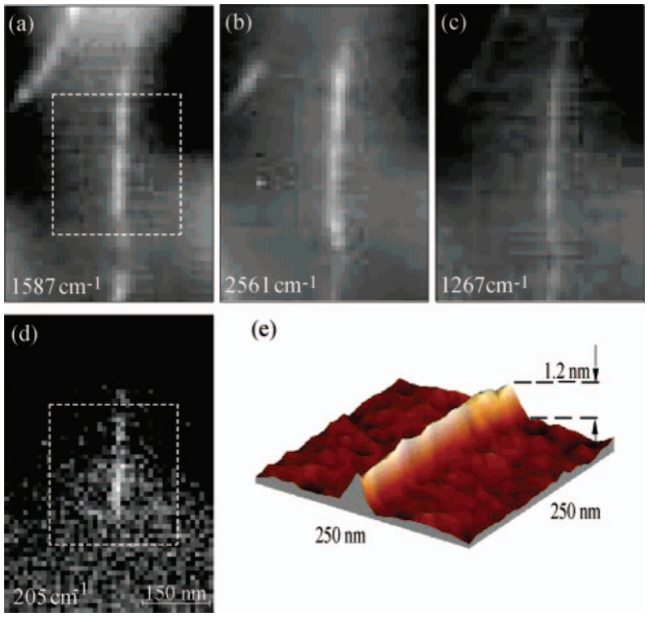

FIG. 29. TERS images of an individual carbon nanotube obtained by integrating the (a) *G* band, (b) *G′* band, (c) *D* band, and (d) radial breathing mode. (e) AFM topography image. Reprinted with permission from Anderson *et al.*, J. Am. Chem. Soc. **127**, 2533 (2005). Copyright © 2004 American Chemical Society.

TERS single-molecule sensitivity was extensively tested with Raman-sensitive dyes at low concentration, such as Rhodamine 6G, crystal violet,[171] malachite green isothiocyanate,[6,7] and cresyl blue.[8] In the case of malachite green isothiocyanate, the surface coverage was estimated to be less than 0.7 pmol/cm^2, which corresponds to a density of five molecules in the area under the tip. TERS on small nonresonant molecules included benzenethiol,[215] bipyridine,[228] cobalt tetraphenyl-porphyrin,[296] and CN^- ions[6] deposited on gold surfaces. In the case of cobalt tetraphenyl-porphyrin, the presence of additional bands corresponding to CO and NO stretch vibrations indicated the formation of complexes with axial ligands.[296]

TERS has proven to be a powerful tool to fingerprint biomolecules, such as amino acids, proteins, and DNA. Unlike fluorescence spectroscopy, TERS is a label-free method which requires little sample preparation. Using TERS, the aromatics amino acids phenylalanine and tryptophan were fingerprinted and the intensity of the benzene ring band provided information of the orientation of the molecules on the surface.[297] It was used to investigate portions of the heme protein cytochrome c. A few Raman bands were used as markers for the protein spin and oxidation state. Three types of TERS signatures were observed on cytochrome c and they were assigned to specific orientations of cytochrome c on the surface. Studying how proteins adsorb on surfaces, such as lipid membranes, may improve the sensitivity of chemical sensors.[160]

Work on DNA, RNA, DNA bases, and other pure DNA components, such as individual deoxynucleotides, was performed with TERS with the goal of determining the DNA sequence (Fig. 30).[185,230,298] TERS spectra were collected from the DNA bases adenine, thymine, guanine, and cytosine deposited on Au(111)[298] or a silver island film.[230] The main difference between the TERS signatures of DNA bases and

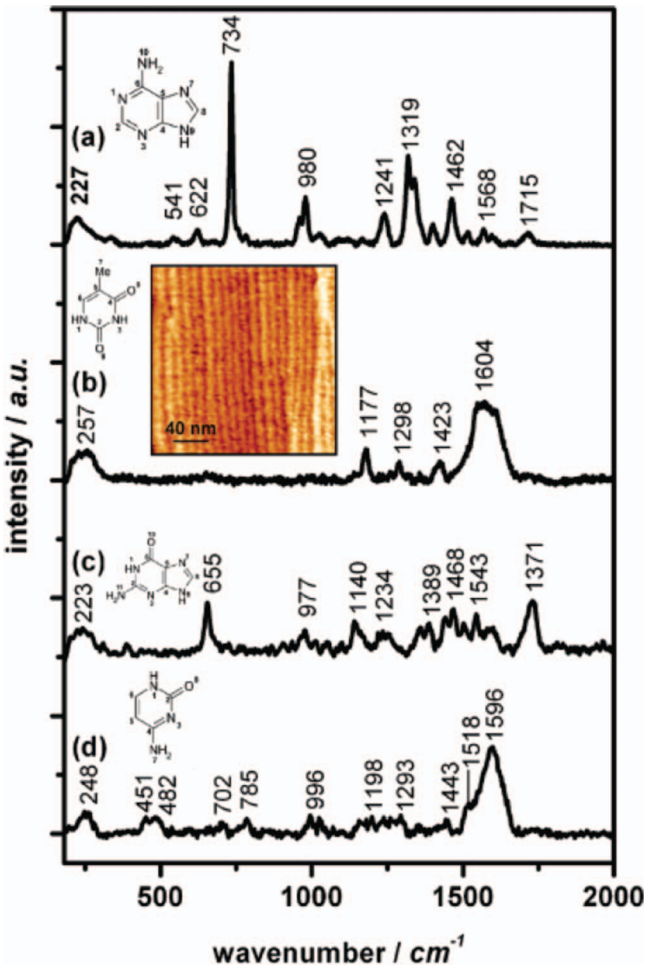

FIG. 30. Background-corrected TERS spectra of (a) adenine, (b) thymine, (c) guanine, and (d) cytosine deposited on Au(111). The inset is a STM image of a thymine self-assembled monolayer on Au(111). Reprinted with permission from Domke *et al.*, J. Am. Chem. Soc. **129**, 6708 (2007). Copyright © 2007 American Chemical Society.

deoxynucleotides was attributed to the phosphate group.[230] TERS spectra were also collected at different positions along a single-stranded RNA homopolymer of cytosine. Although small variations in band intensities and positions were observed, they were likely due to the instability of the tip-sample distance and not the RNA sequence.[185] Questions remain as to whether a single molecule is really observed or the signal is coming from a small cluster. Blinking is sometimes observed and can be explained by the movement of molecules, or their degradation from local heating. The sample can also desorb from the surface.[211]

B. Force measurements

The AFM tip can also be moved up and down vertically to collect a force curve as a function of the tip-sample distance. For AFM, the force sensitivity can vary by the selection of a cantilever with the appropriate spring constant. AFM has proven to be a powerful tool to measure the elastic modulus,[23,118,299] hardness[300,301] of materials, friction properties of nanostructures,[24,302] and to study the plastic deformation of nanostructures.[303]

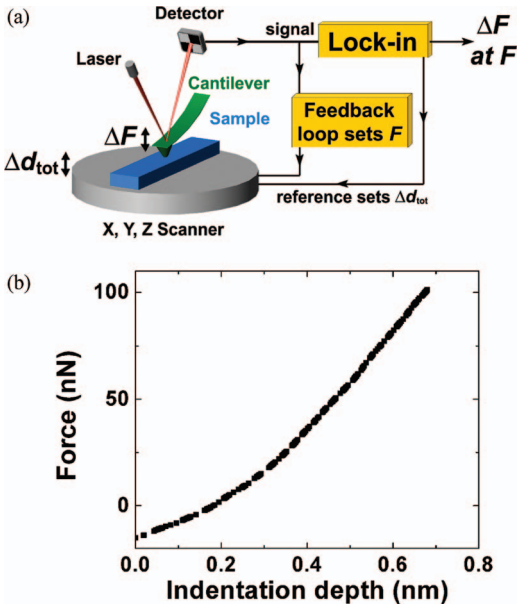

FIG. 31. (a) Experimental setup for the modulated nanoindentation method. (b) Normal force as a function of indentation depth for a ZnO nanobelt. Reprinted with permission from Lucas *et al.*, Nano Lett. **7**, 1314 (2007). Copyright © 2007 American Chemical Society.

To examine only the elastic deformation of nanostructures and limit the indent depth below 1 nm, a modulated nanoindentation technique was used, where an AFM tip indented the sample while the tip or the sample was oscillating in the normal direction with a piezoelectric scanner excited at a fixed amplitude and frequency.[23] The oscillations of the force exerted by the tip on the sample were then measured using a photodetector and a lock-in amplifier (Fig. 31).[118,119] The ratio between force oscillation amplitude ΔF and scanner movement Δz was measured for different values of normal forces F_0 to determine the derivative of the force-distance curve. The force-distance curve was obtained by integration and the elastic modulus was derived using Hertz theory:[299]

$$\frac{\partial F}{\partial z} = \left[\frac{1}{k_{cantilever}} + \frac{1}{2E^* \left[3/4 \; R \; (F + F_{adh}) / E^* \right]^{1/3}} \right]^{-1},$$

where $k_{\text{cantilever}}$ is the cantilever spring constant, R the tip radius, and F_{adh} the tip-sample adhesion force. E^* is the reduced modulus, a function of the elastic moduli E and Poisson's ratios ν of the tip and sample:

$$E^* = \left[\frac{1 - \nu_{tip}^2}{E_{tip}} + \frac{1 - \nu_{sample}^2}{E_{sample}} \right]^{-1}.$$

The elastic modulus of ZnO nanobelts was found to depend strongly on their width-to-thickness ratio, decreasing from about 100 GPa to 10 GPa, as the width-to-thickness ratio increases from 1.2 to 10.3.[118]

Another potential application in materials science is the study of polymer mechanical properties. The modulus of a polystyrene/polymethylmethacrylate blend was measured as a function of temperature around the glass transition of both polymers.[304] Such a study on polymers was complemented by Raman spectroscopy, which was used to characterize crystallinity[120] and crystallite orientation in polymers.[121]

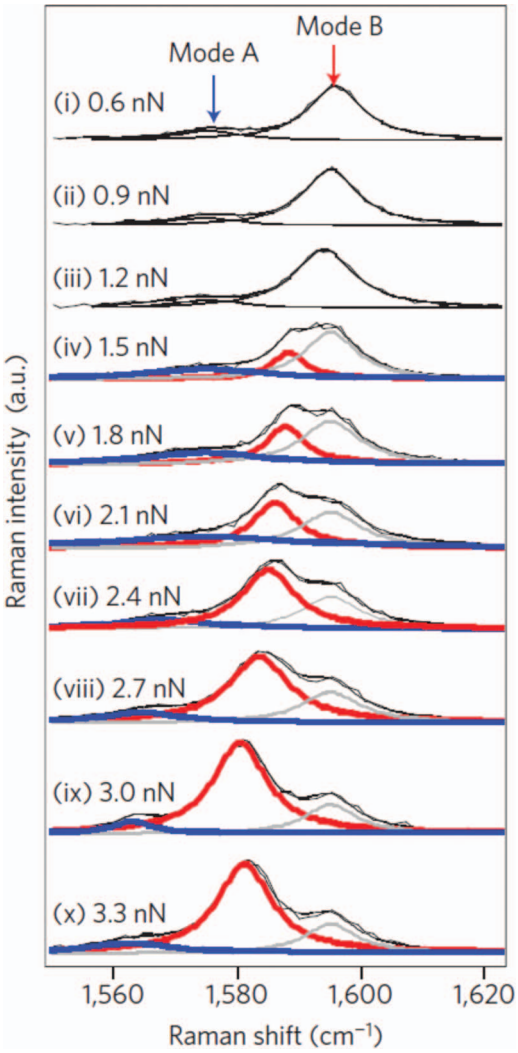

FIG. 32. TERS spectra of the G band of an individual single-wall carbon nanotube under the pressure applied by an AFM tip. Reprinted by permission from Yano *et al.*, Nat. Photonics **3**, 473 (2009). Copyright © 2009 Macmillan Publishers Ltd.

The tip can also be used as a probe to apply local stress on nanostructures, while TERS data are acquired. The radial breathing modes and G band of carbon nanotubes were found to shift in position as the tip applies an increasing pressure (Fig. 32).[10,208] A similar study on C_{60} molecule aggregates revealed irreversible intensity variations and shifts for the radial-breathing A_g mode at high stress that could be the signature of C_{60} polymerization.[93]

While the AFM offers high spatial and temporal resolution for cell studies, it can also measure physical properties, while their biological function are assessed by optical microscopy. AFM revealed with high resolution the morphology of whole cells and it changes as it reacts to chemical stimuli. AFM allows for the study of their locomotion: it can image the formation of membrane protrusions as the cells migrate on a surface.[305] Force measurements on whole cells by AFM were combined with confocal fluorescence microscopy. The force was applied by a glass bead attached to the end of a

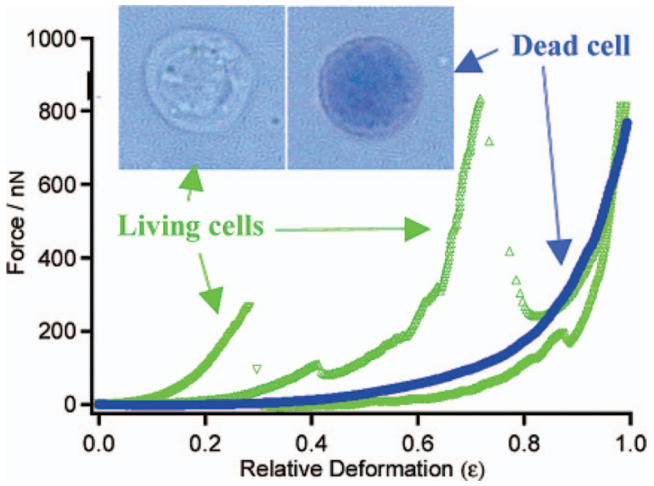

FIG. 33. Typical force versus deformation curves for living (green/light) and dead (blue/dark) T cells. Insets show the two types of cells upon the addition of 10 μL of 4% trypan blue solution. Dead cells turn blue under optical microscopy. Reprinted with permission from Lulevich *et al.*, Langmuir **22**, 8151 (2006). Copyright © 2006 American Chemical Society.

tipless cantilever. The force ranged from 10^{-11} to 10^{-5} N. Force-distance curves were acquired while the deformation of the cell nucleus and membrane was observed by using appropriate stains and fluorescence microscopy.[306] The mechanical data provided insight into the cell elasticity and permeability. For deformations below 30%, the cell response was elastic and the force-distance curve was reversible. It was suggested that the membrane remained impermeable. At large deformations above 30%, the force-distance curve exhibited force discontinuities that were attributed to partial membrane rupture and liquid leaking from the cell (Fig. 33). Mechanical characterization on cells can determine whether the cell is alive or dead. Dead cells were identified by fluorescence spectroscopy using the trypan blue stain. Force-distance curves from dead cells were continuous, even for large deformations. They were irreversible at strains as low as 10%–20%.[306]

Using the elastic theory of membranes and the Hertz theory on contact mechanics, an expression for the force F as a function of the normal strain ε applied to the cell was derived to extract the membrane and cytoskeleton elastic moduli of live cells:[306]

$$F = F_m + F_c = 2\pi \frac{E_m}{1-\nu_m} h R_0 \varepsilon^3 + \pi \frac{\sqrt{2}E_c}{3\left(1-\nu_c^2\right)} R_0^2 \varepsilon^{3/2},$$

where R_0 and h are the radius of the uncompressed cell and its plasma membrane thickness. E and ν are the elastic modulus and the Poisson's ratio. The indices m and c are for the membrane and cytoskeleton, respectively. From live T-cell force-distance curves, the membrane elastic modulus was determined to be between 10 and 35 MPa.

Other potential applications of force measurements in biology are the cell response to external chemical stimuli[307] and the study of interactions between single molecules.[308] Advances in force spectroscopy in air and liquids in tapping modes will further improve the force sensitivity and resolution, even on soft materials such as cell membranes and polymer films.[309] Advances in the development of AFM probes enabled the measurement of mechanical forces at high frequencies with acceptable signal-to-noise ratio.[27,304] The torsional harmonic cantilever, which has a tip that is slightly off the cantilever long axis, allows for the use of high frequency torsional resonances with high quality factor to measure and image the mechanical properties of soft polymer blends around their glass transition.[304]

For the mechanical measurements at high frequencies, the AFM operates in tapping mode, which reduces the sample damage.[305] The amplitude, frequency, and phase lag of the cantilever vibrations are the measurables, which provide information on the elastic and dissipative tip-sample interactions.[310] The extraction of quantitative data and their interpretation are complicated by the complex dynamic interactions between the sample and the tip, and the unknown tip shape. Algorithms are under development to derive quantities such as force as a function of distance, energy dissipated, elastic modulus, viscosity, and density.[310–312]

C. High-resolution chemical mapping

AFM and confocal Raman microscopy were combined to image the distribution of wood extractives on cellulose surfaces,[313] and the distribution of cellulose and lignin in wood.[314] AFM phase and Raman images were used to locate triglycerides, fatty acids, steryl esters, and resin acids on rough cellulose surfaces. These extractives cannot be distinguished from the substrate with AFM topography images.[313]

The high Raman cross section for some materials makes it possible to monitor chemical reactions. For example, AFM and Raman microscopy were used to monitor the modification of a NaCl(100) surface as it reacted with NO_2 at various relative humidity. Raman images confirmed the formation of $NaNO_3$ particles and AFM topography images allowed for the measurement of the size and density of the particles. AFM images showed that the particles aggregate at high relative humidity above 45% to form rhombohedral plates.[315] AFM and TERS were also used to map the chemical composition of a mixed polyisoprene and polystyrene film. Variations of TERS signals along line scans were attributed to the presence of air cavities in the film below the surface.[316]

Chemical force microscopy was made possible by the use of AFM tips functionalized with molecules that have an affinity with a specific analyte. The presence of the analyte is detected by an increase in adhesion force between the tip and the substrate. For example, a tip coated with CH_3-terminated alkanethiols was used to image the wettability of two types of live cells, *Aspergillus fumigatus* and *Mycobacterium bovis*. The presence of hydrophobic areas on the cell membrane revealed the presence of proteins which provided insight into the cell function.[317] Such an approach can be extended to a wide variety of biological ligands and receptors (for example, antigen-antibody) for molecular recognition (Fig. 34).[318]

Scanning near-field infrared spectroscopy was used to image polymer domains in a blend of polystyrene/polymethylmethacrylate based on the amplitude of the backscattered infrared signal.[319] The same technique was

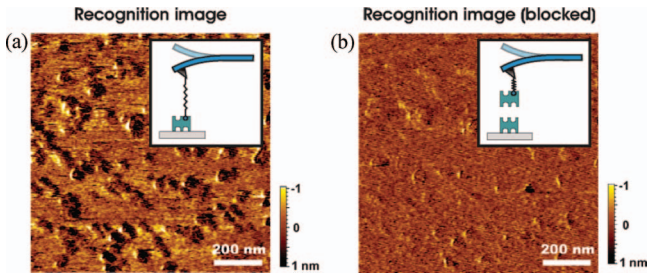

FIG. 34. (a) Recognition image of avidin molecules adsorbed to mica acquired with a biotin-tethered tip, prior to blocking. (b) Recognition image after blocking the tip by adding free avidin into the solution while scanning the same position. Reprinted with permission from Kienberger *et al.*, Acc. Chem. Res. **39**, 29 (2006). Copyright © 2006 American Chemical Society.

applied to the chemical fingerprinting of single tobacco mosaic virus (Fig. 35).[320]

Tip-enhanced CARS was applied to image adenine molecules in DNA clusters. The 1337 cm^{-1} CARS band, which corresponds to the ring-breathing mode of diazole in adenine, was integrated to image two DNA clusters separated by 160 nm.[252] Tip-enhanced CARS was also applied to the characterization of bacterial microcrystalline cellulose.[254]

D. Biology

Scanning probe microscopies have contributed to the advance of biotechnology, by enabling the study of structure-function relations, force spectroscopy on single-molecule or between molecules, biomolecule manipulation, and recognition.[321] The combination of AFM with fluorescence microscopy enabled the simultaneous high-resolution imaging of membrane components and dynamic processes in live cells. The AFM deflection images recorded in contact mode revealed topographic details on the cell content, such as the cytoskeleton and actin fibers. Fluorescence microscopy was used to image the membrane receptors labeled with the green fluorescent protein. Force spectroscopy on the imaged cells allowed for the characterization of the binding between antibodies attached to the tip and the receptors at the cell surface.[256]

AFM also imaged the appearance of ridges in cell membranes after activation with antigens. Topography images showed the height and distribution of these ridges on the cell surface and how they evolved as the cell spreaded. To understand the origin of these ridges, the F-actin network in the cytoskeleton was labeled with phalloidin. Overlaying the AFM and confocal fluorescence images from activated cells revealed that the location of the membrane ridges matched the F-actin network. The combination of the two techniques also showed the formation of depressions in the membrane that were correlated with the merger of granules into the membrane.[258]

TERS has provided spectroscopic fingerprints of lipids, proteins, and other polysaccharides.[12,313,322,323] When used in conjunction with AFM, the topography images and TERS spectra allowed for the characterization of cell structure and chemical composition of the cell membrane.[313,322] The interpretation of TERS spectra and the assignment of TERS bands are still complicated by the intensity variations due to molecule orientation, tip-sample distance, and tip shape variations.[12,323]

TERS in water was made possible by mounting the tip below a wide Teflon plate. A droplet of water fills the gap between the sample substrate and the Teflon plate, therefore keeping both the tip and the sample immersed during measurements. A tip coating consisting of SiO_x/Ag was selected to prevent detachment of the silver particles in water. As a demonstration, TERS spectra were collected from self-assembled monolayers of thiophenolate on gold surfaces immersed in water with enhancement factors larger than 10^4. Thus, TERS could potentially be applied to live cells in their physiological environment (Fig. 36).[216]

The scanning probe can also be used as part of a delivery system to inject chemical stimuli into live cells. Such a system was developed by attaching a functionalized multiwalled carbon nanotube to an AFM tip. As a demonstration, a quantum dot was attached to the nanotube by a linker which is composed of a disulfide bond and a pyrene moiety that adsorbs on the nanotube sidewall. Once the nanotube penetrates the cell membrane, the disulfide bond is cleaved in the reducing intracellular environment, releasing the quantum dot inside the cell. The release of the quantum dot was confirmed by fluorescence microscopy using an inverted microscope mounted

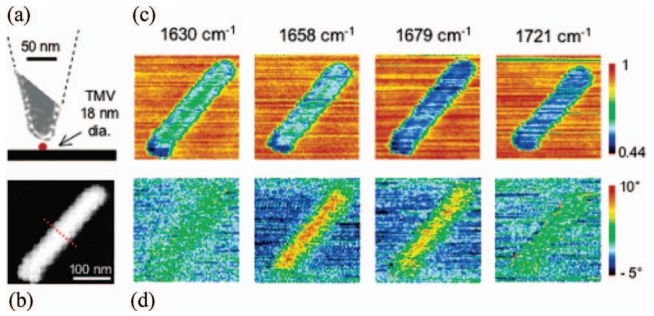

FIG. 35. Near-field infrared images of a single tobacco mosaic virus on Si. (a) Schematic and TEM image of the Pt-coated Si tip. (b) AFM topography image. (c) Near-field amplitude and (d) phase contrast images obtained by integrating different absorption bands. Reprinted with permission from Brehm *et al.*, Nano Lett. **6**, 1307 (2006). Copyright © 2006 American Chemical Society.

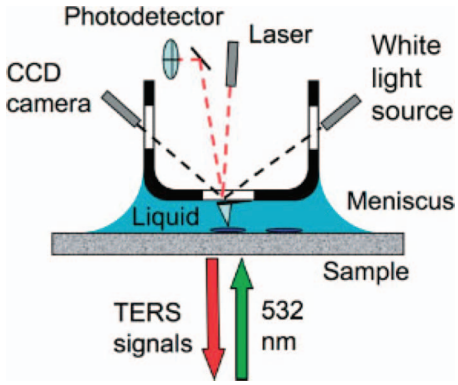

FIG. 36. Schematic diagram of the TERS setup in aqueous conditions. Reprinted with permission from Schmid *et al.*, J. Raman Spectrosc. **40**, 1392 (2009). Copyright © 2009 John Wiley.

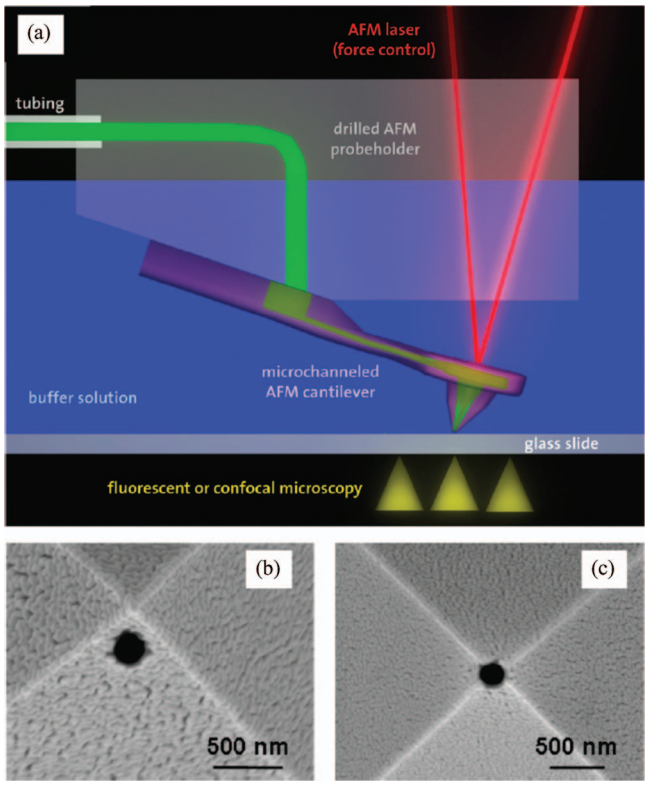

FIG. 37. (a) Schematic of fluidFM showing a microchanneled cantilever chip connected to an external liquid reservoir. (b), (c) SEM images of tip apices with apertures milled by focused ion beam. The aperture can be used to dispense chemicals inside live cells after a small perforation of the cell membrane. Reprinted with permission from Meister *et al.*, Nano Lett. **9**, 2501 (2009). Copyright © 2009 American Chemical Society.

under the AFM.[324] Such a delivery system required an incubation time of 15 to 30 minutes.

In order to reduce the delivery time and control the amount of cargo injected, a nanofluidic system was integrated into an AFM cantilever. The tip has an aperture and the cantilever is connected to an external reservoir and a pressure controller to form a fluidic circuit. The injection of fluorescein isocyanate sodium salt was monitored *in situ* by confocal scanning laser microscopy. This fluidFM technology can operate in liquids and can deliver larger amounts of any soluble biomolecules (Fig. 37).[325]

E. Defects

Defects and grain boundaries can affect negatively the elastic modulus of materials. However, in some cases, they have positive effects on the material strength. Silver nanowires produced by a chemical process have a pentagonal structure with five internal twin boundaries over their entire length. These twin boundaries pin dislocations in silver nanowires under tensile deformation, enhancing their strength while keeping their elastic modulus constant.[303]

Raman spectroscopy has been widely used to detect the presence of defects in materials. The Raman *D* band in carbon nanotubes was used to characterize the quality of synthesis products and the chemical functionalization of their sidewalls.[206] The same *D* band in graphene was used to assess the damage induced by ion beam irradiation. The combination of AFM and Raman spectroscopy showed at similar fluences single-layer graphene is more easily damaged by ion beams compared with multilayered graphene.[326] Another application of Raman spectroscopy is the characterization of amorphization and residual stresses in samples after indentation, which are revealed by the broadening and position shift of Raman bands.[327]

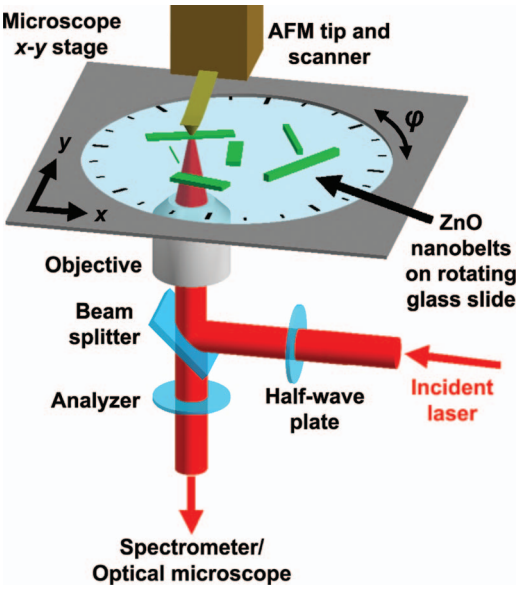

FIG. 38. Schematic of the experimental setup to characterize *in situ* the growth direction, defects, morphology, and mechanical properties of ZnO nanobelts. The samples are deposited on a glass slide, which is placed inside a rotating Petri dish. Reprinted with permission from Lucas *et al.*, Appl. Phys. Lett. **95**, 051904 (2009). Copyright © 2009 American Institute of Physics.

The presence of defects in ZnO nanobelts was characterized by the appearance of additional bands observed around 224 and 275 cm^{-1}.[119,123] Other Raman bands at 531, 631, and 720 cm^{-1} were previously observed in Sb-, Ga-, Mn-, and Fe-implanted ZnO films.[328] The combination of AFM and polarized Raman spectroscopy allowed for the characterization of morphology, defects, growth direction, and mechanical properties in ZnO nanobelts. As the nanobelt width-to-thickness ratio increased, the Raman defect peak areas were found to increase, leading to a significant decrease in the elastic modulus (Figs. 38 and 39).[119]

F. Crystallography

Raman spectroscopy has been widely used to characterize the crystal structure,[119] crystallinity,[120] and crystallite orientation[121] in materials. It was used to characterize residual indents in an indium antimonide single crystal. The appearance of new Raman bands around the residual indent suggested a phase transition from the zinc blende to wurtzite structure induced by the pressure applied during the indentation.[327] Relative intensity variations of the 380 and 1096 cm^{-1} bands in cellulose were measured to assess the crystallinity of samples after ball milling treatments of various times.[120]

TERS enabled the characterization of crystal structure with nanoscale spatial resolution. The integrated intensity

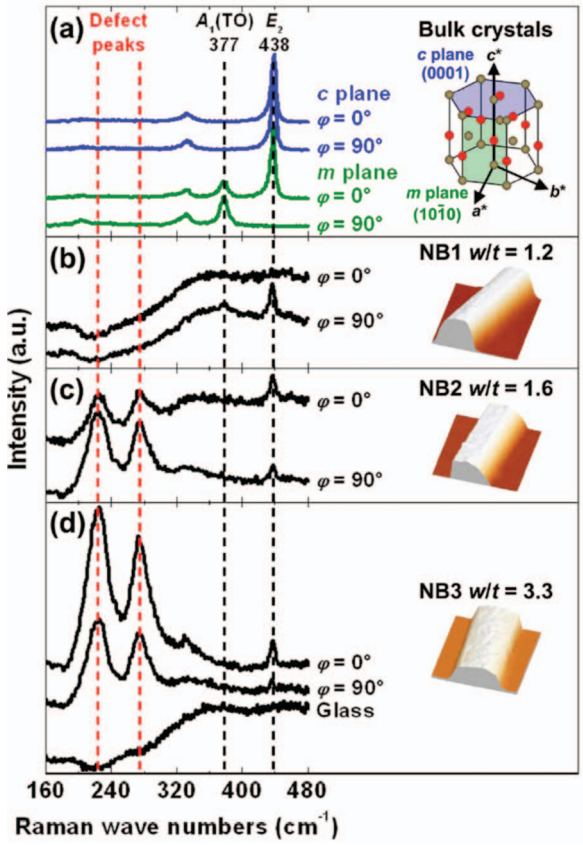

FIG. 39. (a) Polarized Raman spectra from the *c* and *m* planes of a ZnO crystal, shown in blue and green, respectively. The wurtzite structure (Zn atoms are brown, O atoms red) is also shown. (b)-(d) AFM topography images (3×3 μm^2) of three ZnO nanobelts labeled NB1, NB2, and NB3 and corresponding polarized Raman spectra. Reprinted with permission from Lucas *et al.*, Appl. Phys. Lett. **95**, 051904 (2009). Copyright © 2009 American Institute of Physics.

of the A_1 transverse optical mode at 516 cm^{-1} and the *E* longitudinal optical mode at 715 cm^{-1} was measured across $BaTiO_3$ nanorods to map ferroelectric domains. The domain boundaries in the TERS images were correlated with topographic changes in the AFM images (Fig. 40).[217]

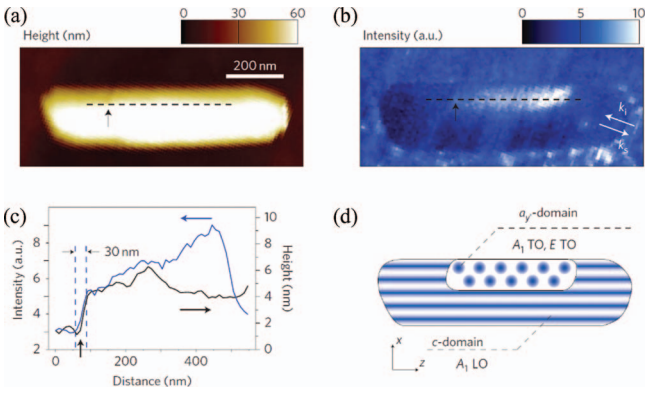

FIG. 40. Spatially resolved TERS for ferroelectric domain imaging. (a) Topography image of a $BaTiO_3$ nanorod. (b) Spectrally integrated TERS signal for ferroelectric domain imaging. (c) Line profiles along the dashed lines in (a) and (b) of TERS signal (blue) and topography (black). (d) Domain assignment based on the Raman selection rules for the TERS geometry used. Reprinted by permission from Berweger *et al.*, Nat. Nanotechnol. **4**, 496 (2009). Copyright © 2009 Macmillan Publishers Ltd.

A combination of polarized Raman spectroscopy and AFM can characterize the growth direction, the presence of defects, and the morphology of individual ZnO nanobelts. The nanobelt growth direction was determined by fitting polarized Raman spectroscopy data to group theory predictions (Fig. 41).[119,123] It was observed that nanobelts without defects had a width-to-thickness ratio that was correlated with the growth direction. Nanobelts with defects grew along a direction that formed an angle larger than 60° with the most common [0001] growth direction for all width-to-thickness ratio. These results revealed two different growth modes for ZnO nanobelts synthesized by physical vapor deposition without catalysts. In a first growth mode controlled by thermodynamics, nanobelts grow with the common growth habit without defects and their morphology depends on their growth direction. In a second growth mode controlled by kinetics, they grow along directions almost perpendicular to the common [0001] growth direction with defects.[123]

G. Strain mapping

Mechanical strain affects the position of many Raman bands in a variety of materials, including carbon nanotubes[56,57,329] and silicon.[330] The combination of Raman spectroscopy with AFM enables the manipulation of the sample and the controlled application of strain by the AFM tip while Raman spectra are simultaneously collected. For example, an AFM tip was used to apply uniaxial strain on an individual suspended carbon nanotube. An individual carbon nanotube was synthesized by chemical vapor deposition between the end of a silicon cantilever and the edge of a silicon substrate using a dilute ferritin solution as catalyst. Raman spectra were collected by focusing the laser spot on the nanotube section suspended over the gap. Strain was applied step-wise by pressing and deflecting the silicon cantilever with an AFM tip. This method eliminated any substrate effect on the nanotube deformation and Raman signal. Indeed, interactions between nanotube and substrate are known to shift the *G* band. The suspension of the nanotube not only reduced significantly the contribution of the substrate on the Raman signal, but also enhanced the nanotube signal.[329]

TERS was used to measure strain with high spatial resolution. Early TERS studies enabled the collection of AFM topographic images on an individual carbon nanotube of diameter 1.7 nm and TERS spectra at selected spots along the same nanotube. The TERS spectra revealed that the Raman *G′* band position varied along the nanotube with shifts as large as 9 cm^{-1}, which was partially explained by external stresses such as the interaction with the substrate (Fig. 42).[130] The *G′* band in carbon nanotubes shifted to higher or lower wave numbers, upon compressive or tensile stress along their axis, respectively.[57] Residual stresses were mapped with TERS in strained silicon structures as narrow as 70 nm.[214] However, the stress analysis is complicated by the laser heating of the sample and the temperature dependence of the Raman shift. In silicon, a temperature increase of 30 K in silicon can induce a shift of 0.6 cm^{-1} for the peak at 521 cm^{-1}. This shift is significant, considering that this peak

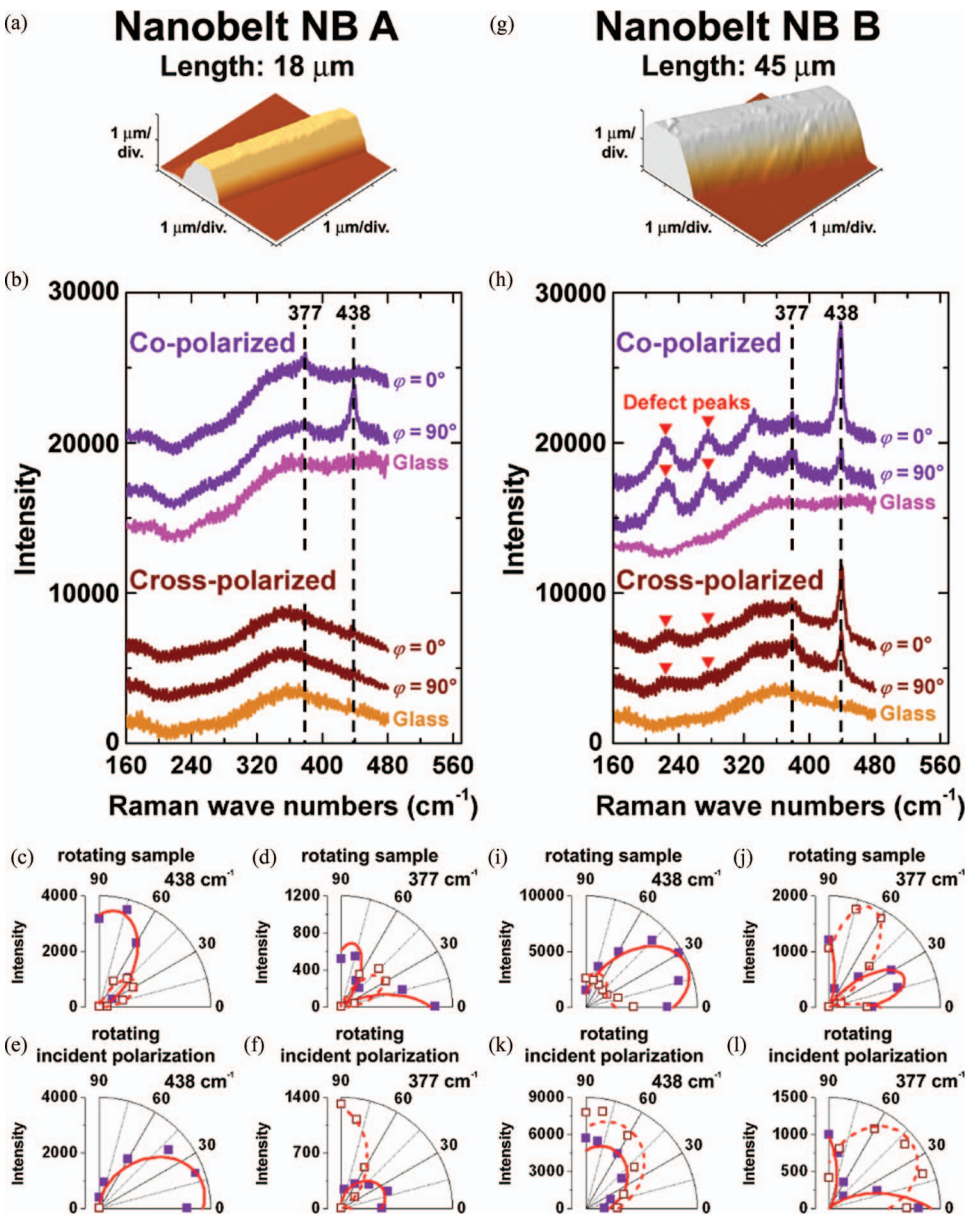

FIG. 41. Polarized Raman-AFM results on individual ZnO nanobelts. (a), (g) AFM topography images of two ZnO nanobelts. (b), (h) typical polarized Raman spectra for different sample orientations and polarization configurations. (c)-(f), (i)-(l) Polar plots of the angular dependence of the Raman intensities. The Raman spectra in (h) exhibit peaks centered at 224 and 275 cm^{-1} that are characteristic of defects in the nanobelt NB B. Reprinted with permission from Lucas *et al.*, Phys. Rev. B **81**, 045415 (2010). Copyright © 2010 American Physical Society.

shifts with stress at a rate of -4 cm^{-1}/GPa.[330] In order to measure accurately the stress in the material immediately under the tip and increase the signal-to-noise ratio, the far-field signal from unstrained silicon can be reduced by the appropriate selection of the polarization configuration.[224,225] Polarized TERS data collected using side illumination allowed for the determination of the full plane stress tensor for Si and $Si_{0.8}Ge_{0.2}$.[331]

The strong TERS signal from silicon allowed for the collection of AFM topography images and Raman strain maps (pixel size about 25 × 25 nm) in the same area on strained thin films. The near-field Raman strain map showed strain variations at the nanoscale, while the far-field strain map from the same area showed little contrast due to the averaging effect from the diffraction limit.[4]

H. Electrical properties

The various electrical modes developed in scanning probe microscopy enabled the imaging at the nanoscale of the work function, conductivity variations, and photocurrents in materials.[36] For example, conductive AFM was used to measure a conductivity enhancement in reduced graphene oxide nanoribbons produced by thermochemical nanolithography.[332]

Photocurrent AFM was used to map local photocurrents in organic photovoltaic devices manufactured on a transparent ITO electrode. The photocurrent AFM was placed on top of an inverted optical microscope that was used to illuminate the sample below the metallic AFM tip. Interfaces as narrow as 20 nm between donor/acceptor domains were imaged at 0 V bias. Spatial variations of the photocurrent were explained by

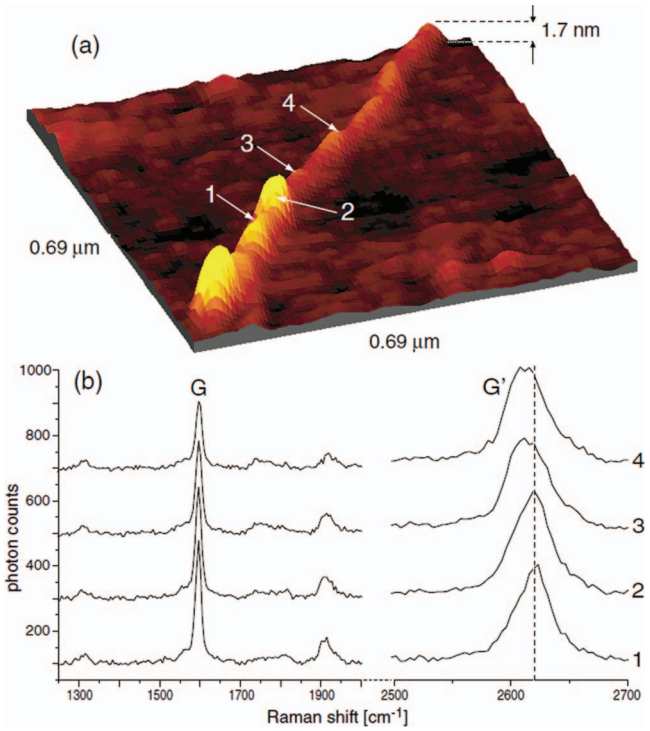

FIG. 42. (a) AFM topography image of an individual single-wall carbon nanotube. (b) TERS spectra at the positions 1 to 4 marked in (a). Reprinted with permission from Hartschuh *et al.*, Phys. Rev. Lett. **90**, 095503 (2003). Copyright © 2003 American Physical Society.

variations in morphology and microstructure of the polymer blend film (Fig. 43).[333]

Electrostatic force microscopy was used in combination with an inverted microscope to characterize photoinduced charging in a polymer blend film deposited on a transparent ITO electrode. The tip was set at a +10 V bias and oscillating at its resonance frequency above the sample surface. When the sample was excited by a monochromatic light at 405 nm, the charges generated led the resonance frequency to shift toward a new lower equilibrium value. The charging timescale was of the order of a few tens of microseconds, and depended on the sample material, excitation intensity, film thickness. A map of the charging timescale was generated with a resolution of about 100 nm and compared with topography images. The charging timescale at the interfaces between donor/acceptor domains was found 30%–50% slower than in the surrounding areas. Similar experiments on different polymer blends showed that the charging timescale correlated well with the quantum efficiency of the resulting photoconductive device. These results showed the complex interplay between local morphology, optoelectronic properties, and the resulting device performance.[39]

Scanning near-field infrared spectroscopy was applied to image the free-carriers concentration in sulfur-doped InP nanowires. The topography, amplitude, and phase of the backscattered light were measured simultaneously using a modulated technique. Amplitude and phase images of the infrared signal showed three different sections along a nanowire that cannot be distinguished by AFM topography. The highly doped central section exhibited a higher amplitude and phase than the surrounding undoped sections. Using the finite-

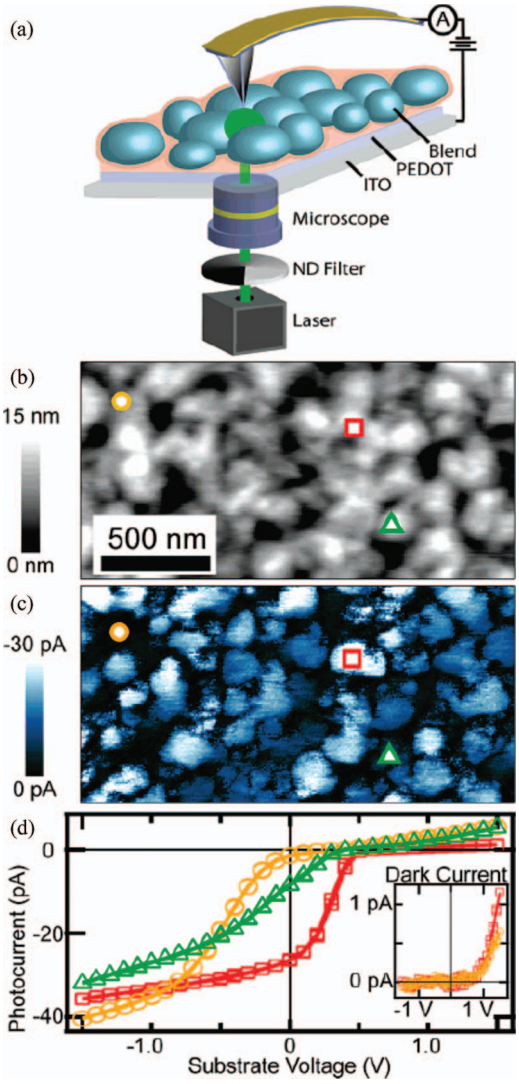

FIG. 43. (a) Schematic of photoconductive AFM. A laser illuminates a photovoltaic blend film through a transparent electrode and the current is collected with a metal-coated AFM tip. (b) AFM height image of an MDMO-PPV:PCBM 20:80 film spin-coated from xylenes. (c) Photocurrent map measured with zero external bias. (d) Local current-voltage data acquired at the three locations indicated in (b) and (c). Inset: Local current-voltage data without illumination showing much smaller dark currents. Reprinted with permission from Coffey *et al.*, Nano Lett. **7**, 738 (2007). Copyright © 2007 American Chemical Society.

dipole model, the amplitude and phase were correlated with the free-carrier concentration.[334] Scanning near-field infrared spectroscopy can also distinguish the metallic and the insulating phases of VO_2, based on their difference in optical conductivity. The metallic domains with a larger conductivity yielded a larger enhancement of the IR-s-SNOM signal. This technique was used to investigate the insulator-to-metal transition in VO_2 crystals at high temperatures, with a spatial resolution of 10–20 nm which was imposed by the tip radius.[278]

ACKNOWLEDGMENTS

We acknowledge the support of the Office of Basic Energy Sciences of the US Department of Energy (DE-FG02-06ER46293). We also acknowledge partial support from the

National Science Foundation (NSF) (CMMI-1100290 and DMR-0820382).

[1] A. M. Minor, J. W. Morris, and E. A. Stach, Appl. Phys. Lett. **79**, 1625 (2001).
[2] B. Varghese, Y. Zhang, L. Dai, V. B. C. Tan, C. T. Lim, and C.-H. Sow, Nano Lett. **8**, 3226 (2008).
[3] S. W. Hell, Science **316**, 1153 (2007).
[4] G. Binning, H. Rohrer, C. Gerber, and E. Weibel, Phys. Rev. Lett. **49**, 57 (1982).
[5] G. Binning, C. F. Quate, and C. Gerber, Phys. Rev. Lett. **56**, 930 (1986).
[6] B. Pettinger, B. Ren, G. Picardi, R. Schuster, and G. Ertl, Phys. Rev. Lett. **92**, 096101 (2004).
[7] K. F. Domke, D. Zhang, and B. Pettinger, J. Am. Chem. Soc. **128**, 14721 (2006).
[8] W. Zhang, B.-S. Yeo, T. Schmid, and R. Zenobi, J. Phys. Chem. C **111**, 1733 (2007).
[9] G. Picardi, Q. Nguyen, R. Ossikovski, and J. Schreiber, Appl. Spectrosc. **61**, 1301 (2007).
[10] T. Yano, Y. Inouye, and S. Kawata, Nano Lett. **6**, 1269 (2006).
[11] N. Hayazawa, M. Motohashi, Y. Saito, H. Ishitobi, A. Ono, T. Ichimura, P. Verma, and S. Kawata, J. Raman Spectrosc. **38**, 684 (2007).
[12] T. Schmid, A. Messmer, B.-S. Yeo, W. Zhang, and R. Zenobi, Anal. Bioanal. Chem. **391**, 1907 (2008).
[13] B. W. Hoogenboom, P. L. T. M. Frederix, J. L. Yang, S. Martin, Y. Pellmont, M. Steinacher, S. Zäch, E. Langenbach, H.-J. Heimbeck, A. Engel, and H. J. Hug, Appl. Phys. Lett. **86**, 074101 (2005).
[14] H. I. Rasool, P. R. Wilkinson, A. Z. Stieg, and J. K. Gimzewski, Rev. Sci. Instrum. **81**, 023703 (2010).
[15] K. Karrai and R. D. Grober, Appl. Phys. Lett. **66**, 1842 (1995).
[16] W. H. J. Rensen, N. F. van Hulst, and S. B. Kämmer, Appl. Phys. Lett. **77**, 1557 (2000).
[17] R. Toledo-Crow, P. C. Yang, Y. Chen, and M. Vaez-Iravani, Appl. Phys. Lett. **60**, 2957 (1992).
[18] T. R. Albrecht, P. Grütter, D. Horne, and D. Rugar, J. Appl. Phys. **69**, 668 (1991).
[19] T. Ichimura, S. Fujii, P. Verma, T. Yano, Y. Inouye, and S. Kawata, Phys. Rev. Lett. **102**, 186101 (2009).
[20] R. W. Stark and W. M. Heckl, Rev. Sci. Instrum. **74**, 5111 (2003).
[21] S. Hembacher, F. J. Giessibl, and J. Mannhart, Science **305**, 380 (2004).
[22] J. Preiner, J. Tang, V. Pastushenko, and P. Hinterdorfer, Phys. Rev. Lett. **99**, 046102 (2007).
[23] I. Palaci, S. Fedrigo, H. Brune, C. Klinke, M. Chen, and E. Riedo, Phys. Rev. Lett. **94**, 175502 (2005).
[24] M. Lucas, X. Zhang, I. Palaci, C. Klinke, E. Tosatti, and E. Riedo, Nat. Mater. **8**, 876 (2009).
[25] N. A. Burnham, O. P. Behrend, F. Oulevey, G. Gremaud, P.-J. Gallo, D. Gourdon, E. Dupas, A. J. Kulik, H. M. Pollock, and G. A. D. Briggs, Nanotechnology **8**, 67 (1997).
[26] S. N. Magonov, V. Elings, and M.-H. Whangbo, Surf. Sci. **375**, L385 (1997).
[27] L. Tetard, A. Passian, and T. Thundat, Nat. Nanotechnol. **5**, 105 (2010).
[28] Y. Sugimoto, P. Pou, M. Abe, P. Jelinek, R. Pérez, S. Morita, and Ó. Custance, Nature (London) **446**, 64 (2007).
[29] B. J. Albers, T. C. Schwendemann, M. Z. Baykara, N. Pilet, M. Liebmann, E. I. Altman, and U. D. Schwarz, Nat. Nanotechnol. **4**, 307 (2009).
[30] Y. Martin and H. K. Wickramasinghe, Appl. Phys. Lett. **50**, 1455 (1987).
[31] M. R. Koblischka and U. Hartmann, Ultramicroscopy **97**, 103 (2003).
[32] O. Züger and D. Rugar, Appl. Phys. Lett. **63**, 2496 (1993).
[33] C. L. Degen, M. Poggio, H. J. Mamin, C. T. Rettner, and D. Rugar, Proc. Natl. Acad. Sci. U. S. A. **106**, 1313 (2009).
[34] A. Majumdar, J. P. Carrejo, and J. Lai, Appl. Phys. Lett. **62**, 2501 (1993).
[35] R. Meckenstock, Rev. Sci. Instrum. **79**, 041101 (2008).
[36] R. Berger, H.-J. Butt, M. B. Retschke, and S. A. L. Weber, Macromol. Rapid Commun. **30**, 1167 (2009).
[37] A. J. Bard, F. R. F. Fan, J. Kwak, and O. Lev, Anal. Chem. **61**, 132 (1989).
[38] Y. Martin, D. W. Abraham, and H. K. Wickramasinghe, Appl. Phys. Lett. **52**, 1103 (1988).
[39] D. C. Coffey and D. S. Ginger, Nat. Mater. **5**, 735 (2006).
[40] M. Nonnenmacher, M. P. O'Boyle, and H. K. Wickramasinghe, Appl. Phys. Lett. **58**, 2921 (1991).
[41] Y. Cho, A. Kitahara, and T. Saeki, Rev. Sci. Instrum. **67**, 2297 (1996).
[42] V. Nalladega, S. Sathish, K. V. Jata, and M. P. Blodgett, Rev. Sci. Instrum. **79**, 073705 (2008).
[43] L. Wang, C. Kranz, and B. Mizaikoff, Anal. Chem. **82**, 3132 (2010).
[44] L. Wang, J. Kowalik, B. Mizaikoff, and C. Kranz, Anal. Chem. **82**, 3139 (2010).
[45] L. Gross, Nat. Chem. **3**, 273 (2011).
[46] S. H. Pan, E. W. Hudson, and J. C. Davis, Appl. Phys. Lett. **73**, 2992 (1998).
[47] A. Downes and M. E. Welland, Phys. Rev. Lett. **81**, 1857 (1998).
[48] C. Weiss, C. Wagner, C. Kleimann, M. Rohlfing, F. S. Tautz, and R. Temirov, Phys. Rev. Lett. **105**, 086103 (2010).
[49] C. Weiss, C. Wagner, R. Temirov, and F. S. Tautz, J. Am. Chem. Soc. **132**, 11864 (2010).
[50] B. J. Rodriguez, S. Jesse, A. P. Baddorf, and S. V. Kalinin, Phys. Rev. Lett. **96**, 237602 (2006).
[51] E. Bussmann and C. C. Williams, Rev. Sci. Instrum. **75**, 422 (2004).
[52] C. V. Raman and R. S. Krishnan, Nature (London) **121**, 501 (1928).
[53] R. L. McCreery, *Raman Spectroscopy for Chemical Analysis*, Chemical Analysis Vol. 157 (Wiley Interscience, New York, 2000).
[54] A. V. Malkovskiy, V. I. Malkovsky, A. M. Kisliuk, C. A. Barrios, M. D. Foster, and A. P. Sokolov, J. Raman Spectrosc. **40**, 1349 (2009).
[55] S. B. Cronin, A. K. Swan, M. S. Ünlü, B. B. Goldberg, M. S. Dresselhaus, and M. Tinkham, Phys. Rev. Lett. **93**, 167401 (2004).
[56] M. Lucas and R. J. Young, Compos. Sci. Technol. **67**, 2135 (2007).
[57] M. Lucas and R. J. Young, Phys. Rev. B **69**, 085405 (2004).
[58] A. Ianoul, T. Coleman, and S. A. Asher, Anal. Chem. **74**, 1458 (2002).
[59] M. Lucas, B. A. Macdonald, G. L. Wagner, S. A. Joyce, and K. D. Rector, A C S Appl. Mater. Interfaces **2**, 2198 (2010).
[60] C. Eliasson and P. Matousek, Anal. Chem. **79**, 1696 (2007).
[61] N. Welter, U. Schüssler, and W. Kiefer, J. Raman Spectrosc. **38**, 113 (2007).
[62] D. L. Dickensheets, D. D. Wynn-Williams, H. G. M. Edwards, C. Schoen, C. Crowder, and E. M. Newton, J. Raman Spectrosc. **31**, 633 (2000).
[63] J.-X. Cheng and X. S. Xie, J. Phys. Chem. B **108**, 827 (2004).
[64] M. D. Duncan, J. Reintjes, and T. J. Manuccia, Opt. Lett. **7**, 350 (1982).
[65] A. Zumbusch, G. R. Holtom, and X. S. Xie, Phys. Rev. Lett. **82**, 4142 (1999).
[66] T. Seeger, J. Jonuscheit, M. Schenk, and A. Leipertz, J. Mol. Struct. **661-662**, 515 (2003).
[67] G. Beadie, M. Bashkansky, J. Reintjes, and M. O. Scully, J. Mod. Opt. **51**, 2627 (2004).
[68] T. Ichimura, N. Hayazawa, M. Hashimoto, Y. Inouye, and S. Kawata, Phys. Rev. Lett. **92**, 220801 (2004).
[69] R. D. Schaller, J. Ziegelbauer, L. F. Lee, L. H. Haber, and R. J. Saykally, J. Phys. Chem. B **106**, 8489 (2002).
[70] C. L. Evans, E. O. Potma, M. Puoris'haag, D. Côté, C. P. Lin, and X. S. Xie, Proc. Natl. Acad. Sci. U. S. A. **102**, 16807 (2005).
[71] S.-H. Lim, A. G. Caster, O. Nicolet, and S. R. Leone, J. Phys. Chem. B **110**, 5196 (2006).
[72] B.-C. Chen, J. Sung, and S.-H. Lim, J. Phys. Chem. B **114**, 16871 (2010).
[73] F. Ganikhanov, C. L. Evans, B. G. Saar, and X. S. Xie, Opt. Lett. **31**, 1872 (2006).
[74] B. G. Saar, G. R. Holtom, C. W. Freudiger, C. Ackermann, W. Hill, and X. S. Xie, Opt. Express **17**, 12532 (2009).
[75] M. Fleischmann, P. J. Hendra, A. J. McQuillan, R. L. Paul, and E. S. Reid, J. Raman Spectrosc. **4**, 269 (1976).
[76] A. J. McQuillan, P. J. Hendra, and M. Fleischmann, J. Electroanal. Chem. **65**, 933 (1975).
[77] M. G. Albrecht and J. A. Creighton, J. Am. Chem. Soc. **99**, 5215 (1977).
[78] D. L. Jeanmaire and R. P. Van Duyne, J. Electroanal. Chem. **84**, 1 (1977).
[79] J. A. Creighton, C. G. Blatchford, and M. G. Albrecht, J. Chem. Soc., Faraday Trans. 2 **75**, 790 (1979).
[80] E. C. Le Ru, E. Blackie, M. Meyer, and P. G. Etchegoin, J. Phys. Chem. C **111**, 13794 (2007).
[81] P. G. Cao, J. L. Yao, B. Ren, B. W. Mao, R. A. Gu, and Z. Q. Tian, Chem. Phys. Lett. **316**, 1 (2000).
[82] P. Kambhampati, O.-K. Song, and A. Campion, Phys. Stat. Sol. (a) **175**, 233 (1999).
[83] J. R. Lombardi and R. L. Birke, Acc. Chem. Res. **42**, 734 (2009).
[84] A. Wokaun, J. P. Gordon, and P. F. Liao, Phys. Rev. Lett. **48**, 957 (1982).
[85] P. W. Barber, R. K. Chang, and H. Massoudi, Phys. Rev. Lett. **50**, 997 (1983).
[86] O. Sqalli, I. Utke, P. Hoffmann, and F. Marquis-Weible, J. Appl. Phys. **92**, 1078 (2002).

[87]B. N. J. Persson, K. Zhao, and Z. Zhang, Phys. Rev. Lett. **96**, 207401 (2006).
[88]C. L. Haynes and R. P. Van Duyne, J. Phys. Chem. B **107**, 7426 (2003).
[89]J. R. Lombardi, R. L. Birke, T. Lu, and J. Xu, J. Chem. Phys. **84**, 4174 (1986).
[90]A. Otto, A. Bruckbauer, and Y. X. Chen, J. Mol. Struct. **661-662**, 501 (2003).
[91]R. M. Stöckle, Y. D. Suh, V. Deckert, and R. Zenobi, Chem. Phys. Lett. **318**, 131 (2000).
[92]H. Watanabe, Y. Ishida, N. Hayazawa, Y. Inouye, and S. Kawata, Phys. Rev. B **69**, 155418 (2004).
[93]P. Verma, K. Yamada, H. Watanabe, Y. Inouye, and S. Kawata, Phys. Rev. B **73**, 045416 (2006).
[94]K.-I. Yoshida, T. Itoh, H. Tamaru, V. Biju, M. Ishikawa, and Y. Ozaki, Phys. Rev. B **81**, 115406 (2010).
[95]A. M. Schwartzberg, C. D. Grant, A. Wolcott, C. E. Talley, T. R. Huser, R. Bogomolni, and J. Z. Zhang, J. Phys. Chem. B **108**, 19191 (2004).
[96]P. Olk, J. Renger, T. Härtling, M. T. Wenzel, and L. M. Eng, Nano Lett. **7**, 1736 (2007).
[97]L. Rogobete, F. Kaminski, M. Agio, and V. Sandoghdar, Opt. Lett. **32**, 1623 (2007).
[98]R. M. Bakker, H.-K. Yuan, Z. Liu, V. P. Drachev, A. V. Kildishev, and V. M. Shalaev, R. H. Pedersen, S. Gresillon, and A. Boltasseva, Appl. Phys. Lett. **92**, 043101 (2008).
[99]J. Wessel, J. Opt. Soc. Am. B **2**, 1538 (1985).
[100]S. Nie and S. R. Emory, Science **275**, 1102 (1997).
[101]S. R. Emory and S. Nie, Anal. Chem. **69**, 2631 (1997).
[102]I. Khan, D. Cunningham, D. Graham, D. W. McComb, and W. E. Smith, J. Phys. Chem. B **109**, 3454 (2005).
[103]S. Basu, S. Pande, S. Jana, S. Bolisetty, and T. Pal, Langmuir **24**, 5562 (2008).
[104]X. Y. Lang, P. F. Guan, L. Zhang, T. Fujita, and M. W. Chen, J. Phys. Chem. C **113**, 10956 (2009).
[105]C. Y. Chan, J. B. Xu, M. Y. Waye, and H. C. Ong, Appl. Phys. Lett. **96**, 033104 (2010).
[106]W. Zhang, H. Fischer, T. Schmid, R. Zenobi, and O. J. F. Martin, J. Phys. Chem. C **113**, 14672 (2009).
[107]C. Tabor, D. Van Haute, and M. A. El-Sayed, ACS Nano **3**, 3670 (2009).
[108]X. Deng, G. B. Braun, S. Liu, P. F. Sciortino, Jr., B. Koefer, T. Tombler, and M. Moskovits, Nano Lett. **10**, 1780 (2010).
[109]J. J. Mock, M. Barbic, D. R. Smith, D. A. Schultz, and S. Schultz, J. Chem. Phys. **116**, 6755 (2002).
[110]M. Rycenga, P. H. C. Camargo, W. Li, C. H. Moran, and Y. Xia, J. Phys. Chem. Lett. **1**, 696 (2010).
[111]A. Tcherniak, J. W. Ha, S. Dominguez-Medina, L. S. Slaughter, and S. Link, Nano Lett. **10**, 1398 (2010).
[112]P. N. Njoki, I-I. S. Lim, D. Mott, H.-Y. Park, B. Khan, S. Mishra, R. Sujakumar, J. Luo, and C.-J. Zhong, J. Phys. Chem. C **111**, 14664 (2007).
[113]J. B. Lassiter, J. Aizpurua, L. I. Hernandez, D. W. Brandl, I. Romero, S. Lal, J. H. Hafner, P. Nordlander, and N. J. Halas, Nano Lett. **8**, 1212 (2008).
[114]H. Guo, F. Ruan, L. Lu, J. Hu, J. Pan, Z. Yang, and B. Ren, J. Phys. Chem. C **113**, 10459 (2009).
[115]L. V. Brown, H. Sobhani, J. B. Lassiter, P. Nordlander, and N. J. Halas, ACS Nano **4**, 819 (2010).
[116]T. Kalkbrenner, U. Håkanson, and V. Sandoghdar, Nano Lett. **4**, 2309 (2004).
[117]D.-K. Lim, K.-S. Jeon, H. M. Kim, J.-M. Nam, and Y. D. Suh, Nat. Mater. **9**, 60 (2010).
[118]M. Lucas, W. J. Mai, R. S. Yang, Z. L. Wang, and E. Riedo, Nano Lett. **7**, 1314 (2007).
[119]M. Lucas, Z. L. Wang, and E. Riedo, Appl. Phys. Lett. **95**, 051904 (2009).
[120]U. P. Agarwal, R. S. Reiner, and S. A. Ralph, Cellulose **17**, 721 (2010).
[121]M. Tanaka and R. J. Young, Biomacromolecules **7**, 2575 (2006).
[122]I. Calizo, A. A. Balandin, W. Bao, F. Miao, and C. N. Lau, Nano Lett. **7**, 2645 (2007).
[123]M. Lucas, Z. L. Wang, and E. Riedo, Phys. Rev. B **81**, 045415 (2010).
[124]V. Biju, D. Pan, Y. A. Gorby, J. Fredrickson, J. McLean, D. Saffarini, and H. P. Lu, Langmuir **23**, 1333 (2007).
[125]H. Ko, Y. Pikus, C. Jiang, A. Jauss, O. Hollricher, and V. V. Tsukruk, Appl. Phys. Lett. **85**, 2598 (2004).
[126]H.-J. Kim, D.-C. Kim, R. Kim, J. Kim, D.-H. Park, H.-S. Kim, J. Joo, and Y. D. Suh, J. Appl. Phys. **101**, 053514 (2007).
[127]U. Schmidt, S. Hild, W. Ibach, and O. Hollricher, Macromol. Symp. **230**, 133 (2005).
[128]W. X. Sun and Z. X. Shen, Ultramicroscopy **94**, 237 (2003).
[129]M. S. Anderson and W. T. Pike, Rev. Sci. Instrum. **73**, 1198 (2002).
[130]A. Hartschuh, E. J. Sánchez, X. S. Xie, and L. Novotny, Phys. Rev. Lett. **90**, 095503 (2003).
[131]L. Novotny, E. J. Sánchez, and X. S. Xie, Ultramicroscopy **71**, 21 (1998).
[132]S. Quabis, R. Dorn, M. Eberler, O. Glöckl, and G. Leuchs, Opt. Commun. **179**, 1 (2000).
[133]M. Sackrow, C. Stanciu, M. A. Lieb, and A. J. Meixner, Chem. Phys. Chem. **9**, 316 (2008).
[134]M. A. Lieb and A. J. Meixner, Opt. Express **8**, 458 (2001).
[135]P. Anger, A. Feltz, T. Berghaus, and A. J. Meixner, J. Microsc. **209**, 162 (2003).
[136]J. Steidtner and B. Pettinger, Rev. Sci. Instrum. **78**, 103104 (2007).
[137]C. Stanciu, M. Sackrow, and A. J. Meixner, J. Microsc. **229**, 247 (2008).
[138]D. Zhang, X. Wang, K. Braun, H.-J. Egelhaaf, M. Fleischer, L. Hennemann, H. Hintz, C. Stanciu, C. J. Brabec, D. P. Kern, and A. J. Meixner, J. Raman Spectrosc. **40**, 1371 (2009).
[139]D. Roy, J. Wang and M. E. Welland, Faraday Discuss. **132**, 215 (2006).
[140]C. C. Neacsu, J. Dreyer, N. Behr, and M. B. Raschke, Phys. Rev. B **73**, 193406 (2006).
[141]S. Berweger and M. B. Raschke, Anal. Bioanal. Chem. **396**, 115 (2010).
[142]D. Mehtani, N. Lee, R. D. Hartschuh, A. Kisliuk, M. D. Foster, A. P. Sokolov, and J. F. Maguire, J. Raman Spectrosc. **36**, 1068 (2005).
[143]Q. Nguyen, R. Ossikovski, and J. Schreiber, Opt. Commun. **274**, 231 (2007).
[144]N. Lee, R. D. Hartschuh, D. Mehtani, A. Kisliuk, J. F. Maguire, M. Green, M. D. Foster, and A. P. Sokolov, J. Raman Spectrosc. **38**, 789 (2007).
[145]N. Hayazawa, A. Tarun, Y. Inouye, and S. Kawata, J. Appl. Phys. **92**, 6983 (2002).
[146]M. Schnell, A. Garcia-Etxarri, A. J. Huber, K. B. Crozier, A. Borisov, J. Aizpurua, and R. Hillenbrand, J. Phys. Chem. C **114**, 7341 (2010).
[147]Z. D. Schultz, S. J. Stranick, and I. W. Levin, Appl. Spectrosc. **62**, 1173 (2008).
[148]A. Downes, D. Salter, and A. Elfick, J. Phys. Chem. B **110**, 6692 (2006).
[149]L. T. Nieman, G. M. Krampert, and R. E. Martinez, Rev. Sci. Instrum. **72**, 1691 (2001).
[150]J. Stadler, T. Schmid, and R. Zenobi, Nano Lett. **10**, 4514 (2010).
[151]R. C. Dunn, Chem. Rev. **99**, 2891 (1999).
[152]D. W. Pohl, W. Denk, and M. Lanz, Appl. Phys. Lett. **44**, 651 (1984).
[153]A. Lewis, M. Isaacson, A. Harootunian, and A. Muray, Ultramicroscopy **13**, 227 (1984).
[154]T. Huser, L. Novotny, T. Lacoste, R. Eckert, and H. Heinzelmann, J. Opt. Soc. Am. A **16**, 141 (1999).
[155]E. Betzig and J. K. Trautman, Science **257**, 189 (1992).
[156]B. Hecht, H. Bielefeldt, Y. Inouye, D. W. Pohl, and L. Novotny, J. Appl. Phys. **81**, 2492 (1997).
[157]A. Mai, L. Zhu, M. Hecker, J. Rinderknecht, C. Georgi, Y. Ritz, and E. Zschech, J. Raman Spectrosc. **39**, 435 (2008).
[158]Y. Jiang, A. Wang, B. Ren, and Z.-Q. Tian, Langmuir **24**, 12054 (2008).
[159]L. A. Gheber, J. Hwang, and M. Edidin, Appl. Opt. **37**, 3574 (1998).
[160]B.-S. Yeo, S. Mädler, T. Schmid, W. Zhang, and R. Zenobi, J. Phys. Chem. C **112**, 4867 (2008).
[161]J. Prikulis, K. V. G. K. Murty, H. Olin, and M. Käll, J. Microsc. **210**, 269 (2003).
[162]E. Betzig, P. L. Finn, and J. S. Weiner, Appl. Phys. Lett. **60**, 2484 (1992).
[163]H. A. Bethe, Phys. Rev. **66**, 163 (1944).
[164]L. Novotny and C. Hafner, Phys. Rev. E **50**, 4094 (1994).
[165]F. Zenhausern, M. P. O'Boyle, and H. K. Wickramasinghe, Appl. Phys. Lett. **65**, 1623 (1994).
[166]F. Zenhausern, Y. Martin, and H. K. Wickramasinghe, Science **269**, 1083 (1995).
[167]B. Hecht, B. Sick, U. P. Wild, V. Deckert, R. Zenobi, O. J. F. Martin, and D. W. Pohl, J. Chem. Phys. **112**, 7761 (2000).
[168]J. Kim and K.-B. Song, Micron **38**, 409 (2007).
[169]A. Lewis, H. Taha, A. Strinkovski, A. Manevitch, A. Khatchatouriants, R. Dekhter, and E. Ammann, Nat. Biotechnol. **21**, 1378 (2003).
[170]A. Rasmussen and V. Deckert, Anal. Bioanal. Chem. **381**, 165 (2005).
[171]N. Hayazawa, Y. Inouye, Z. Sekkat, and S. Kawata, J. Chem. Phys. **117**, 1296 (2002).
[172]E. Bailo and V. Deckert, Chem. Soc. Rev. **37**, 921 (2008).
[173]K. L. A. Chan and S. G. Kazarian, Nanotechnology **22**, 175701 (2011).

[174]N. Hayazawa, Y. Inouye, Z. Sekkat, and S. Kawata, Opt. Commun. **183**, 333 (2000).
[175]M. S. Anderson, Appl. Phys. Lett. **76**, 3130 (2000).
[176]D. S. Bulgarevich and M. Futamata, Appl. Spectrosc. **58**, 757 (2004).
[177]B. Pettinger, G. Picardi, R. Schuster, and G. Ertl, Single Mol. **3**, 285 (2002).
[178]C. Vannier, B.-S. Yeo, J. Melanson, and R. Zenobi, Rev. Sci. Instrum. **77**, 023104 (2006).
[179]T.-A. Yano, T. Ichimura, A. Taguchi, N. Hayazawa, P. Verma, Y. Inouye, and S. Kawata, Appl. Phys. Lett. **91**, 121101 (2007).
[180]L. Novotny, R. X. Bian, and X. S. Xie, Phys. Rev. Lett. **79**, 645 (1997).
[181]E. J. Sánchez, L. Novotny, and X. S. Xie, Phys. Rev. Lett. **82**, 4014 (1999).
[182]D. Richards, R. G. Milner, F. Huang, and F. Festy, J. Raman Spectrosc. **34**, 663 (2003).
[183]B.-S. Yeo, T. Schmid, W. Zhang, and R. Zenobi, Anal. Bioanal. Chem. **387**, 2655 (2007).
[184]B. Pettinger, K. F. Domke, D. Zhang, R. Schuster, and G. Ertl, Phys. Rev. B **76**, 113409 (2007).
[185]E. Bailo and V. Deckert, Angew. Chem. Int. Ed. **47**, 1658 (2008).
[186]W. X. Sun and Z. X. Shen, J. Raman Spectrosc. **34**, 668 (2003).
[187]D. Roy, J. Wang, and C. Williams, J. Appl. Phys. **105**, 013530 (2009).
[188]M. Micic, N. Klymyshyn, Y. D. Suh, and H. P. Lu, J. Phys. Chem. B **107**, 1574 (2003).
[189]Y. C. Martin, H. F. Hamann, and H. K. Wickramasinghe, J. Appl. Phys. **89**, 5774 (2001).
[190]J. T. Krug II, E. J. Sánchez, and X. S. Xie, J. Chem. Phys. **116**, 10895 (2002).
[191]A. L. Demming, F. Festy, and D. Richards, J. Chem. Phys. **122**, 184716 (2005).
[192]A. V. Goncharenko, M. M. Dvoynenko, H.-C. Chang, and J.-K. Wang, Appl. Phys. Lett. **88**, 104101 (2006).
[193]Z. Yang, J. Aizpurua, and H. Xu, J. Raman Spectrosc. **40**, 1343 (2009).
[194]M. Sukharev and T. Seideman, J. Phys. Chem. A **113**, 7508 (2009).
[195]J. A. Porto, P. Johansson, S. P. Apell, and T. López-Ríos, Phys. Rev. B **67**, 085409 (2003).
[196]P. I. Geshev, S. Klein, T. Witting, K. Dickmann, and M. Hietschold, Phys. Rev. B **70**, 075402 (2004).
[197]P. I. Geshev, U. Fischer, and H. Fuchs, Phys. Rev. B **81**, 125441 (2010).
[198]L. Novotny, D. W. Pohl, and B. Hecht, Ultramicroscopy **61**, 1 (1995).
[199]N. Behr and M. B. Raschke, J. Phys. Chem. C **112**, 3766 (2008).
[200]T. Grosges, A. Vial, and D. Barchiesi, Opt. Express **13**, 8483 (2005).
[201]M. B. Raschke and C. Lienau, Appl. Phys. Lett. **83**, 5089 (2003).
[202]A. Taguchi, N. Hayazawa, K. Furusawa, H. Ishitobia, and S. Kawata, J. Raman Spectrosc. **40**, 1324 (2009).
[203]Z. Ma, J. M. Gerton, L. A. Wade, and S. R. Quake, Phys. Rev. Lett. **97**, 260801 (2006).
[204]F. Festy, A. Demming, and D. Richards, Ultramicroscopy **100**, 437 (2004).
[205]W. Zhang, X. Cui, B.-S. Yeo, T. Schmid, C. Hafner, and R. Zenobi, Nano Lett. **7**, 1401 (2007).
[206]N. Anderson, A. Hartschuh, S. Cronin, and L. Novotny, J. Am. Chem. Soc. **127**, 2533 (2005).
[207]J. Steidtner and B. Pettinger, Phys. Rev. Lett. **100**, 236101 (2008).
[208]T.-A. Yano, P. Verma, Y. Saito, T. Ichimura, and S. Kawata, Nat. Photonics **3**, 473 (2009).
[209]F. De Angelis, G. Das, P. Candeloro, M. Patrini, M. Galli, A. Bek, M. Lazzarino, I. Maksymov, C. Liberale, L. C. Andreani, and E. Di Fabrizio, Nat. Nanotechnol. **5**, 67 (2010).
[210]C. C. Neacsu, J. Dreyer, N. Behr, and M. B. Raschke, Phys. Rev. B **75**, 236402 (2007).
[211]K. F. Domke, D. Zhang, and B. Pettinger, J. Phys. Chem. C **111**, 8611 (2007).
[212]T. Ichimura, H. Watanabe, Y. Morita, P. Verma, S. Kawata, and Y. Inouye, J. Phys. Chem. C **111**, 9460 (2007).
[213]N. Anderson, P. Anger, A. Hartschuh, and L. Novotny, Nano Lett. **6**, 744 (2006).
[214]L. Zhu, C. Georgi, M. Hecker, J. Rinderknecht, A. Mai, Y. Ritz, and E. Zschech, J. Appl. Phys. **101**, 104305 (2007).
[215]B. Ren, G. Picardi, B. Pettinger, R. Schuster, and G. Ertl, Angew. Chem. Int. Ed. **44**, 139 (2005).
[216]T. Schmid, B.-S. Yeo, G. Leong, J. Stadler, and R. Zenobi, J. Raman Spectrosc. **40**, 1392 (2009).
[217]S. Berweger, C. C. Neacsu, Y. Mao, H. Zhou, S. S. Wong, and M. B. Raschke, Nat. Nanotechnol. **4**, 496 (2009).
[218]A. Weigel and N. P. Ernsting, J. Phys. Chem. B **114**, 7879 (2010).
[219]P. G. Gucciardi, M. Lopes, R. Déturche, C. Julien, D. Barchiesi, and M. Lamy de la Chapelle, Nanotechnology **19**, 215702 (2008).
[220]L. Novotny, M. R. Beversluis, K. S. Youngworth, and T. G. Brown, Phys. Rev. Lett. **86**, 5251 (2001).
[221]S. Quabis, R. Dorn, and G. Leuchs, Appl. Phys. B **81**, 597 (2005).
[222]N. Hayazawa, Y. Saito, and S. Kawata, Appl. Phys. Lett. **85**, 6239 (2004).
[223]V. Poborchii, T. Tada, and T. Kanayama, Jpn. J. Appl. Phys. **44**, L202 (2005).
[224]R. Ossikovski, Q. Nguyen, and G. Picardi, Phys. Rev. B **75**, 045412 (2007).
[225]M. Motohashi, N. Hayazawa, A. Tarun, and S. Kawata, J. Appl. Phys.**103**, 034309 (2008).
[226]K. J. Yi, X. N. He, Y. S. Zhou, W. Xiong, and Y. F. Lu, Rev. Sci. Instrum. **79**, 073706 (2008).
[227]B. Ren, G. Picardi, and B. Pettinger, Rev. Sci. Instrum. **75**, 837 (2004).
[228]X. Wang, Z. Liu, M.-D. Zhuang, H.-M. Zhang, X. Wang, Z.-X. Xie, D.-Y. Wu, B. Ren, and Z.-Q. Tian, Appl. Phys. Lett. **91**, 101105 (2007).
[229]K. Dickmann, F. Demming, and J. Jersch, Rev. Sci. Instrum. **67**, 845 (1996).
[230]A. Rasmussen and V. Deckert, J. Raman Spectrosc. **37**, 311 (2006).
[231]P. J. Schuck, D. P. Fromm, A. Sundaramurthy, G. S. Kino, and W. E. Moerner, Phys. Rev. Lett. **94**, 017402 (2005).
[232]J. J. Wang, Y. Saito, D. N. Batchelder, J. Kirkham, C. Robinson, and D. A. Smith, Appl. Phys. Lett. **86**, 263111 (2005).
[233]R. F. Aroca, R. A. Alvarez-Puebla, N. Pieczonka, S. Sanchez-Cortez, and J. V. Garcia-Ramos, Adv. Colloid Interface Sci. **116**, 45 (2005).
[234]I. Barsegova, A. Lewis, A. Khatchatouriants, A. Manevitch, A. Ignatov, N. Axelrod, and C. Sukenik, Appl. Phys. Lett. **81**, 3461 (2002).
[235]Y. Gan, Rev. Sci. Instrum. **78**, 081101 (2007).
[236]R. Stöckle, C. Fokas, V. Deckert, R. Zenobi, B. Sick, B. Hecht, and U. P. Wild, Appl. Phys. Lett. **75**, 160 (1999).
[237]P. B. Johnson and R. W. Christy, Phys. Rev. B **6**, 4370 (1972).
[238]C. A. Barrios, A. V. Malkovskiy, A. M. Kisliuk, A. P. Sokolov, and M. D. Foster, J. Phys. Chem. C **113**, 8158 (2009).
[239]B.-S. Yeo, W. Zhang, C. Vannier, and R. Zenobi, Appl. Spectrosc. **60**, 1142 (2006).
[240]S. Berweger, J. M. Atkin, R. L. Olmon, and M. B. Raschke, J. Phys. Chem. Lett. **1**, 3427 (2010).
[241]E. C. Le Ru, M. Meyer, and P. G. Etchegoin, J. Phys. Chem. B **110**, 1944 (2006).
[242]J. E. Bohn, E. C. Le Ru, and P. G. Etchegoin, J. Phys. Chem. C **114**, 7330 (2010).
[243]J. C. Tsang, J. E. Demuth, P. N. Sanda, and J. R. Kirtley, Chem. Phys. Lett. **76**, 54 (1980).
[244]N. P. W. Pieczonka and R. F. Aroca, Chem. Phys. Chem. **6**, 2473 (2005).
[245]W. Zhang, T. Schmid, B.-S. Yeo, and R. Zenobi, J. Phys. Chem. C **112**, 2104 (2008).
[246]A. Downes, D. Salter, and A. Elfick, Opt. Express **14**, 5216 (2006).
[247]G. Baffou, R. Quidant, and F. J. García de Abajo, ACS Nano **4**, 709 (2010).
[248]T. L. Haslett, L. Tay, and M. Moskovits, J. Chem. Phys. **113**, 1641 (2000).
[249]K. Kneipp, Y. Wang, H. Kneipp, I. Itzkan, R. R. Dasari, and M. S. Feld, Phys. Rev. Lett. **76**, 2444 (1996).
[250]E. C. Le Ru and P. G. Etchegoin, Faraday Discuss. **132**, 63 (2006).
[251]R. C. Maher, L. F. Cohen, E. C. Le Ru, and P. G. Etchegoin, Faraday Discuss. **132**, 77 (2006).
[252]P. Verma, Y. Inouye, and S. Kawata, Topics Appl. Phys. **103**, 241 (2006).
[253]A. P. D. Elfick, A. R. Downes, and R. Mouras, Anal. Bioanal. Chem. **396**, 45 (2010).
[254]J. M. Yarbrough, M. E Himmel, and S.-Y. Ding, Biotechnol Biofuels. **2**, 17 (2009).
[255]H. G. Frey, S. Witt, K. Felderer, and R. Guckenberger, Phys. Rev. Lett. **93**, 200801 (2004).
[256]J. Madl, S. Rhode, H. Stangl, H. Stockinger, P. Hinterdorfer, G. J. Schütz, and G. Kada, Ultramicroscopy **106**, 645 (2006).
[257]T. Schmid, J. Burkhard, B.-S. Yeo, W. Zhang, and R. Zenobi, Anal. Bioanal. Chem. **391**, 1899 (2008).
[258]Z. Deng, T. Zink, H.-Y. Chen, D. Walters, F.-T. Liu, and G.-Y. Liu, Biophys. J. **96**, 1629 (2009).
[259]A. Kramer, W. Trabesinger, B. Hecht, and U. P. Wild, Appl. Phys. Lett. **80**, 1652 (2002).
[260]P. Anger, P. Bharadwaj, and L. Novotny, Phys. Rev. Lett. **96**, 113002 (2006).
[261]S. Kühn, U. Håkanson, L. Rogobete, and V. Sandoghdar, Phys. Rev. Lett. **97**, 017402 (2006).

[262]F. M. Huang, F. Festy, and D. Richards, Appl. Phys. Lett. **87**, 183101 (2005).
[263]A. Trache and G. A. Meininger, J. Biomed. Opt. **10**, 064023 (2005).
[264]R. L. Stiles, K. A. Willets, L. J. Sherry, J. M. Roden, and R. P. Van Duyne, J. Phys. Chem. C **112**, 11696 (2008).
[265]H. Gumpp, S. W. Stahl, M. Strackharn, E. M. Puchner, and H. E. Gaub, Rev. Sci. Instrum. **80**, 063704 (2009).
[266]M. Y. Berezin and S. Achilefu, Chem. Rev. **110**, 2641 (2010).
[267]D. Hu, M. Micic, N. Klymyshyn, Y. D. Suh, and H. P. Lu, Rev. Sci. Instrum. **74**, 3347 (2003).
[268]E. Yoskovitz, G. Menagen, A. Sitt, E. Lachman, and U. Banin, Nano Lett. **10**, 3068 (2010).
[269]N. Hayazawa, K. Furusawa, A. Taguchi, S. Kawata, and H. Abe, Appl. Phys. Lett. **94**, 193112 (2009).
[270]N. Hayazawa, K. Furusawa, A. Taguchi, and S. Kawata, J. Appl. Phys.**106**, 113103 (2009).
[271]S. K. Sekatskii and V. S. Letokhov, Appl. Phys. B **63**, 525 (1996).
[272]S. A. Vickery and R. C. Dunn, J. Microsc. **202**, 408 (2001).
[273]B. Knoll and F. Keilmann, Nature (London) **399**, 134 (1999).
[274]A. Cvitkovic, N. Ocelic, J. Aizpurua, R. Guckenberger, and R. Hillenbrand, Phys. Rev. Lett. **97**, 060801 (2006).
[275]A. Hammiche, H. M. Pollock, M. Reading, M. Claybourn, P. H. Turner, and K. Jewkes, Appl. Spectrosc. **53**, 810 (1999).
[276]M. S. Anderson, Appl. Spectrosc. **54**, 349 (2000).
[277]A. Dazzi, R. Prazeres, F. Glotin, and J. M. Ortega, Ultramicroscopy **107**, 1194 (2007).
[278]A. C. Jones, S. Berweger, J. Wei, D. Cobden, and M. B. Raschke, Nano Lett. **10**, 1574 (2010).
[279]N. Ocelic, A. Huber, and R. Hillenbrand, Appl. Phys. Lett. **89**, 101124 (2006).
[280]M. Brucherseifer, C. Kranz, and B. Mizaikoff, Anal. Chem. **79**, 8803 (2007).
[281]G. Scott, S. Ashtekar, J. Lyding, and M. Gruebele, Nano Lett. **10**, 4897 (2010).
[282]I. Rajapaksa, K. Uenal, and H. K. Wickramasinghe, Appl. Phys. Lett. **97**, 073121 (2010).
[283]A. V. Zayats and V. Sandoghdar, J. Microsc. **202**, 94 (2001).
[284]I. I. Smolyaninov, A. V. Zayats, and C. C. Davis, Phys. Rev. B **56**, 9290 (1997).
[285]I. I. Smolyaninov, H. Y. Liang, C. H. Lee, and C. C. Davis, J. Appl. Phys.**89**, 206 (2001).
[286]S. Takahashi and A. V. Zayats, Appl. Phys. Lett. **80**, 3479 (2002).
[287]A. Bouhelier, M. Beversluis, A. Hartschuh, and L. Novotny, Phys. Rev. Lett. **90**, 013903 (2003).
[288]A. V. Zayats, T. Kalkbrenner, V. Sandoghdar, and J. Mlynek, Phys. Rev. B **61**, 4545 (2000).
[289]K. A. Meyer, K. C. Ng, Z. Gu, Z. Pan, W. B. Whitten, and R. W. Shaw, Appl. Spectrosc. **64**, 1 (2010).
[290]A. V. Zayats and I. I. Smolyaninov, Phil. Trans. R. Soc. Lond. A **362**, 843 (2004).
[291]A. Hartschuh, H. Qian, C. Georgi, M. Böhmler, and L. Novotny, Anal. Bioanal. Chem. **394**, 1787 (2009).
[292]N. Anderson, A. Hartschuh, and L. Novotny, Nano Lett. **7**, 577 (2007).
[293]Y. Saito, P. Verma, K. Masui, Y. Inouye, and S. Kawata, J. Raman Spectrosc. **40**, 1434 (2009).
[294]N. Marquestaut, D. Talaga, L. Servant, P. Yang, P. Pauzauskie, and F. Lagugné-Labarthet, J. Raman Spectrosc. **40**, 1441 (2009).
[295]D. Pan, N. Klymyshyn, D. Hu, and H. P. Lu, Appl. Phys. Lett. **88**, 093121 (2006).
[296]K. F. Domke and B. Pettinger, Chem. Phys. Chem. **10**, 1794 (2009).
[297]T. Deckert-Gaudig, E. Rauls, and V. Deckert, J. Phys. Chem. C **114**, 7412 (2010).
[298]K. F. Domke, D. Zhang, and B. Pettinger, J. Am. Chem. Soc. **129**, 6708 (2007).
[299]M. Lucas, W. J. Mai, R. S. Yang, Z. L. Wang, and E. Riedo, Philos. Mag. **87**, 2135 (2007).
[300]D. Passeri, A. Bettucci, A. Biagioni, M. Rossi, A. Alippi, M. Lucci, I. Davoli, and S. Berezina, Rev. Sci. Instrum. **79**, 066105 (2008).
[301]M. Lucas, K. Gall, and E. Riedo, J. Appl. Phys. **104**, 113515 (2008).
[302]B. Bhushan and X. Ling, Phys. Rev. B **78**, 045429 (2008).
[303]M. Lucas, A. M. Leach, M. T. McDowell, S. E. Hunyadi, K. Gall, C. J. Murphy, and E. Riedo, Phys. Rev. B **77**, 245420 (2008).
[304]O. Sahin, S. Magonov, C. Su, C. F. Quate, and O. Solgaard, Nat. Nanotechnol. **2**, 507 (2007).
[305]Z. Deng, V. Lulevich, F.-T. Liu, and G.-Y. Liu, J. Phys. Chem. B **114**, 5971 (2010).
[306]V. Lulevich, T. Zink, H.-Y. Chen, F.-T. Liu, and G.-Y. Liu, Langmuir **22**, 8151 (2006).
[307]A. Trache, J. P. Trzeciakowski, L. Gardiner, Z. Sun, M. Muthuchamy, M. Guo, S. Y. Yuan, and G. A. Meininger, Biophys. J. **89**, 2888 (2005).
[308]A. R. Bizzarri and S. Cannistraro, J. Phys. Chem. B **113**, 16449 (2009).
[309]X. Xu, J. Melcher, and A. Raman, Phys. Rev. B **81**, 035407 (2010).
[310]R. García, R. Magerle, and R. Perez, Nat. Mater. **6**, 405 (2007).
[311]H. Hölscher, Appl. Phys. Lett. **89**, 123109 (2006).
[312]N. McLoughlin, S. L. Lee, and G. Hähner, Appl. Phys. Lett. **89**, 184106 (2006).
[313]R. Böhme, M. Richter, D. Cialla, P. Rösch, V. Deckert, and J. Popp, J. Raman Spectrosc. **40**, 1452 (2009).
[314]U. P. Agarwal, Planta **224**, 1141 (2006).
[315]S. Scolaro, S. Sobanska, J. Barbillat, J. Laureyns, F. Louis, D. Petitprez, and C. Brémard, J. Raman Spectrosc. **40**, 157 (2009).
[316]B.-S. Yeo, E. Amstad, T. Schmid, J. Stadler, and R. Zenobi, Small **5**, 952 (2009).
[317]E. Dague, D. Alsteens, J.-P. Latgé, C. Verbelen, D. Raze, A. R. Baulard, and Y. F. Dufrêne, Nano Lett. **7**, 3026 (2007).
[318]F. Kienberger, A. Ebner, H. J. Gruber, and P. Hinterdorfer, Acc. Chem. Res. **39**, 29 (2006).
[319]T. Taubner, R. Hillenbrand, and F. Keilmann, Appl. Phys. Lett. **85**, 5064 (2004).
[320]M. Brehm, T. Taubner, R. Hillenbrand, and F. Keilmann, Nano Lett. **6**, 1307 (2006).
[321]D. J. Müller and Y. F. Dufrêne, Nat. Nanotechnol. **3**, 261 (2008).
[322]U. Neugebauer, U. Schmid, K. Baumann, W. Ziebuhr, S. Kozitskaya, V. Deckert, M. Schmitt, and J. Popp, Chem. Phys. Chem. **8**, 124 (2007).
[323]D. Cialla, T. Deckert-Gaudig, C. Budich, M. Laue, R. Möller, D. Naumann, V. Deckert, and J. Poppa, J. Raman Spectrosc. **40**, 240 (2009).
[324]X. Chen, A. Kis, A. Zettl, and C. R. Bertozzi, Proc. Natl. Acad. Sci. U. S. A. **104**, 8218 (2007).
[325]A. Meister, M. Gabi, P. Behr, P. Studer, J. Vörös, P. Niedermann, J. Bitterli, J. Polesel-Maris, M. Liley, H. Heinzelmann, and T. Zambelli, Nano Lett. **9**, 2501 (2009).
[326]G. Compagnini, F. Giannazzo, S. Sonde, V. Raineri, and E. Rimini, Carbon **47**, 3201 (2009).
[327]M. R. Joya, P. S. Pizani, R. G. Jasinevicius, R. E. Samad, W. de Rossi, and N. D. Vieira, Jr., J. Appl. Phys. **100**, 053518 (2006).
[328]H. Zhong, J. Wang, X. Chen, Z. Li, W. Xu, and W. Lu, J. Appl. Phys. **99**, 103905 (2006).
[329]S. W. Lee, G.-H. Jeong, and E. E. B. Campbell, Nano Lett. **7**, 2590 (2007).
[330]C. Georgi, M. Hecker, and E. Zschech, J. Appl. Phys. **101**, 123104 (2007).
[331]R. Ossikovski, Q. Nguyen, G. Picardi, and J. Schreiber, J. Appl. Phys. **103**, 093525 (2008).
[332]Z. Wei, D. B. Wang, S. Kim, S.-Y. Kim, Y. Hu, M. K. Yakes, A. R. Laracuente, Z. Dai, S. R. Marder, C. Berger, W. P. King, W. A. de Heer, P. E. Sheehan, and Elisa Riedo, Science **328**, 1373 (2010).
[333]D. C. Coffey, O. G. Reid, D. B. Rodovsky, G. P. Bartholomew, and D. S. Ginger, Nano Lett. **7**, 738 (2007).
[334]J. M. Stiegler, A. J. Huber, S. L. Diedenhofen, J. Gómez Rivas, R. E. Algra, E. P. A. M. Bakkers, and R. Hillenbrand, Nano Lett. **10**, 1387 (2010).